Review article

On neglecting Coriolis and related couplings in first-principles rovibrational spectroscopy: Considerations of symmetry, accuracy, and simplicity. II. Case studies for H₂O isotopologues, H₃⁺, O₃, and NH₃

János Sarka [a,*], Bill Poirier [a,*], Viktor Szalay [b], Attila G. Császár [c,*]

[a] Department of Chemistry and Biochemistry, Texas Tech University, Lubbock, TX 79409, USA
[b] Institute for Solid State Physics and Optics, Wigner Research Centre for Physics, Hungarian Academy of Sciences, P.O. Box 49, H-1525 Budapest, Hungary
[c] MTA-ELTE Complex Chemical Systems Research Group and Laboratory of Molecular Structure and Dynamics, Institute of Chemistry, ELTE Eötvös Loránd University, H-1117 Budapest, Pázmány Péter sétány 1/A, Hungary

ARTICLE INFO

ABSTRACT

For centuries, it has been known that vibrational and rotational degrees of freedom are in general not separable. Nevertheless, surprisingly little is known about the best strategies for approximately separating these degrees of freedom in practice—even in the case of semirigid molecules, where the separation is most meaningful. There is also some confusion in the literature about the proper way to quantify the magnitude of the Coriolis (*i.e.*, rotation-vibration) coupling in rovibrational Hamiltonians or its effect on the rovibrational eigenenergies. In this study, a vibrational-coordinate-independent metric is proposed to quantify the magnitude of the Coriolis contribution to the rovibrational Hamiltonian. The impact of Coriolis coupling on the rovibrational eigenenergies is computed numerically exactly, using both full and various truncated Hamiltonians. The role played by the choice of the vibrational coordinate system—and especially by the choice of "embedding" or body-fixed frame—is examined extensively, both numerically and analytically. This investigation targets several molecular prototypes, all of which serve as important benchmarks for the high-resolution spectroscopic community. Most of these are triatomic molecules, including water ($H_2^{16}O$), its deuterated isotopologues ($D_2^{16}O$ and $HD^{16}O$), H_3^+, and ozone ($^{16}O_3$), but the tetratomic ammonia molecule ($^{14}NH_3$) is also investigated. These studies provide important insight into the nature of Coriolis coupling under various circumstances. The findings of this study also have significant practical ramifications, vis-à-vis the use of simplifying numerical approximation techniques in nuclear-motion computations.

Contents

* Corresponding author.
  E-mail addresses: Janos.Sarka@ttu.edu (J. Sarka), Bill.Poirier@ttu.edu (B. Poirier), csaszarag@caesar.elte.hu (A.G. Császár).

1. Introduction

Whether classical or quantum mechanical, the dynamics of many-body systems is a notoriously challenging problem whose solution benefits from—and often requires—simplifying assumptions. To this end, the full problem is generally decomposed into translational, rotational, and vibrational components. Yet, whereas overall translation perfectly separates from everything else (provided there are no external fields or spatial constraints), rotational and vibrational motions are inherently coupled. Moreover, the nature and precise form of this rotation-vibration or "Coriolis" coupling (CC) depend on the definition of the rotational degrees of freedom (dofs), which is essentially arbitrary. As a consequence, the accuracy of a given separable approximation (e.g., setting the CC contribution to zero) must depend on the choice of coordinates, which lends additional complexity—but also possibility—to the enterprise.

The above considerations are particularly pertinent for quantum calculations, for which the computational cost increases dramatically (typically exponentially) with the number of dofs, both in memory and CPU time. In particular, computing rovibrational molecular eigenenergies converged to the accuracy of typical high-resolution spectroscopic measurements (*i.e.*, $\sim 10^{-2}$ cm^{-1} or better) requires variational methods [1–17] that are all the more computationally expensive, given the large number of eigenstates that typically need to be determined in practice [18]. Simplifying approximations that can effectively reduce the number of dofs, and thereby also the corresponding basis set size and the number of explicitly computed eigenstates, are thus very important.

An equally important consideration is that such approximations should introduce only a minor, acceptable loss of accuracy. Whereas, in principle, spectroscopic accuracy might be the desired standard of the field, in practice, many potential energy surfaces (PESs) are able to yield eigenenergies that are only accurate to a few cm^{-1} or so. Accordingly, we aim for an accuracy standard of a few cm^{-1}, which should prove perfectly acceptable, if it can be achieved, for a number of applications. On the other hand, it is not the PES contribution but rather the exact rovibrational kinetic energy operator (KEO) [19,20] contribution, where the Coriolis contribution enters the Hamiltonian. Ideally, we would like to contrive a separable KEO approximation that can be successfully applied not only to semirigid molecules, but also to those with vibrational dynamics of arbitrary complexity [21–29]. However, for *quasistructural* molecules [29] this separation clearly cannot be expected to work.

Exact rovibrational Hamiltonians can always be written in the form

$$\hat{H}_{VR} = \hat{T} + \hat{V} = \hat{T}_V + \hat{T}_R + \hat{T}_{VR} + \hat{V}, \tag{1}$$

where $\hat{T}$ and $\hat{V}$ are the KEO and PES operators, respectively. The pure rotational (R) and pure vibrational (V) contributions to the KEO are denoted using appropriate subscripts, whereas the rotation-vibration (VR) coupling or CC contribution is denoted as $\hat{T}_{VR}$. It is advantageous that in external-field-free cases, as assumed in Eq. (1), $\hat{V}$ is independent of the rotational dofs. Consequently, the matrix representation of $\hat{H}_{VR}$ becomes block-diagonal by the rotational quantum number, J, which is thus a good quantum number [30].

Insofar as developing useful separable approximations to Eq. (1) is concerned, this field is nearly as old as quantum mechanics itself [19,20,31–36]. As mentioned, part of the richness stems from the fact that the three-term decomposition of $\hat{T}$ in Eq. (1) depends on the choice of rotational dofs—which in turn is determined by the choice of "embedding" or body-fixed frame. For triatomic molecules, general rovibrational Hamiltonians have been derived by Sutcliffe and Tennyson [37,38], including arbitrary axis embeddings. Rovibrational Hamiltonians satisfying the Casimir condition were also developed [39]. For triatomic molecules, Eckart embeddings [40,41] have been investigated by Wei and Carrington [42] using Radau, valence, and Jacobi vibrational coordinates. Wei and Carrington also derived Eckart-frame Hamiltonians using valence [43] and Radau [44] coordinates, as well as their bond (vector) and bisector equivalents.

In Ref. [43], Wei and Carrington argued that the magnitude of CC can be assessed by examining the individual tensor elements of $\hat{T}_{VR}$. However, this is a dangerous prescription, because the tensor elements also depend on the choice of the vibrational coordinates, and therefore the individual tensor elements are somewhat arbitrary. In reality, the $\hat{T}_{VR}$ operator is determined *solely* by the embedding, and is therefore (vibration) coordinate-independent. Based on this kind of analysis, Wei and Carrington deduced that it is the Eckart embedding that results in minimal CC [44]—and this simple presumption has evidently never been questioned since, even though it was based on a coordinate-dependent measure. Wei and Carrington also acknowledged [43] that their effort is just the "first step" towards establishing the relative advantages of the different embeddings; to really provide a definitive assessment, it would be necessary to calculate rovibrational eigenenergies using different embeddings. These are precisely the sort of calculations that we have performed here, for a number of molecular systems, after a hiatus of two decades.

The above discussion presumes that the simplest way to arrive at a "separable" approximate KEO is to simply neglect the Coriolis contribution, $\hat{T}_{VR}$. In practice, however, this does *not* actually result in a truly separable calculation, for which vibrational and rotational contributions can be computed independently—and therefore, much more inexpensively. The reason is that $\hat{T}_R$ depends parametrically on the vibrational coordinates. Consequently, in order to achieve true separability, it is also necessary to modify or discard parts of $\hat{T}_R$. To this end, we introduce a sequence of

increasingly severe approximations—starting with the above *Coriolis-free* approximation (CFA), then moving on to the *diagonal* $\mathbf{G}_R$ approximation (DGRA), and finally, the *generalized centrifugal sudden* approximation (GCSA) [45].

The centrifugal sudden (CS) (and related) approximation has itself enjoyed a long history, and so this portion of the present work is important for establishing the requisite theoretical connections between CFA and CS. A few decades ago, the "j_z conserving" CS approximation was developed by McGuire and Kouri [46] in Jacobi coordinates for triatomic (atom + diatom) quantum scattering calculations [46]. At the same time, Pack [47] investigated space-fixed and body-fixed axes in atom-diatom molecule scattering problems when the rotation is treated in a "sudden approximation". In chemical physics, these approaches have been applied primarily in the context of reactive scattering [48–52], although some authors have employed them in the rovibrational spectroscopy context, as well [53,54].

In response to the state of affairs outlined above, our present investigation is structured as follows. First, a comprehensive study is performed for the $H_2{}^{16}O$ AB_2-type triatomic molecule. In particular, accurately converged rovibrational energy levels are computed using each of the three approximations, *i.e.*, CFA, DGRA, and GCSA, employing a variety of different embeddings and vibrational coordinates. These are then compared with similarly-well-converged results using the exact KEO. Additionally, we examine the $\hat{T}_{VR}$ tensor elements analytically, evaluated at a range of different molecular geometries. Some interesting trends are observed, which we justify using theoretical arguments. In order to confirm the generality of the conclusions obtained, similar investigations are conducted for a set of molecules, venturing successively further from $H_2{}^{16}O$. These studies start with the deuterated isotopologues of $H_2{}^{16}O$ (*i.e.*, $D_2{}^{16}O$ and $HD{}^{16}O$), and then move on to H_3^+, ozone ($^{16}O_3$), and the fluxional tetratomic ammonia molecule ($^{14}NH_3$). For these studies, only CFA and exact KEO calculations were performed, although multiple embeddings were considered, and both tensor elements and rovibrational eigenenergies were computed. Finally, we have performed some calculations to confirm numerically what we predict theoretically—i.e., that exact KEO results should be independent of both vibrational coordinate system *and* embedding, whereas CFA results should be embedding-dependent but vibrational-coordinate-independent. Certain embeddings therefore behave better than others in the CFA, and

Table 1
Summary of the different embeddings studied in this paper. The abbreviations listed here are used throughout the paper. The *s/a* prefix indicates symmetric/asymmetric Jacobi coordinates.

abbreviation	full name	internal coordinates	molecules the embedding is applied to
EE	Eckart	any	$H_2{}^{16}O$, $D_2{}^{16}O$, $HD{}^{16}O$, H_3^+, $^{16}O_3$, $^{14}NH_3$
FEE	flexible-Eckart	any	$H_2{}^{16}O$, $HD{}^{16}O$, H_3^+, $^{14}NH_3$
VBE	valence bisector	valence	$H_2{}^{16}O$, $D_2{}^{16}O$, $HD{}^{16}O$, H_3^+, $^{16}O_3$
Vr$_1$E	valence r_1[a]	valence	$H_2{}^{16}O$, $D_2{}^{16}O$, $HD{}^{16}O$, H_3^+, $^{16}O_3$
VFEE	valence flexible-Eckart	valence	$H_2{}^{16}O$, $HD{}^{16}O$
VwBE	valence weighted-bisector	valence	$HD{}^{16}O$
RBE	Radau bisector	Radau	$H_2{}^{16}O$, $D_2{}^{16}O$, $HD{}^{16}O$, H_3^+, $^{16}O_3$
Rr$_1$E	Radau r_1[a]	Radau	$H_2{}^{16}O$, $D_2{}^{16}O$, $HD{}^{16}O$, H_3^+, $^{16}O_3$
RFEE	Radau flexible-Eckart	Radau	$H_2{}^{16}O$, $HD{}^{16}O$
RwBE	Radau weighted-bisector	Radau	$HD{}^{16}O$
*s/a*JrE	*s/a*-Jacobi r[b]	*s/a*-Jacobi	$H_2{}^{16}O$, $D_2{}^{16}O$, H_3^+, $^{16}O_3$
*s/a*JRE	*s/a*-Jacobi R[b]	*s/a*-Jacobi	$H_2{}^{16}O$, $D_2{}^{16}O$, H_3^+, $^{16}O_3$
*s/a*JBE	*s/a*-Jacobi bisector[b]	*s/a*-Jacobi	$H_2{}^{16}O$, $D_2{}^{16}O$, H_3^+, $^{16}O_3$
zxzE	"*zxz*" (scattering)	valence	$^{14}NH_3$

[a] For $HD{}^{16}O$, the valence/Radau r_1 embedding (Vr$_1$E/Rr$_1$E) becomes valence/Radau r_H (Vr$_H$E/Rr$_H$E) and r_D (Vr$_D$E/Rr$_D$E) embedding.
[b] For A_3 molecules, the *s/a* prefix is dropped from the name and the abbreviation of the embedding.

it is our task here to determine which those are, using—for the first time, to our knowledge—a combined analytical and numerical approach.

Some of our results concerning the separation of vibrations and rotations have been detailed in a recent paper [45], where we studied only $H_2{}^{16}O$, and considered just a few selected embeddings. The present paper builds on and extends our previous work in several important ways. First and foremost, we extend our earlier study to a much broader set of molecules, including ABC and A_3 triatomics, as well as the fluxional tetraatomic, NH_3. Second, we consider a much broader range of embeddings (see Table 1), including the sophisticated class known as flexible or "Sayvetz" embeddings [55], tailored to an entire isomerization pathway, rather than to just a single reference geometry. Such embeddings are particularly important for floppy molecules with low isomerization barriers, such as NH_3. Third, we make use of a *coordinate-independent measure* to assess the magnitude of CC. As discussed, earlier studies [43,44] used an *ad hoc* criterion for this, that depends on the specific choice of vibrational coordinates, thereby leading to "apples-to-oranges" comparisons, and possibly unreliable conclusions. Finally, we also provide more detailed and rigorous theoretical explanations for many of the observed trends, thereby placing our conclusions on a more general, reliable footing.

2. Triatomic AB_2 molecules

2.1. Overview

Let us take a triatomic AB_2 molecule with a reference geometry of C_{2v} point-group symmetry. This reference structure can be the global minimum, as in the case of the ground electronic state of $H_2{}^{16}O$ [56]. Alternatively, the reference structure might be the transition state between two equivalent C_s minima, as in the case of the $\tilde{C}\ {}^1B_2$ electronic state of $^{32}SO_2$ [57,58]. For purposes of the present study, the choice of the reference structure need have nothing to do with the nature of the reference point, whether a minimum or a transition state; this choice is used to define a reference orientation, and to specify the body-fixed frame or "embedding".

For the reference geometry, we define the reference orientation such that the $\hat{x}$ axis is parallel to the B_1–B_2 separation vector (where 1 and 2 label the two B atoms), and the $\hat{z}$ axis is perpendicular to the molecular frame (Fig. 1). Let $\vec{r}_1$, $\vec{r}_2$, and $\vec{r}_A$, respectively, denote the positions of the atoms B_1, B_2, and A in the body-fixed frame. For the reference geometry, these position vectors must take the following form:

$$
\begin{aligned}
\vec{r}_1^{\,ref} &= (-x_0, y_0, 0) \\
\vec{r}_2^{\,ref} &= (x_0, y_0, 0) \\
\vec{r}_A^{\,ref} &= \left(0, -\left[\frac{2m}{M}\right]y_0, 0\right).
\end{aligned} \tag{2}
$$

Here, $m = m_B$ and $M = m_A$ denote the masses of the B and A atoms, respectively, and the coordinates have been chosen so that the center of mass (COM) coincides with the origin of the body-fixed frame.

The choice of embedding is determined by specifying the values of the three body-fixed position vectors, $\vec{r}_1$, $\vec{r}_2$, and $\vec{r}_A$, with respect to all possible vibrational displacements from the reference geometry. In all cases, the displacements are constrained by the COM condition, *i.e.*,

$$
m\vec{r}_1 + m\vec{r}_2 + M\vec{r}_A = \vec{0}. \tag{3}
$$

Thus, $\vec{r}_A$ is completely determined by $\vec{r}_1$ and $\vec{r}_2$, so that there are six independent rovibrational coordinates (*e.g.*, the Cartesian com-
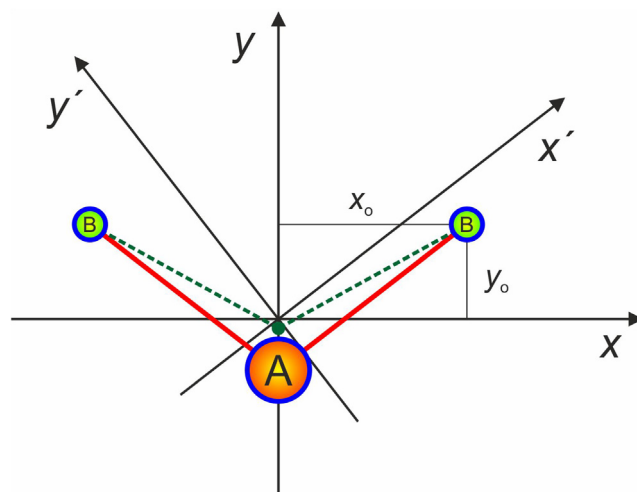
Fig. 1. The body-fixed frame $(\hat{x}, \hat{y})$ used in this study for the three linear embeddings investigated (see text). The valence bond and the Radau vectors are marked with red and dashed green lines, respectively. The Radau special point between the A atom and the center of mass at the origin is indicated with a green dot. The rotated axes $(\hat{x}', \hat{y}')$ used for Jacobi bond embeddings are also illustrated (with a similar rotation also used for the Radau bond embeddings).

ponents of $\vec{r}_1$ and $\vec{r}_2$). However, there are only three independent vibrational displacements, so in effect there is a (local) three-parameter family of possible embedding choices.

For triatomic systems, the three atoms always define a plane (except for collinear geometries), and so it is natural to restrict consideration to only those frames for which the $\hat{z}$ components of the atoms are all zero ($z_1 = z_2 = z_A = 0$). This constraint reduces the number of independent coordinates to just four, (x_1, y_1, x_2, y_2). This reduces the range of local embedding choices to a one-parameter family. All of the triatomic embeddings considered in this work are subject to this constraint.

Consider a particular embedding. In general, it is possible to apply a *global* rotation ($\tilde{R}$) to the $(\hat{x}, \hat{y}, \hat{z})$ body-fixed coordinate system,

$$
\vec{r} \rightarrow \vec{r}' = \tilde{R} \cdot \vec{r}, \tag{4}
$$

without changing anything fundamental about the embedding itself (*i.e.*, the rotational $\hat{T}_R$ and CC $\hat{T}_{VR}$ contributions to the total rovibrational Hamiltonian are essentially unchanged). There are at least two ways to interpret this situation. In the *active* interpretation, Eq. (4) transforms any given geometry from the reference orientation to some arbitrary orientation. Thus, by applying Eq. (4), all orientations can be generated. In the *passive* interpretation, we simply redefine what we take to be the body-fixed axes, from $(\hat{x}, \hat{y}, \hat{z})$ to $(\hat{x}', \hat{y}', \hat{z}')$. The latter interpretation can be useful when considering, *e.g.*, the so-called "asymmetric" embeddings, which do not respect the permutation symmetry of B_1 and B_2. Note, however, that in this context the ($\hat{z}$-axis) rotation angle *does* depend on the geometry; it is therefore not a *global* rotation, and so it does indeed result in a change of embedding. In any event, for all "symmetric" embeddings, the original $(\hat{x}, \hat{y}, \hat{z})$ axes are always the most relevant.

2.2. Vibrational displacements for symmetric embeddings

Consider the vibrational displacements that transform the reference geometry into any other C_{2v} geometry. There is a two-parameter family of such displacements, corresponding to "symmetric stretch" and (symmetric) "bend" vibrational motions. Note that any C_{2v} geometry remains invariant under permutation of B_1 and B_2. Therefore, for any symmetric embedding, the refer-
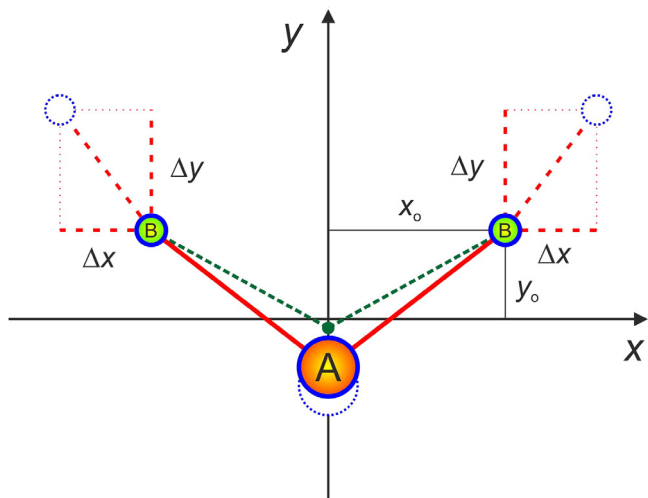
Fig. 2. Symmetric vibrational displacements in linear embeddings using $(\Delta x, \Delta y)$ general coordinates.

Fig. 3. Asymmetric vibrational displacement in linear embeddings using the Δ general coordinate. The B atom displacements are in a direction defined by the angle ϵ, whose value also serves to define the particular linear embedding.

ence orientation for any C_{2v} geometry must retain the same symmetric form as the reference geometry. Consequently, the position vectors must adopt the form

$$\begin{aligned}
\vec{r}_1^{\,C_{2v}} &= (-(x_0 + \Delta x), y_0 + \Delta y, 0) \\
\vec{r}_2^{\,C_{2v}} &= (x_0 + \Delta x, y_0 + \Delta y, 0) \\
\vec{r}_A^{\,C_{2v}} &= \left(0, -\left[\frac{2m}{M}\right](y_0 + \Delta y), 0\right).
\end{aligned} \tag{5}$$

In Eq. (5), Δx and Δy represent the two independent symmetric vibrational displacement parameters (see Fig. 2).

Note that, as per Eq. (5), all symmetric embeddings behave exactly the same with respect to symmetric vibrational displacements. We can thus take Δx and Δy to be the two symmetric vibrational coordinates, describing symmetric stretch and bend motions for all symmetric embeddings—which we shall do for pedagogical and comparative purposes. Note further that for all symmetric embeddings, the two-dimensional (2D) subspace of pure symmetric displacements is *linear* (i.e., flat and Cartesian). In other words, if the configurations

$$\vec{r}_1^{\,\text{ref}} + \Delta\vec{r}_1^{\,C_{2v}}, \vec{r}_2^{\,\text{ref}} + \Delta\vec{r}_2^{\,C_{2v}}, \vec{r}_A^{\,\text{ref}} + \Delta\vec{r}_A^{\,C_{2v}} \tag{6}$$

and $$\vec{r}_1^{\,\text{ref}} + \Delta\vec{r'}_1^{\,C_{2v}}, \vec{r}_2^{\,\text{ref}} + \Delta\vec{r'}_2^{\,C_{2v}}, \vec{r}_A^{\,\text{ref}} + \Delta\vec{r'}_A^{\,C_{2v}} \tag{7}$$

both belong to the subspace of symmetric displacements, then so does

$$\vec{r}_1^{\,\text{ref}} + \Delta\vec{r}_1^{\,C_{2v}} + \Delta\vec{r'}_1^{\,C_{2v}}, \vec{r}_2^{\,\text{ref}} + \Delta\vec{r}_2^{\,C_{2v}} + \Delta\vec{r'}_2^{\,C_{2v}}, \vec{r}_A^{\,\text{ref}} + \Delta\vec{r}_A^{\,C_{2v}} + \Delta\vec{r'}_A^{\,C_{2v}}. \tag{8}$$

Again, this is true for all symmetric embeddings.

Two out of the three vibrational displacements are thus already accounted for. In reality, the various symmetric embeddings differ only with respect to how they treat the *third* type of vibrational displacement, the asymmetric stretch. Three of the symmetric embeddings considered in this paper are very closely related to each other—in the sense that in all three cases the pure asymmetric displacements are linear, in the sense of Eq. (8). In all three cases, asymmetric stretch displacement corresponds to linear displacement by the distance Δ, in a direction for B_1/B_2 that is at an angle ϵ below/above the $\hat{x}$ axis (see Fig. 3). Accordingly, we shall call these three embeddings the "linear embeddings". The only difference between any two linear embeddings is therefore with respect to how the angle ϵ is defined. Although only three such choices are
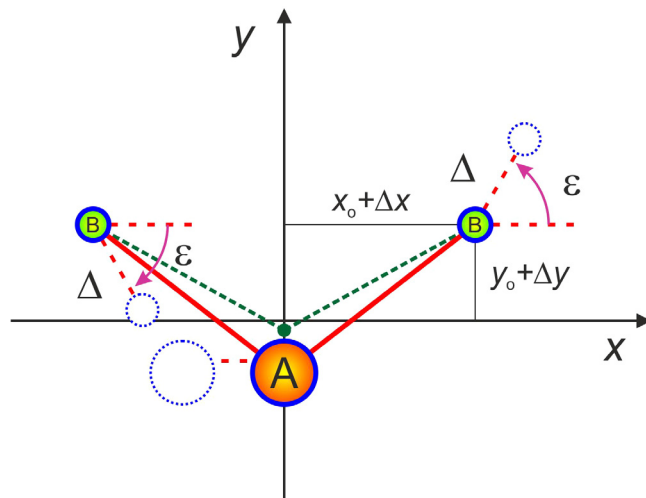
considered here, in principle a vast range of linear embeddings are possible. It may be worth investigating these more fully in the future, for as we shall see, the linear embeddings seem to offer the best performance, in practice, in terms of separating vibration and rotation via minimization of the CC, for all systems studied.

2.3. Asymmetric stretch displacements for the three linear embeddings

2.3.1. Eckart embedding

The simplest and most famous of the three linear embeddings is the Eckart embedding (EE). In addition to the usual center-of-mass condition [Eq. (3)], EE is defined by

$$m(\vec{r}_1^{\,\text{ref}} \times \Delta\vec{r}_1) + m(\vec{r}_2^{\,\text{ref}} \times \Delta\vec{r}_2) + M(\vec{r}_A^{\,\text{ref}} \times \Delta\vec{r}_A) = \vec{0}, \tag{9}$$

where the displacements are defined as $\Delta\vec{r}_1 = (\vec{r}_1 - \vec{r}_1^{\,\text{ref}})$, $\Delta\vec{r}_2 = (\vec{r}_2 - \vec{r}_2^{\,\text{ref}})$, and $\Delta\vec{r}_A = (\vec{r}_A - \vec{r}_A^{\,\text{ref}})$. Equation (9) takes the form of a vector equation. However, since all vectors lie in the $\hat{x}$–$\hat{y}$ plane, the cross-product vectors all point in the $\hat{z}$ direction. Thus, in reality, Eq. (9) represents a single new constraint on $\{\vec{r}_1, \vec{r}_2, \vec{r}_A\}$—exactly what is needed to specify the embedding.

For the subspace of pure symmetric displacements,

$$\begin{aligned}
\Delta\vec{r}_1^{\,C_{2v}} &= (-\Delta x, \Delta y, 0) \\
\Delta\vec{r}_2^{\,C_{2v}} &= (\Delta x, \Delta y, 0) \\
\Delta\vec{r}_A^{\,C_{2v}} &= \left(0, -\left[\frac{2m}{M}\right]\Delta y, 0\right),
\end{aligned} \tag{10}$$

which satisfies Eq. (9). For the pure asymmetric-stretch displacements, Section 2.2 suggests the following ansatz:

$$\begin{aligned}
\Delta\vec{r}_1^{\,C_s} &= (\Delta\cos\epsilon, -\Delta\sin\epsilon, 0) \\
\Delta\vec{r}_2^{\,C_s} &= (\Delta\cos\epsilon, \Delta\sin\epsilon, 0) \\
\Delta\vec{r}_A^{\,C_s} &= \left(-\left[\frac{2m}{M}\right]\Delta\cos\epsilon, 0, 0\right).
\end{aligned} \tag{11}$$

Substituting Eq. (11) into Eq. (9) results in the following determination of the EE angle ϵ:

$$\tan\epsilon^{\text{EE}} = \left(1 + \left[\frac{2m}{M}\right]\right)\left(\frac{y_0}{x_0}\right). \tag{12}$$

The value of the angle ϵ, as specified in Eq. (12), corresponds to the motion of B_1/B_2 directly towards/away from the *reference geometry* position of A. Note that this angle remains constant over all asym-

metric stretch displacements, Δ. This means that both B_1 and B_2 follow straight-line paths, so that the asymmetric displacement subspace is linear. Furthermore, it can be shown that Eq. (12) also generalizes for *arbitrary* vibrational displacements, and it is thus independent of Δx and Δy, as well as Δ. As a consequence, the *entire* vibrational subspace is linear for the Eckart frame—the only "linear embedding" considered here for which this property holds.

2.3.2. Valence bisector embedding

Consider pure asymmetric stretch displacements with respect to the chosen reference geometry. In the Eckart frame, even for sufficiently large Δ, atom B_1 never collides with atom A, because A is itself displaced from its reference position [Eq. (11)]. In contrast, in the *valence bisector embedding* (VBE), the B_1/B_2 atoms always move towards/away from the *actual* position of atom A, along the actual valence bonds. Consequently, the A and B atoms will always "collide" eventually, even if starting from an arbitrary C_{2v} geometry that is not necessarily the reference geometry. Note that by applying asymmetric displacements to different C_{2v} starting geometries, we can generate any particular asymmetric displacement subspace. These can be labeled in the same manner as the C_{2v} starting geometries, i.e., in terms of the symmetric displacements, $(\Delta x, \Delta y)$. In this manner, the whole vibrational displacement space may be explored.

We continue to assume a linear ansatz in terms of the angle ϵ, so that the general vibrational displacements are of the form

$$
\begin{aligned}
\Delta \vec{r}_1 &= \ (-\Delta x + \Delta \cos \epsilon, \Delta y - \Delta \sin \epsilon, 0) \\
\Delta \vec{r}_2 &= \ (\Delta x + \Delta \cos \epsilon, \Delta y + \Delta \sin \epsilon, 0) \\
\Delta \vec{r}_A &= \ \left(-\left[\frac{2m}{M}\right] \Delta \cos \epsilon, -\left[\frac{2m}{M}\right] \Delta y, 0 \right).
\end{aligned}
\tag{13}
$$

The main difference from the Eckart frame is that the direction of motion, ϵ, clearly depends on the particular C_{2v} starting geometry—i.e., on Δx and Δy, though not on Δ. Consequently, although any particular asymmetric displacement subspace is linear in the sense of Section 2.2, the vibrational space as a whole is not. Essentially, it is a flat linear space that has been "twisted".

Formally, the VBE is defined such that the $\hat{y}$ axis corresponds to the bisector of the B_1–A–B_2 bond angle. From this definition, it is clear that all of the above claims are satisfied, except those pertaining to ϵ. However, by applying the valence bisector condition to the ansatz of Eq. (13), the following solution is obtained:

$$
\tan \epsilon^{\text{VBE}} = \left(1 + \left[\frac{2m}{M}\right] \right)^2 \left(\frac{y_0 + \Delta y}{x_0 + \Delta x} \right).
\tag{14}
$$

Eq. (14) does indeed depend on the symmetric displacements $(\Delta x, \Delta y)$ (i.e., on the non-reference C_{2v} starting geometry), but is independent of Δ, as claimed. Note also that even for pure asymmetric stretching, i.e., $\Delta x = \Delta y = 0$, the direction ϵ as specified by Eq. (14) is *not* equivalent to the corresponding Eckart ϵ, in fact it represents a steeper angle than in Eq. (12). Only in the limit $(m/M) \rightarrow 0$ do the two ϵ values become equivalent.

2.3.3. Radau bisector embedding

The (symmetric) Radau coordinates are defined in terms of the two Radau vectors, which extend from a common origin, lying partway between the AB_2 center of mass and atom A, out to the two B atoms (Fig. 1). The *Radau bisector embedding* (RBE) is then defined such that the bisector of the angle formed by the two Radau vectors lies along the body-fixed $\hat{y}$ axis. This is in complete analogy with the VBE, and indeed—based on the description above—the two should become equivalent in the $(m/M) \rightarrow 0$ limit.

By applying the Radau bisector condition to the ansatz of Eq. (13), a linear solution is again obtained:

$$
\tan \epsilon^{\text{RBE}} = \left(1 + \left[\frac{2m}{M}\right] \right) \left(\frac{y_0 + \Delta y}{x_0 + \Delta x} \right).
\tag{15}
$$

As in the VBE case, the RBE vibrational space is only separately "linear", in the pure symmetric and pure asymmetric subspaces. The vibrational space as a whole is thus once again "twisted" (see Section 2.3.2).

In many respects, Eq. (15) lies "halfway" between the EE [Eq. (12)] and VBE [Eq. (14)] forms. In particular, we see that Eq. (15) reduces to Eq. (14) in the $(m/M) \rightarrow 0$ limit, as predicted. This is true regardless of the symmetric displacements, Δx and Δy, because the geometric (i.e., second) factors in the right-hand side of the two equations are identical. On the other hand, in comparing Eq. (15) with Eq. (12), we see that it is the mass (i.e., first) factor that is identical, whereas the Radau geometric factor has been modified from the Eckart form, to incorporate the symmetric displacements.

This situation can be interpreted as follows. Whereas in EE asymmetric displacements are always such that the B atoms move towards/away from the location of A as defined for the *reference* geometry, in the RBE case, this becomes the location of A as defined by the C_{2v} *starting geometry*. The pure asymmetric subspaces for EE and RBE are thus the same, since pure asymmetric stretching corresponds to $\Delta x = \Delta y = 0$. Furthermore, in the vicinity of the reference geometry, the two embeddings are locally equivalent to each other, but different from the VBE. These facts will later be seen to have important repercussions.

2.4. Symmetric Jacobi embeddings

In addition to the three linear embeddings described above, EE, VBE, and RBE, there are two other symmetric embeddings that we also consider. These are both based on the symmetric (s) Jacobi coordinates, for which one vector is defined as the difference between B_1 and B_2 positions, and the second vector is defined as the difference between the B_1–B_2 center of mass and the position of A (see Fig. 4). The first Jacobi vector is called $\vec{r}$, the second Jacobi vector is called $\vec{R}$. Two natural symmetric embeddings are obtained from the symmetric Jacobi vectors described above. The first, which we call the "symmetric Jacobi r" embedding (sJrE) is defined by taking $\vec{r}$ to be parallel with the body-fixed $\hat{x}$ axis. The second, the "symmetric Jacobi R" embedding (sJRE) has $\vec{R}$ parallel
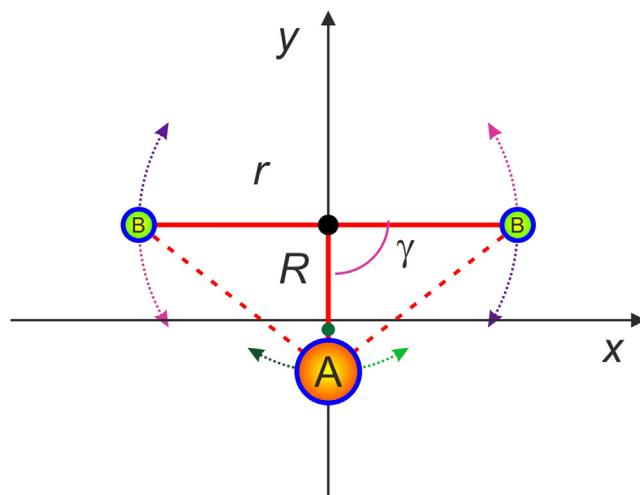

Fig. 4. Jacobi vectors (r and R) in symmetric Jacobi embeddings. The movement of the unfixed vector is indicated with dark/light green arrows for the symmetric Jacobi r embedding, and with pink/purple arrows for the symmetric Jacobi R embedding.

with the body-fixed $\hat{y}$ axis. Both Jacobi embedding choices are very popular.

Regarding the vibrational motions, the pure symmetric subspace is the same for all symmetric embeddings, including the three linear as well as the two symmetric Jacobi embeddings. Thus, Eq. (10) is still applicable here. Note that the length $r = |\vec{r}|$ is determined by Δx, whereas $R = |\vec{R}|$ is determined by Δy. On the other hand, the pure asymmetric stretching motion is no longer linear. Instead, we use γ—i.e., the angle between the two Jacobi vectors—as the asymmetric vibration coordinate (Fig. 4), with $\gamma = \pi/2$ corresponding to zero asymmetric displacement (i.e., to the C_{2v} starting geometry). Since r and R are both constant under pure asymmetric stretching, the asymmetric subspaces for both symmetric Jacobi embeddings are *circular*, rather than linear, as per Fig. 4. Nevertheless, it turns out that the full vibrational space is actually linear (Section 2.5)—although we do not refer to these as "linear embeddings."

It is straightforward to work out the individual particle positions $\vec{r}$ under arbitrary vibrational displacements. For sJrE, these are as follows:

$$
\begin{aligned}
\vec{r}_1 &= (-(x_0 + \Delta x) - (y_0 + \Delta y)\cos\gamma, (y_0 + \Delta y)\sin\gamma, 0) \\
\vec{r}_2 &= ((x_0 + \Delta x) - (y_0 + \Delta y)\cos\gamma, (y_0 + \Delta y)\sin\gamma, 0) \\
\vec{r}_A &= \left(\left[\frac{2m}{M}\right](y_0 + \Delta y)\cos\gamma, -\left[\frac{2m}{M}\right](y_0 + \Delta y)\sin\gamma, 0\right).
\end{aligned}
\tag{16}
$$

Note that since $\vec{r}$ lies along the B_1–B_2 "bond", the sJrE embedding might also be called the "valence BB" embedding.

For the sJRE embedding, the individual particle positions are as follows:

$$
\begin{aligned}
\vec{r}_1 &= (-(x_0 + \Delta x)\sin\gamma, (y_0 + \Delta y) + (x_0 + \Delta x)\cos\gamma, 0) \\
\vec{r}_2 &= ((x_0 + \Delta x)\sin\gamma, (y_0 + \Delta y) - (x_0 + \Delta x)\cos\gamma, 0) \\
\vec{r}_A &= \left(0, -\left[\frac{2m}{M}\right](y_0 + \Delta y), 0\right).
\end{aligned}
\tag{17}
$$

Note that atom A is not displaced at all under pure asymmetric stretching.

2.5. Asymmetric embeddings

On the face of it, there might appear to be little point in working in an *asymmetric* embedding—i.e., one that does not respect the B_1–B_2 permutation symmetry. However, it will be useful for pedagogical purposes to compare the symmetric embeddings described above with several standard asymmetric ones, which in any event become relevant for asymmetric ABC molecules.

Let us first reconsider the choice of the reference geometry and orientation. As discussed in Section 2.1, the body-fixed $(\hat{x}, \hat{y}, \hat{z})$ axes can be defined for *all* embeddings, including asymmetric embeddings. However, for the asymmetric embeddings it is better to work with the rotated axes $(\hat{x}', \hat{y}', \hat{z}')$, obtained by applying a rotation as per Eq. (4), in order to align one of the axes with a relevant molecule vector (see Fig. 1). In this manner, we extend the definition of the rotated $(\hat{x}', \hat{y}', \hat{z}')$ axes to all geometries, i.e., not just to the reference geometry.

In the *valence AB embedding* (or alternatively valence r_1 embedding, Vr$_1$E), the $(\hat{x}', \hat{y}', \hat{z}')$ axes are rotated about the $\hat{z}$ axis such that $\hat{x}'$ lies parallel to the A–B_1 bond. In this embedding, displacements of the B_2 atom form a linear subspace. These displacements correspond to symmetric bending and A–B_2 stretching motions. Displacements of B_1, though limited to the $\hat{x}'$ direction, also form a linear subspace. Interestingly, the two subspaces do not affect one another, so that the *combined* vibrational space is also linear in this case. Actually, this is not surprising: the A–B_1 valence bond

vector is also the $\vec{r}$ vector for the *asymmetric* Jacobi coordinate configuration corresponding to AB$_1$ + B$_2$; accordingly, the valence AB bond embedding is also the "asymmetric Jacobi r" embedding (aJrE).

The *Radau AB embedding* (or alternatively Radau r_1 embedding, Rr$_1$E) is defined similarly to the valence AB embedding, except that it is the B_1 Radau vector that is taken to lie parallel to the body-fixed $\hat{x}'$ axis, via a suitable, geometry-dependent $\hat{z}$-axis rotation. Note that in the $(m/M) \to 0$ limit the Radau and valence AB embeddings approach each other.

Another asymmetric embedding is that based on the asymmetric (a) Jacobi $\vec{R}$ vector—i.e., the vector which points from the A–B_1 center of mass to B_2. The *asymmetric Jacobi R embedding* (aJRE) is defined via a geometry-dependent $\hat{z}$-axis rotation, $(\hat{x}, \hat{y}, \hat{z}) \to (\hat{x}', \hat{y}', \hat{z}')$, such that $\hat{y}'$ lies parallel to the asymmetric Jacobi $\vec{R}$ vector. As in the case of sJRE, this embedding gives rise to a curved asymmetric displacement space, although the full vibrational space is linear.

Our final asymmetric embeddings comprise the Jacobi vector analogs of the VBE, or *Jacobi bisector embeddings*, wherein the bisector of the angle between the two Jacobi vectors defines the $\hat{y}$ axis. There are two such embeddings for AB$_2$ molecules, one corresponding to the symmetric Jacobi vectors (sJBE), and the other to the asymmetric Jacobi vectors (aJBE). Note that *both* embeddings are actually "asymmetric", in the sense defined here.

3. Classical rovibrational kinetic energy

3.1. The **g** tensor

The total classical kinetic energy, as expressed in Cartesian coordinates $\vec{r}_n$ for a set of particles n with mass m_n, is given by

$$
T_{\text{total}} = \sum_{n=1}^{N} \frac{m_n}{2}\vec{\dot{r}}_n \cdot \vec{\dot{r}}_n = \frac{m}{2}\vec{\dot{r}}_1 \cdot \vec{\dot{r}}_1 + \frac{m}{2}\vec{\dot{r}}_2 \cdot \vec{\dot{r}}_2 + \frac{M}{2}\vec{\dot{r}}_A \cdot \vec{\dot{r}}_A,
\tag{18}
$$

where the first form applies to a generic molecule with N atoms, and the second form to the specific case of AB$_2$ triatomics. By transforming to translation-rotation-vibration coordinates, the COM translational motion separates exactly from the rotation-vibration motions, and can be ignored. In tensor form, the resultant rotation-vibration kinetic energy becomes

$$
T = \frac{1}{2}\dot{\mathbf{q}}^T \cdot \mathbf{g} \cdot \dot{\mathbf{q}},
\tag{19}
$$

where $\dot{\mathbf{q}}$ is a list of the vibration-then-rotation coordinate velocities, $\dot{\mathbf{q}} = (\dot{q}_1, \dot{q}_2, \ldots, \dot{\theta}_x, \dot{\theta}_y, \dot{\theta}_z)$, and $\mathbf{g}$ is a tensor. Here, q_i denote the vibrational coordinates and $\theta_\alpha = q_\alpha$, with $\alpha = \{x, y, z\}$, refer to the rotational space.

Note that every tensor element of $\mathbf{g}$ depends only on the geometry—that is, on the values of the vibrational coordinates, q_i, and not on θ_α. Moreover, due to the division of $\dot{\mathbf{q}}$ components into vibration and rotation subsets, the $\mathbf{g}$ tensor necessarily adopts a block-structured form,

$$
\mathbf{g} = \begin{pmatrix} \mathbf{g}_V & \mathbf{g}_{VR} \\ \mathbf{g}_{VR}^T & \mathbf{g}_R \end{pmatrix}.
\tag{20}
$$

Explicit expressions for the individual $\mathbf{g}$ tensor elements are provided in Appendix A.

Note that different embeddings give rise to different rotation-vibration coordinate systems, and therefore to different $\mathbf{g}$ tensor elements. In addition, all tensor elements depend on the geometry. In all embeddings, however, the 3×3 rotation tensor $\mathbf{g}_R$, for a given geometry, is just the usual moment-of-inertia tensor.

3.2. The **G** tensor

3.2.1. Generic form

To obtain a Hamiltonian, the rotation-vibration kinetic energy must be reexpressed using the canonically conjugate momenta, $\mathbf{p} = (p_1, p_2, \ldots, J_x, J_y, J_z)$, rather than $\dot{\mathbf{q}}$. The result is

$$T = \frac{1}{2}\mathbf{p}^T \cdot \mathbf{G} \cdot \mathbf{p}, \tag{21}$$

where

$$\mathbf{G} = \mathbf{g}^{-1} = \begin{pmatrix} \mathbf{G}_{\mathrm{V}} & \mathbf{G}_{\mathrm{VR}} \\ \mathbf{G}_{\mathrm{VR}}^T & \mathbf{G}_{\mathrm{R}} \end{pmatrix} \tag{22}$$

is defined in Appendix A.

When the rotation-vibration coupling $\mathbf{g}_{\mathrm{VR}}$ is zero, $\mathbf{g}$ becomes block diagonal, so that each diagonal block inverts independently:

$$\mathbf{G}_{\mathrm{V}} = \mathbf{g}_{\mathrm{V}}^{-1}; \quad \mathbf{G}_{\mathrm{VR}} = \mathbf{0}; \quad \mathbf{G}_{\mathrm{R}} = \mathbf{g}_{\mathrm{R}}^{-1}. \tag{23}$$

Thus, in this case the CC $\mathbf{G}_{\mathrm{VR}}$ vanishes. Furthermore, $\mathbf{G}_{\mathrm{R}}$ can be called "geometric"—meaning simply that it is the inverse of the moment-of-inertia tensor. More generally, i.e., when $\mathbf{g}_{\mathrm{VR}}$ and $\mathbf{G}_{\mathrm{VR}}$ are *not* zero, the rotation-vibration coupling modifies the form of $\mathbf{G}_{\mathrm{R}}$ as follows:

$$\mathbf{G}_{\mathrm{R}} = \left(\mathbf{g}_{\mathrm{R}} - \mathbf{g}_{\mathrm{VR}}^T \cdot \mathbf{g}_{\mathrm{V}}^{-1} \cdot \mathbf{g}_{\mathrm{VR}}\right)^{-1}. \tag{24}$$

This implies, for example, that the three rotational constants (defined as the eigenvalues of $\mathbf{G}_{\mathrm{R}}$) are no longer equal to the inverses of the three moments of inertia, as is true in the geometric case.

3.2.2. Rotational kinetic energy for AB_2 molecules

For all triatomic molecules, including the AB_2 case considered here, the geometry is necessarily planar, leading to further specialized structure in $\mathbf{g}_{\mathrm{R}}$ and $\mathbf{G}_{\mathrm{R}}$. In particular, both tensors themselves block diagonalize into planar (xy) and perpendicular (z) contributions:

$$\mathbf{g}_{\mathrm{R}} = \begin{pmatrix} g_{xx}^{\mathrm{R}} & g_{xy}^{\mathrm{R}} & 0 \\ g_{yx}^{\mathrm{R}} & g_{yy}^{\mathrm{R}} & 0 \\ 0 & 0 & g_{zz}^{\mathrm{R}} \end{pmatrix}; \quad \mathbf{G}_{\mathrm{R}} = \begin{pmatrix} G_{xx}^{\mathrm{R}} & G_{xy}^{\mathrm{R}} & 0 \\ G_{yx}^{\mathrm{R}} & G_{yy}^{\mathrm{R}} & 0 \\ 0 & 0 & G_{zz}^{\mathrm{R}} \end{pmatrix}. \tag{25}$$

The planar contributions—i.e., the upper-left 2×2 blocks in Eq. (25) above—will be denoted $\mathbf{g}_{xy}$ and $\mathbf{G}_{xy}$.

For all planar molecules, the perpendicular moment of inertia, I_z, is equal to the sum of the two planar moments of inertia, I_x and I_y [note: the planar principal axes associated with I_x and I_y do not need to coincide with $\hat{x}$ and $\hat{y}$]. Since $\mathbf{g}_{\mathrm{R}}$ is always geometric, $I_z = I_x + I_y = g_{zz}^{\mathrm{R}}$—regardless of the choice of embedding. In contrast, the individual $\mathbf{g}_{xy}$ tensor elements vary from one embedding to the next; however, the two $\mathbf{g}_{xy}$ eigenvalues are always equal to the two planar moments, I_x and I_y.

For $\mathbf{G}_{\mathrm{R}}$, there is more variability, since this tensor need not generally be geometric. Nevertheless, even for $\mathbf{G}_{\mathrm{R}}$, it can be shown that for *all* geometries and embeddings, the $\mathbf{G}_{xy}$ block is *always* geometric. Thus, $\mathbf{G}_{xy} = \mathbf{g}_{xy}^{-1}$ and it takes the explicit form

$$\mathbf{G}_{xy} = \begin{pmatrix} \frac{m(x_1+x_2)^2 + M(x_1^2+x_2^2)}{m(2m+M)(x_2y_1-x_1y_2)^2} & \frac{m(x_1+x_2)(y_1+y_2)+M(x_1y_1+x_2y_2)}{m(2m+M)(x_2y_1-x_1y_2)^2} \\ \frac{m(x_1+x_2)(y_1+y_2)+M(x_1y_1+x_2y_2)}{m(2m+M)(x_2y_1-x_1y_2)^2} & \frac{m(y_1+y_2)^2+M(y_1^2+y_2^2)}{m(2m+M)(x_2y_1-x_1y_2)^2} \end{pmatrix}. \tag{26}$$

Consequently, the two planar rotational constants, A_x and A_y, are always equal to the inverses of the smallest two moments of inertia—i.e., $A_x = 1/I_x$ and $A_y = 1/I_y$, where A_x and A_y are the eigenvalues of $\mathbf{G}_{xy}$. Eq. (26) is completely general, across all geometries and embeddings. Note, however, that for all C_{2v} geometries and all sym-

metric embeddings, the off-diagonal G_{xy}^{R} tensor element vanishes. In this case, $A_x = 1/I_x = G_{xx}^{\mathrm{R}}$ and $A_y = 1/I_y = G_{yy}^{\mathrm{R}}$.

Since $\mathbf{G}_{\mathrm{R}}$ is in general not geometric, the *only* place where the non-geometric character can manifest is in the third rotational constant, $A_z = G_{zz}^{\mathrm{R}}$. Thus, in general, $A_z \neq 1/I_z$, so $G_{zz}^{\mathrm{R}} \neq 1/g_{zz}^{\mathrm{R}}$. The difference between these two quantities—i.e., the "CC correction", $(G_{zz}^{\mathrm{R}} - 1/g_{zz}^{\mathrm{R}})$—arises solely due to non-zero CC. Indeed, based on Eq. (24), it can be shown that in general *only* the z component of the CC—i.e., the G_{iz}^{VR} tensor elements—are non-zero. Note also that A_z need not in general be the smallest rotational constant, though certainly it is smallest in the geometric case.

Given its close relation to $\mathbf{g}_{\mathrm{VR}}$, it is reasonable to consider the magnitude of the CC correction quantity $(G_{zz}^{\mathrm{R}} - 1/g_{zz}^{\mathrm{R}})$ as a quantitative measure of the relative magnitude of the Coriolis coupling. This choice is particularly useful in that it is a (vibrational) *coordinate-independent metric*. Earlier authors simply examined the $\mathbf{G}_{\mathrm{VR}}$ tensor elements themselves as a direct measure of the extent of CC [43,44]. However, this procedure is far from ideal, as the tensor element values depend on the choice of vibrational coordinates, which in reality has *no impact whatsoever* on the CC—and therefore, no impact (in principle) on an exact or CFA calculation.

What is needed is a coordinate-independent measure for the magnitude of the CC—i.e., one that provides the same result, no matter what coordinates are used. Likewise, this metric should be invariant with respect to a *global* rotation of the body-fixed axes, (x, y, z), since such a rotation changes nothing fundamental about the embedding. In Ref. [45], we have proposed the quantity $\|\mathbf{G}_{\mathrm{R}} - \mathbf{g}_{\mathrm{R}}^{-1}\|_{\mathrm{F}}$ (FNGR)—i.e., the Frobenius norm of the difference between the rotational and inverse moment-of-inertia tensors—as a suitable metric. For the special case of triatomic molecules that lie in the (x, y) plane, this quantity becomes just $|G_{zz}^{\mathrm{R}} - 1/g_{zz}^{\mathrm{R}}|$, as should be clear from the arguments given above. Note that FNGR is always positive or zero, vanishing only when $\mathbf{G}_{\mathrm{VR}}$ (or $\mathbf{g}_{\mathrm{VR}}$) vanish. Thus, the smaller the value of FNGR for a given geometry and embedding, the smaller the CC, and consequently the better the embedding is expected to perform in a CFA calculation—at least for rovibrational states that have significant probability at the given geometry. More generally, by comparing FNGR norm values for different embeddings across a range of relevant geometries, one can gain a sense of which embedding should perform best overall.

3.3. **G** expressions for specific embeddings

3.3.1. Linear embeddings

For the three linear embeddings, EE, VBE, and RBE, it is convenient to replace the asymmetric displacement parameter Δ with $\mu = \Delta \cos \epsilon$. Then, Eq. (13) becomes

$$\begin{aligned} \Delta \vec{r}_1 &= (-\Delta x + \mu, \Delta y - \mu \tan \epsilon, 0) \\ \Delta \vec{r}_2 &= (\Delta x + \mu, \Delta y + \mu \tan \epsilon, 0) \\ \Delta \vec{r}_A &= \left(-\left[\frac{2m}{M}\right]\mu, -\left[\frac{2m}{M}\right]\Delta y, 0\right). \end{aligned} \tag{27}$$

Likewise, from Eqs. (34) and (26) we obtain

$$\mathbf{G}_{\mathrm{R}} = \begin{pmatrix} \frac{\mu^2 + (M/(2m+M))(x_0+\Delta x)^2}{2m[\mu^2 \tan \epsilon - (x_0+\Delta x)(y_0+\Delta y)]^2} & \frac{\mu[(y_0+\Delta y)+(M/(2m+M))(x_0+\Delta x)\tan \epsilon]}{2m[\mu^2 \tan \epsilon - (x_0+\Delta x)(y_0+\Delta y)]^2} & 0 \\ \frac{\mu[(y_0+\Delta y)+(M/(2m+M))(x_0+\Delta x)\tan \epsilon]}{2m[\mu^2 \tan \epsilon - (x_0+\Delta x)(y_0+\Delta y)]^2} & \frac{(M/(2m+M))\mu^2 \tan^2 \epsilon + (y_0+\Delta y)^2}{2m[\mu^2 \tan \epsilon - (x_0+\Delta x)(y_0+\Delta y)]^2} & 0 \\ 0 & 0 & \frac{1+(M/(2m+M))\tan^2 \epsilon}{2m[(x_0+\Delta x)+(y_0+\Delta y)\tan \epsilon]^2} \end{pmatrix}. \tag{28}$$

Note that $G_{xy}^{\mathrm{R}} = 0$ for all C_{2v} geometries (i.e., for $\mu = 0$), as predicted. Furthermore, the three diagonal elements, $G_{xx}^{\mathrm{R}}, G_{yy}^{\mathrm{R}}$, and G_{zz}^{R}, are in

general embedding- (*i.e.*, ϵ)-dependent, except when $\mu = 0$, in which case $G^R_{xx} = A_x$ and $G^R_{yy} = A_y$. However, even for C_{2v} geometries, G^R_{zz} depends on the embedding.

Equation (28) applies to all linear embeddings; specific forms may be obtained by substituting $\tan\epsilon$ via Eq. (12), (14), or (15), as appropriate—or indeed, any other form. Note that RBE turns out to be a very special choice, in that $G^R_{zz} = A_z = 1/I_z$ when $\mu = 0$, so that $\mathbf{G}_R$ is geometric. Thus, *RBE is the only linear embedding for which all CC vanishes, for all C_{2v} geometries*. Specifically, we have for the $\mu = 0$ RBE case,

$$\mathbf{G}_R = \begin{pmatrix} \frac{M}{2m(2m+M)(y_0+\Delta y)^2} & 0 & 0 \\ 0 & \frac{1}{2m(x_0+\Delta x)^2} & 0 \\ 0 & 0 & \frac{M}{2m\left[M(x_0+\Delta x)^2+(2m+M)(y_0+\Delta y)^2\right]} \end{pmatrix}. \quad (29)$$

For EE, CC in general vanishes only at a single point, at the reference geometry. More generally, "flexible" embeddings can be contrived for which CC vanishes along a 1D curve of geometries [55]. Here, in the special case of AB_2 molecules, however, we find that RBE results in $\mathbf{G}_{VR} = \mathbf{0}$ over the entire 2D space of pure symmetric displacements, $(\Delta x, \Delta y)$.

In contrast, VBE is not geometric even at the reference geometry itself. Even here, then, the CC does not vanish, and $G^R_{zz} \neq 1/I_z$. In fact, we find

$$G^R_{zz} = \left(\frac{M}{2m}\right)\frac{M^3 x_0^2 + (2m+M)^3 y_0^2}{\left[M^2 x_0^2 + (2m+M)^2 y_0^2\right]^2}, \quad (30)$$

for the VBE at the reference geometry, which is not consistent with Eq. (29).

3.3.2. Jacobi and Radau bond embeddings

All of the remaining embeddings considered here, both symmetric and asymmetric ones, are Jacobi or Radau bond embeddings, for which a single Jacobi/Radau vector is used to define the body-fixed frame (recall that *a*JrE is equivalent to VBE). More generally, these embeddings are just special cases of a one-parameter family of coordinate systems, related to one another by what are called "democracy transformations" [59]. For each such coordinate system, there are two vectors, either of which can be used to define an embedding, in analogy with what is done with Jacobi and Radau vectors. The lengths of the two vectors, together with the angle between them, γ, can also serve as a convenient choice of vibrational coordinates. However, it must be reemphasized that none of the properties of specific embeddings, as discussed here and in Section 3.3.1, depends on the choice of the vibrational coordinates.

For the *s*JrE embedding, the explicit $\mathbf{G}_R$ tensor elements are

$$\mathbf{G}_R = \left(\frac{M}{2m}\right)\begin{pmatrix} \frac{\cot^2\gamma}{M(x_0+\Delta x)^2} + \frac{\csc^2\gamma}{(2m+M)(y_0+\Delta y)^2} & -\frac{\cot\gamma}{M(x_0+\Delta x)^2} & 0 \\ -\frac{\cot\gamma}{M(x_0+\Delta x)^2} & \frac{1}{M(x_0+\Delta x)^2} & 0 \\ 0 & 0 & \frac{1}{M(x_0+\Delta x)^2} \end{pmatrix}. \quad (31)$$

Note that for all C_{2v} geometries $G^R_{xy} = 0$, implying that $G^R_{xx} = A_x = 1/I_x$ and $G^R_{yy} = A_y = 1/I_y$. Note further that for all geometries $G^R_{zz} = G^R_{yy}$, with these quantities being independent of both Δy and γ. In fact, they are equal to A_y for the corresponding C_{2v} starting geometry (corresponding to setting $\gamma = \pi/2$).

For the *s*JRE embedding, we have a very similar situation:

$$\mathbf{G}_R = \left(\frac{M}{2m}\right)\begin{pmatrix} \frac{1}{(2m+M)(y_0+\Delta y)^2} & -\frac{\cot\gamma}{(2m+M)(y_0+\Delta y)^2} & 0 \\ -\frac{\cot\gamma}{(2m+M)(y_0+\Delta y)^2} & \frac{\csc^2\gamma}{M(x_0+\Delta x)^2} + \frac{\cot^2\gamma}{(2m+M)(y_0+\Delta y)^2} & 0 \\ 0 & 0 & \frac{1}{(2m+M)(y_0+\Delta y)^2} \end{pmatrix}. \quad (32)$$

Perhaps not surprisingly, Eq. (32) is like Eq. (31), but with the roles of x and y reversed. In particular, now $G^R_{zz} = G^R_{xx}$. Again, these quantities are independent of γ (as well as Δx), and are equal to A_x for the corresponding C_{2v} starting geometry, since once again, $G^R_{xy} = 0$ for all C_{2v} geometries.

The above-mentioned characteristics are not only true for *s*JrE and *s*JRE. It can be shown that for *any* Jacobi, Radau, or democracy-transformed bond embeddings defined above, and for all geometries, two out of the three diagonal tensor elements of $\mathbf{G}_R$ are identical. This follows from the fact that the rovibrational kinetic energy T is orthogonal (*i.e.*, there are no cross terms) when expressed in terms of the Cartesian components of the two coordinate vectors. Though true in general, here we focus mainly on AB_2 molecules, and the symmetric Jacobi embeddings.

For C_{2v} geometries (or all geometries, if G^R_{xy} is ignored), the equivalence of two out of three rotational constants implies that the rotational kinetic energy has the form of a *symmetric rigid rotor*. This is true, despite the fact that planar molecules do not have *any* symmetric rigid-rotor geometries (*i.e.*, those for which $I_z = I_x$ or $I_z = I_y$, as opposed to "symmetric" in the C_{2v} sense) because $I_z = I_x + I_y$. Put another way, the geometric value of $A_z = G^R_{zz}$ [*i.e.*, $1/(I_x + I_y)$] is less than both A_x and A_y—and thus also less than either G^R_{xx} and G^R_{yy}.

The above arguments also extend to non-C_{2v} geometries, because the values of G^R_{xx} and G^R_{yy} are both larger than the lesser value of A_x and A_y. Thus, once again, the geometric value of A_z must be less than the actual value of A_z (which equals either G^R_{xx} or G^R_{yy}). Thus, the $\mathbf{G}_R$ tensor is never geometric, which immediately implies that *CC is never zero in a Jacobi or Radau bond embedding*. More specifically, the difference between the actual and the geometric $A_z = G^R_{zz}$ values must therefore be positive, and sufficiently large as to transform A_z from the geometric value up to either G^R_{xx} or G^R_{yy}.

All of this implies that if the most relevant molecular geometries are not especially symmetric-rotor-like to begin with—or if they correspond to an oblate symmetric rotor ($I_x \approx I_y$)—then the CC will be significant. If the geometries are close to a prolate symmetric rotor, then the CC could be quite small if G^R_{zz} equals the smaller of the other two diagonal elements; otherwise, it will be rather large. For the primary AB_2 system considered here—*i.e.*, $H_2^{16}O$—the reference geometry is only approximately prolate symmetric rotor, with $G^R_{xx} = 1/I_x = 54.80$ cm^{-1}, $G^R_{yy} = 1/I_y = 29.18$ cm^{-1} and $1/I_z = 19.04$ cm^{-1}. We therefore expect CC to be substantially larger for *s*JRE than for *s*JrE.

Now, we briefly consider the Radau and asymmetric Jacobi embeddings (including valence AB). Note that the body-fixed axes [*i.e.*, $(\hat{x}', \hat{y}')$ from Section 2.5] are no longer aligned with the principal axes for the reference geometry. Accordingly, G^R_{xx} and G^R_{yy} (technically $G^R_{x'x'}$ and $G^R_{y'y'}$, but we drop the primes for convenience) take on less extremal values than for the symmetric Jacobi embeddings—although it is still true that $G^R_{xx} + G^R_{yy} = A_x + A_y$. In any case, for all asymmetric embeddings of this kind, we expect $\mathbf{G}_{VR}$ to lie "intermediate" in magnitude between the two symmetric Jacobi embeddings.

On the other hand, for any Jacobi or Radau bond embedding, we expect CC to be larger in general than for the three linear embeddings. There are two reasons for this. First, for all Jacobi and Radau embeddings, the rotational kinetic energy is forced to adopt a symmetric rotor form for C_{2v} geometries—even though the true geometries are never of this form. The linear embeddings have no such symmetric-rotor constraint. Second, for at least two linear embeddings, there are relevant geometries for which $\mathbf{G}_{VR} = \mathbf{0}$.

4. Quantum Hamiltonian and its approximations

4.1. Overview

Having determined the form of the classical rovibrational kinetic energy, T, through specification of the $\mathbf{G}$ tensor for various embeddings, the next step is to construct the corresponding quantum Hamiltonian. To this end, the rovibrational coordinates $\hat{\mathbf{q}} = (\hat{q}_1, \hat{q}_2, \dots, \hat{\phi}, \hat{\theta}, \hat{\chi})$ and the conjugate momenta $\hat{\mathbf{p}} = (\hat{p}_1, \hat{p}_2, \dots, \hat{J}_x, \hat{J}_y, \hat{J}_z)$ become operators. Since not all of these operators commute, the operator ordering matters, and must thus be dealt with. For our purposes, for which only the $\mathbf{G}_R$ and $\mathbf{G}_{VR}$ contributions to the quantum rovibrational KEO are considered explicitly, the operator ordering implied by the form of Eq. (21) is in fact correct as is. In particular, since the $\mathbf{G}$ tensor elements depend only on the vibrational coordinates $\hat{q}_i$, these commute with the $\hat{J}_\alpha$ components, as do their conjugate vibrational momenta, $\hat{p}_i$. Also, the $\hat{J}_\alpha$ do not commute with each other. As a consequence, all non-commuting $\mathbf{G}_R$ and $\mathbf{G}_{VR}$ contributions to $\hat{T}$ depend only linearly on $\hat{p}_i$ or $\hat{J}_\alpha$—and are thus automatically properly symmetrized, due to the fact that $\mathbf{G}$ is real symmetric [60].

If the exact rovibrational KEO $\hat{T}$ is used, and the resulting rovibrational Hamiltonian is represented in some full-dimensional basis set, then, in principle, all embeddings will give rise to the same rovibrational eigenstates. In practice, the numerical convergence in terms of basis size may depend somewhat on the choice of embedding [61], but for the present purpose, we will, for simplicity, assume comparable basis sizes across all embeddings. In particular, the choice of vibrational basis set—like the choice of vibrational coordinates—is independent of embedding, so may as well be presumed to be the same for each. For the rotational space, the usual Wigner rotation-function basis, $|JKM\rangle$ [30], can be used, whose complete determination requires only the specification of the body-fixed projection axis (for K), in addition to the embedding itself.

Of course, the choice of embedding becomes much more relevant when *approximations* are introduced. Similar to Ref. [45], we consider a sequence of increasingly severe approximations, based on particular embeddings. As a rule, as we progress from one approximation to the next, the symmetry of the problem increases, while the numerical cost and the accuracy decrease. We shall consider all of these aspects for each of the embeddings introduced, but only in the context of AB$_2$ molecules.

The approximations are defined as follows. As discussed, the *Coriolis-free* approximation (CFA) is obtained by ignoring the $\mathbf{G}_{VR}$ (or $\hat{T}_{VR}$) contribution to $\hat{T}$. The resultant approximate Hamiltonian is then a sum of pure vibration and rotation contributions, with $\hat{T}^{CFA} = \hat{T}_V + \hat{T}_R$. As discussed, however, separability is still not achieved in practice, because $\hat{T}_R$ depends parametrically on the geometry—and hence on the vibrational coordinates. If, in addition to discarding $\mathbf{G}_{VR}$, we also set $G_{xy}^R = 0$, then we are left with the *diagonal* $\mathbf{G}_R$ approximation (DGRA). This additional approximation introduces a new permutation symmetry into the Hamiltonian, which serves as a nearly perfect "good" quantum number, suitable

for labeling the exact rovibrational states. Finally, the *generalized CS* approximation (GCSA) is obtained by discarding all remaining K coupling in the $|JKM\rangle$ representation, resulting in another good quantum number, the rotational quantum number K. For decades, the CS approximation has been widely used in the quantum dynamics community [46–54] in the context of Jacobi and Radau coordinate representations [59]. To the best of our knowledge, we are the first to find a natural way to generalize the CS approximation for arbitrary embeddings.

4.2. The Coriolis-free approximation (CFA)

4.2.1. Symmetry

For all embeddings, and all exact and approximate Hamiltonians considered here, the rotational quantum numbers J and M are both rigorously good. The Hamiltonian matrix block-diagonalizes with respect to these quantum numbers, with $(2J + 1)$ identical M blocks for each J value. Without loss of generality, going forward, we work with fixed J value and with $M = 0$. For each J value, the corresponding $M = 0$ Hamiltonian matrix block $\tilde{H}^J$ itself adopts a $(2J + 1) \times (2J + 1)$ (sub) block structure, with respect to the third rotational quantum number, K. As discussed, K is the (non-parity-adapted) projection along some body-fixed axis, which need not be (and generally should not be) $\hat{z}$. Accordingly, we use body-fixed axis labels $(\hat{a}, \hat{b}, \hat{c})$ for purposes of defining the $|JKM\rangle$ basis, with K associated with $\hat{c}$. Note that $\tilde{H}^J$ is at most *block-pentadiagonal*, meaning that the K–K' subblock, $\tilde{H}_{KK'}^J$, vanishes unless $|K - K'| \leqslant 2$. The $|K - K'| = 2$ subblocks arise only from the $\hat{J}_a^2, \hat{J}_b^2$, and $\hat{J}_a\hat{J}_b$ contributions to $\hat{T}_R$, whereas the $|K - K'| = 1$ subblocks come from the $\hat{J}_a\hat{J}_c$ and $\hat{J}_b\hat{J}_c$ $\hat{T}_R$ contributions to $\tilde{T}_R$, as well as from $\hat{T}_{VR}$.

In addition to J and M, the overall parity, $p = \pm 1$, is also a rigorously good quantum number. Through parity-symmetry adaptation, it is possible to subdivide $\tilde{H}^J$ into decoupled positive- and negative-parity symmetry blocks, thereby effectively reducing the basis size by a factor of two. In general, an n-fold reduction of the basis gives rise to a computational savings of n^2, because the computational effort required for each symmetry-adapted diagonal subblock is $1/n^3$ that of the original, but there are n such diagonal subblocks in all.

For AB$_2$ systems, the true Hamiltonian is also characterized by permutation symmetry, $\varepsilon = \pm 1$, associated with the B$_1$–B$_2$ exchange, which can lead to a further factor-of-two reduction, *i.e.*, $n = 4$. However, it should be emphasized that permutation symmetry is only respected by the symmetric embeddings. For the asymmetric embeddings, it may not be possible to exploit this symmetry for the exact Hamiltonian—and for the approximate Hamiltonians it may not exist at all.

Next, we discuss the specific case of the CFA, obtained by setting $\hat{T}_{VR}$ or $\mathbf{G}_{VR}$ to zero. In this particular case, applying the approximation does not lead to any additional symmetries, beyond those discussed above. Furthermore, the CFA is not "separable", in the sense of allowing the rotational and vibrational problems to be solved separately. Consequently, there are no numerical simplifications that can be applied, beyond those already discussed above. Nevertheless, in practice, CFA appears to lead to a significant reduction of CPU cost, by a factor of 3 to 6, in comparison with the corresponding exact calculation. Additionally, the CFA may well offer some advantages for purposes of state labeling; however, this possibility lies outside the purview of the present work.

4.2.2. Accuracy and simplicity

As the least severe of the approximations considered here, the CFA is certainly expected to be the most accurate approximation.

However, in practice, the performance exhibits a substantial dependence on the embedding, as well as on the particular vibrational parent state. Specific embeddings are discussed below.

In general, we expect the performance of the CFA to correlate with the magnitude of the CC, as determined by FNGR, $\|\mathbf{G}_R - \mathbf{g}_R^{-1}\|_F$. This correlation is both embedding- and geometry-dependent. However, we also expect VBE and EE to show similar performance trends, given Eqs. (12) and (14), and the light-heavy-light nature of $H_2^{16}O$ (i.e., $(2m/M) \approx 0.125$), resulting in ϵ values for the two embeddings that are not that dissimilar. As discussed, RBE lies "halfway" between the other two linear symmetric embeddings [see Eq. (15)], and for $H_2^{16}O$ it is expected to perform similarly to the others.

In the Eckart frame, we know that $\|\mathbf{G}_R - \mathbf{g}_R^{-1}\|_F = 0$ for the reference geometry. If the reference geometry corresponds to the global minimum of the PES (as in the specific case of $H_2^{16}O$ considered here), then we can expect the greatest accuracy for the pure rotational states, corresponding to the vibrational ground state, (000). However, the error might be expected to rise fairly rapidly with increasing rovibrational excitation. Not only is $\|\mathbf{G}_R - \mathbf{g}_R^{-1}\|_F \neq 0$ outside the reference geometry, the fact that the vibrational displacement space is completely linear in the Eckart case suggests that for large-amplitude motions this choice of embedding may not be the best (i.e., FNGR may become substantial).

In contrast, the VBE choice is a bit more physically motivated, even when the vibrational displacements are substantial. Chemical intuition suggests that the vibrational dynamics are often well described using the valence bond picture, and the B–A–B valence bond angle bisector is certainly relevant given the identical B atoms. That said, even at the reference geometry, $\|\mathbf{G}_R - \mathbf{g}_R^{-1}\|_F \neq 0$ for the VBE. This suggests that VBE will be less accurate than EE for the lowest-lying states, but may maintain its accuracy better further up in the spectrum.

As to RBE, this choice is physically motivated, like VBE. Moreover, like EE, it has $\|\mathbf{G}_R - \mathbf{g}_R^{-1}\|_F = 0$ at the reference geometry. On the other hand, the Radau bisector embedding also has a considerable advantage over the other two linear embeddings in that $\|\mathbf{G}_R - \mathbf{g}_R^{-1}\|_F = 0$ for a two-dimensional subspace (all symmetric C_{2v} geometries), not just at a single point. We therefore expect RBE to perform the best among the linear embeddings.

For a fair comparison, however, we must point out that, in fact, EE turns out to have $\|\mathbf{G}_R - \mathbf{g}_R^{-1}\|_F = 0$ over a full one-dimensional subspace in the specific case of AB_2 systems (Section 5.2.1). This can be determined from Eqs. (22)–(24) of the operator derived in Ref. [44], although it was not stated in that paper explicitly. In any event, this has especially interesting repercussions when we consider the flexible or "post" Eckart embeddings (FEEs). Introduced by Sayvetz [55], these embeddings are actually designed to provide zero CC over a one-dimensional path extending from the EE reference geometry. The approach enables one to choose the 1D subspace arbitrarily, with different choices leading to different embeddings. In the AB_2 case, we have chosen the 1D path to correspond to varying the bend coordinate, while keeping the stretch coordinates fixed. This gives rise to two different 1D paths, depending on whether valence or Radau coordinates are used. Both the valence and Radau FEEs should perform better than EE, but it remains to be seen which of the two is better and how they compare with RBE. We take this question up again in Section 5.2.1.

With regard to all Jacobi and Radau bond embeddings—both symmetric and asymmetric—we must recall that two out of three diagonal tensor elements of $\mathbf{G}_R$ are always identical. For AB_2 molecules and C_{2v} geometries, this corresponds to symmetric-top-rotor constants. Yet, in reality, there are no planar molecular geometries

that correspond to symmetric rotors, and even the C_{2v} reference geometry for $H_2^{16}O$ is only a "somewhat prolate symmetric top". This implies FNGR values that are at least comparable to the rotational-constant-spacing itself—i.e., on the order of 5–40 cm^{-1} for the systems studied here, which should be much larger than that of any of the linear symmetric embeddings. Moreover, FNGR should never be zero, not even at the reference geometry. Furthermore, the vibrational spaces are all linear, and not tied to any specific geometries, so we expect slowly-varying performance across a broad v and J range.

As an additional prediction, we may expect the two asymmetric Jacobi bond embeddings to always yield similar FNGR values, with those of sJRE and sJrE being always significantly larger or smaller, respectively. This can be explained by the fact the $(\hat{x}', \hat{y}')$ axes are generally far from the principal axes and effectively "randomly" oriented, so that the diagonal tensor elements G_{xx}^R and G_{yy}^R are far from extremal, and on average each equal to $(A_x + A_y)/2$. On the other hand, the symmetric Jacobi embeddings are characterized by $G_{xx}^R \approx A_x$ and $G_{yy}^R \approx A_y$—i.e., the extremal values—across a range of relevant geometries, including the C_{2v} reference geometry. As per Section 3.3.2, we therefore expect symmetric Jacobi r to perform the best, and symmetric Jacobi R the worst, of all of the Jacobi and Radau bond embeddings.

4.3. The diagonal $\mathbf{G}_R$ approximation (DGRA)

4.3.1. Overview

The next rung in our approximation hierarchy is the diagonal $\mathbf{G}_R$ approximation. Formally, DGRA can be defined via the additional removal of all cross terms from the rotational KEO—although in the present context, this amounts to simply setting $G_{xy}^R = 0$. This results in a diagonal $\mathbf{G}_R$ tensor—although the quantum–mechanical matrix representations do not themselves become diagonal (except for the parity-adapted $J = 1$ representation, as in Eq. (35) of Appendix B). Prior to parity adaptation, the approximate $\tilde{H}^J$ matrix remains pentadiagonal, with the non-zero $|K - K'| = 2$ blocks still coming from the $\hat{J}_a^2$ and $\hat{J}_b^2$ contributions. On the other hand, the first off-block diagonal (comprising the $|K - K'| = 1$ blocks) does vanish.

For the asymmetric embeddings, G_{xy}^R can be quite large, as discussed. However, for all of the symmetric embeddings, $G_{xy}^R = 0$ for all C_{2v} geometries, including the reference geometry. Only for large asymmetric displacements do we expect G_{xy}^R to become substantial; accordingly, only for excited asymmetric stretch states do we expect to see a large difference from the CFA, at least for the symmetric embeddings.

In reality, the computed DGRA energy levels turn out to be extremely close to the CFA levels of symmetric embeddings—much more so than might be expected. The reasons for this are explained in Appendix C. In any event, what this means from a practical standpoint is that for symmetric embeddings there is no reason not to use DGRA, if one has already committed to discarding the CC. In comparison with CFA, the additional drawbacks of DGRA are negligible, but the numerical advantages are quite significant.

4.3.2. Symmetry

DGRA also introduces a new symmetry that can be very useful in practice. Not surprisingly, given the discussion of symmetric embeddings above, this has to do with permutation symmetry. Unlike parity, which affects only the rotational states and not the vibrational states (for triatomic systems, at any rate), permutation affects rotation and vibration simultaneously. In the vibrational

space, permutation changes the sign of the asymmetric stretch displacement [*e.g.*, Δ in Eq. (13)], without affecting the symmetric displacements. In the rotational space, the even-$\bar{K}$ basis functions are already adapted for one permutation symmetry, ε, and the odd-$\bar{K}$ basis functions for the other ε (where $\bar{K}$ is the parity-adapted version of the K basis set, *e.g.*, $\bar{K} = \{1^+, 0^+, 1^-\}$ for $J = 1$).

Consider a parity-adapted matrix representation of $\hat{T}_R$, as in Eq. (35). Note that the G_{xy}^R block couples even- and odd-$\bar{K}$ blocks together. Based on the above discussion, this off-diagonal block therefore violates invariance under permutation of the pure rotational space—in fact, under such a permutation, $\tilde{T}_R^{J=1}$ does not remain invariant, but is transformed to $\tilde{T}_R^{J=1^*}$, where $*$ denotes complex conjugation. However, that is fine, because when applied in conjunction with *vibrational* permutation, the G_{xy}^R contribution undergoes a sign change [see, *e.g.*, Eq. (28)] that exactly cancels the effect of the rotational permutation. In other words, *vibrational* permutation symmetry, ε_{vib}, and *rotational* permutation symmetry, ε_{rot}, are not in and of themselves good quantum numbers, only the *total* permutation symmetry—*i.e.*, their product, $\varepsilon = \varepsilon_{rot}\varepsilon_{vib}$—is rigorously conserved.

In practice, this situation can lead to some complications—at the least, one must address permutation symmetry for both rotation and vibration together, as discussed. The situation greatly simplifies in the DGRA, however, because the troublesome G_{xy}^R contribution vanishes altogether. This means that both ε_{rot} and ε_{vib}, *individually*, become good quantum numbers. As a practical benefit, this additional symmetry allows the basis size to be reduced by an additional factor of two, resulting in $n = 8$. Furthermore, because DGRA is so closely related to CFA—which in turn does an excellent job of modeling the exact Hamiltonian, at least for the linear symmetric embeddings—this suggests that ε_{vib} and ε_{rot} are *both* nearly good quantum numbers, that could serve as useful state labels. In fact, this provides a good theoretical justification for the common practice of associating the even-v_3 vibrational quantum states of AB$_2$ molecules with even permutation symmetry, and odd-v_3 states with odd permutation symmetry through the use of the expression $(-1)^{v_3}$. In fact, such labels correspond to ε_{vib}, rather than to ε itself.

4.3.3. Results

Numerical results for the DGRA, as applied to the H$_2^{16}$O system, together with a discussion of key trends, may be found in Sec. II, and in Tables S18 and S19 of the supplementary material. Here, we simply comment that for symmetric embeddings, CFA and DGRA yield eigenvalues that are *extremely* close—*e.g.*, with differences no larger than 0.01 cm^{-1}, across the full range of v values considered. This is remarkable, considering that the magnitude of the discarded G_{xy}^R term can itself be up to 30 cm^{-1}. The theoretical explanation underlying this rather mysterious effect is presented in Appendix C.

4.4. The generalized CS approximation (GCSA)

4.4.1. Symmetry

The centrifugal sudden approximation was introduced—or at least applied—within the chemical physics community as a means of *drastically* reducing the computational cost associated with rovibrational state calculations, especially for large J values. Note that historically, the technique has been applied only when Jacobi or Radau coordinates are used. Here, however, we present a *generalized CS* approximation (GCSA) applicable to any embedding and vibrational coordinate system.

The idea behind GCSA is very simple: for a rovibrational Hamiltonian $\tilde{H}^J$, as expressed in the $|JKM\rangle$ rotational basis, set all off-diagonal K blocks—*i.e.*, $\langle JK'M|\hat{H}|JKM\rangle$ with $K \neq K'$—to zero. The discarded blocks, representing coupling across different K values, are often loosely referred to as "Coriolis coupling", although this is definitely not just $\tilde{T}_{VR}$. In addition, parts of $\tilde{T}_R$ are also included, that depend on both the embedding and the particular body-fixed axis along which K is projected.

The principal advantage of GCSA is that K becomes a good quantum number—thus, increasing the symmetry of the Hamiltonian. This means that the individual $K = K'$ diagonal blocks can be diagonalized separately. The problem size thus reduces by a factor of $n = (2J + 1)$. For $J > 3$, this provides a greater computational reduction for GCSA than for DGRA. Actually, there is some modest savings for $J = 3$ and $J = 2$ as well, for which not all of the $n = 8$ irreps are realized in the DGRA.

In every case—*i.e.*, for all J and every embedding—GCSA is at least as crude as DGRA, because it is equivalent to starting with the latter and (possibly) discarding additional contributions. This is true because of the fact that ε_{rot} is a good quantum number for DGRA, so that each $\tilde{H}^J$ block-diagonalizes by p and ε_{rot}—and because each K block also has well-defined p and ε_{rot} values.

4.4.2. Jacobi and Radau bond embeddings

As discussed, GCSA depends not only on the embedding, but also on the choice of the body-fixed projection axis, $\hat{c}$. For planar molecules better results are obtained when $\hat{a} = \hat{z}$ (Appendix B), which would preclude the choice $\hat{c} = \hat{z}$. In principle, any planar axis will do for $\hat{c}$—*i.e.*, it needs not necessarily align with $\hat{x}$ nor with $\hat{y}$ (nor with the primed axes, in the case of asymmetric embeddings).

That said, however, for all Jacobi and Radau bond embeddings, there is one very natural choice for $\hat{c}$. Consider that for all geometries all such embeddings give rise to one planar body-fixed axis for which $G_{\alpha\alpha}^R = G_{zz}^R$, and another for which the diagonal tensor element is different from G_{zz}^R. Clearly, $\hat{c}$ should be chosen to align with the *latter* planar axis, for then we have $A_a = A_b \neq A_c$ in the DGRA, which describes a symmetric rotor.

Put another way, consider that for any Jacobi or Radau bond embedding, the $\tilde{H}^J$ matrix representation (prior to symmetry adaptation) is *block-tridiagonal*, rather than block-pentadiagonal. This is because the block-pentadiagonal contributions only come from $\hat{J}_a^2$ and $\hat{J}_b^2$, and these contributions cancel when $G_{aa}^R = G_{bb}^R$—as is the case when the projection axis $\hat{c}$ is chosen as described above. So $\tilde{H}^J$ is block-tridiagonal. Furthermore, the off-diagonal (*i.e.*, $K' = K \pm 1$) blocks arise solely from the Coriolis and G_{xy}^R contributions. As a consequence, *DGRA is equivalent to GCSA for all Jacobi and Radau bond embeddings.*

In other words, for all such embeddings, DGRA is block-diagonal in K to begin with, and so GCSA is no different or worse—as has been confirmed numerically, as well as theoretically. This is quite striking when we consider that for *symmetric* Jacobi bond embeddings, DGRA itself is practically as good as CFA. Thus, *all three* approximations are essentially equal in this case, and so *there is no reason why GCSA—with its many computational advantages—should not be used in practice, if an approximate calculation with symmetric Jacobi coordinates is desired*. Indeed, this has been the custom for some time. In Appendix D, we provide an explicit expression for each $\tilde{H}^{JK}$ block of the GCSA, as represented in a Jacobi or Radau bond embedding.

4.4.3. Linear symmetric embeddings

What is not so clear yet is whether or not GCSA in the symmetric Jacobi embeddings outperforms GCSA in the linear symmetric

embeddings. To be sure, at the CFA and DGRA levels of approximation, the linear symmetric embeddings are far superior. However, dropping down to the GCSA level takes nothing further away in the symmetric Jacobi case, whereas in the linear symmetric case this must clearly make things far worse. The reason is that G_{aa}^R need not be similar to G_{bb}^R, so the discarded block-pentadiagonal contribution can be quite large. To our knowledge, this issue has never previously been considered, because GCSA has in the past only been applied to Jacobi and Radau bond embeddings, for which there are no block-pentadiagonal contributions—hence our use of the terminology "generalized CS."

The GCSA comparisons are relevant for the spectroscopy and dynamics communities because it is this approximation that will most likely be used in practice, owing to the fact that it provides the most substantial computational savings. For the largest, $J = 10$ value considered in this paper (which is still quite modest [62]), the $n = (2J + 1)$ reduction in basis size gives rise to a 441-fold reduction in computational effort. On the other hand, the comparative analysis for GCSA is rather involved and complicated. Consequently, since the main focus of this article is CFA, an extended comparative discussion of GCSA performance is reserved for the supplementary material, see its Sec. III and Tables S20–S23. Here, we simply comment that the best linear symmetric embedding GCSA outperforms the best Jacobi/Radau bond GCSA by about a factor of 2, in the sense of smaller rovibrational energy level errors.

5. CFA results across a range of molecular systems

In this section, we provide a comprehensive comparison of the performance of CFA, across a range of embeddings and for a variety of molecular systems, that serve as important benchmarks for the high-resolution spectroscopic community. The studied systems include: water ($H_2^{16}O$), a triatomic AB_2 molecule, already investigated to some extent in our previous paper; [45] the fully deuterated form of water, $D_2^{16}O$; the asymmetrically deuterated isotopologue of water ($HD^{16}O$), a triatomic ABC molecule; two inherently-different A_3 molecules, trihydrogen cation (H_3^+) and ozone ($^{16}O_3$); and ammonia ($^{14}NH_3$), a tetratomic molecule exhibiting a large-amplitude motion.

5.1. Overview and computational details

The rovibrational energy levels of the systems studied were computed using the GENIUSH protocol and code [12,15,16,63,64] across a wide range of embeddings and rotational and vibrational excitations. In GENIUSH, switching between different vibrational coordinates and coordinate embeddings is straightforward. In conjunction with the GENIUSH KEO, the following potential energy surfaces (PESs) were utilized for the particular systems: the BT2 PES [56] for $H_2^{16}O$ and its deuterated isotopologues; the GLH3P PES of Pavanello et al. [65] for H_3^+; the DLLJG PES [66] for $^{16}O_3$; and the PES of Yurchenko et al. [67] for $^{14}NH_3$. In what follows, we focus mostly on $J = 1$ and in some cases also $J = 5$ rotational excitations, in conjunction with the lowest few vibrational parent states.

For each system, both exact and CFA calculations of the rovibrational levels were performed. Note that the GENIUSH code is also very convenient for obtaining G_R and G_{VR} tensor elements, and was therefore used to generate the tensor data provided in this section and in Section 4.2 (the vibrational coordinates actually used by GENIUSH are not those of Section 2.2) For each molecule studied, tensor data is provided for a range of geometries, which always include the equilibrium structure (r_e) as the "reference" geometry, together with a set of distortions in different directions in the vibrational space.

Note that all triatomic systems but one considered here have "at least" C_{2v} (if not D_{3h}) point-group symmetry for their reference structure. Accordingly, for these systems, we can refer to any geometry in terms of the relative displacements from the reference geometry in the bend, symmetric stretch, and/or asymmetric stretch coordinates. The symmetric stretch and bend coordinates lead to "symmetrically distorted" C_{2v} geometries, the asymmetric stretch results in C_s structures. Any geometry is then given as a set of relative displacements from the reference, expressed as percentages. As to the only exception, $HD^{16}O$, which has an equilibrium structure of C_s point-group symmetry, we used the exact same geometries as for $H_2^{16}O$ (see Table S1 and S12). Using valence coordinates, the vibrational coordinate values are the same as for $H_2^{16}O$ at the different geometries due to the mass independence, while for Radau coordinates, they are different. To label the $HD^{16}O$ geometries we used the symmetry labels of $H_2^{16}O$.

For the triatomic molecules, numerical values for all non-zero G_R and G_{VR} tensor elements are provided for each geometry and embedding, as are FNGR norm values, in units of cm^{-1}. For the tetratomic ammonia molecule, partly due to their significantly larger number, G_R and G_{VR} tensor elements are not detailed; only the FNGR norm values are presented.

5.2. $H_2^{16}O$

5.2.1. G_R and G_{VR} tensor elements

For $H_2^{16}O$, the G_R and G_{VR} tensor elements have already been analyzed in some detail in our earlier paper [45] for the three linear embeddings, EE, VBE, and RBE. Whereas in principle any vibrational coordinate system can be used for any embedding, it is natural to use valence coordinates for VBE and Radau for RBE. For EE, we have sometimes used both coordinates, mainly to demonstrate explicitly the coordinate-(in) dependent properties. In any event, in this paper we extend the range of geometries considered previously, and also extend the analysis to new embeddings not studied in our previous paper [45].

Focusing first on extending the range of geometries, in Table 2 explicit G_{VR} and G_R tensor elements are provided for the selected three linear embeddings at eight different geometries (see also Table S1), including more extensive ($1.3r_e$) symmetric and asymmetric stretching excitations than in our earlier paper [45] (for an expanded version of Table 2 with more geometries, see Table S2 and S3). Looking at the C_{2v} geometries of Table 2, we find that *all* of the FNGR norms of RBE are zero. This implies zero CC across the entire two-dimensional space of symmetric distortions (*i.e.*, arbitrary bend and symmetric stretch displacements). This remarkable situation was first explained and described in our earlier paper [45], leading to the conclusion that RBE is the "best" choice of embedding. In contrast, the VBE norms are nonzero everywhere, even at the reference geometry; however, they are still quite small, around 0.03 cm^{-1}, across all C_{2v} geometries. In contrast, the EE norms increase rapidly from 0.1 to 1.1 cm^{-1} upon increasing the bending distortion from $1.1\theta_e$ to $1.3\theta_e$ (see Table S2), although over the entire one-dimensional, pure symmetric stretching distortion space, the EE norm remains zero (see Table 2).

As for the FEEs, we argued in Section 4.2.2 that these should perform better than EE; but which of the two FEEs is better, and how do they compare with RBE? The interesting result, evident from Table 2, is that *two of the three embeddings, RBE, and Radau FEE (RFEE), are identical*, while the valence FEE (VFEE) is very close to the other two. One can understand this as follows, based on the fact that EE already has an intrinsic 1D zero-CC subspace, in the symmetric stretch direction (see row 9 of Table 2). Adding an *additional* direction along which CC is designed to be zero, in the bend direction, thus extends the zero-CC subspace to the full 2D space of symmetric displacements. Note that in this context, it does not

matter whether the valence or the Radau bend coordinate is what is added; either way, one obtains zero CC for all C_{2v} geometries—which is also what we have for RBE. Evidence to support this claim is provided in Table 2: all $\mathbf{G}_R$ and $\mathbf{G}_{VR}$ tensor elements are the same for all three embeddings, across all C_{2v} geometries.

The equivalence of RBE and RFEE also extends to the C_s geometries (see Table 2), for which the FNGR norms are no longer zero. The FNGR norm of the VFEE, although looks the same as RFEE to the provided digits for smaller asymmetric stretch distortions, is slightly above that of RFEE for larger asymmetric stretch distortions. The difference between the RFEE and VFEE norms actually increase from 3–7×10^{-4} cm^{-1} to 0.03–0.07 cm^{-1}, when $1.1 r_e$ is increased to $1.3 r_e$ for C_s geometries. From this, it is very clear that VFEE and RFEE are not equivalent.

More generally, two different effects associated with asymmetric stretch displacements can be ascertained from the C_s data (treating the FEEs as equivalent to RBE in the discussion below). First, pure asymmetric stretching adversely affects RBE much more than EE—$e.g.$, a $1.1 r_e$ distortion results in FNGR of 0.7 and 0.2 cm^{-1}, respectively. This is intriguing, because it implies that the Sayvetz optimization in one direction essentially comes at a cost in another. On the other hand, moving away from the equilibrium geometry in a $second$ direction, by distorting the bend up to $1.5\theta_e$ increases the EE norm more than 20 times, up to 4.2 cm^{-1}, whereas the RBE norm actually $decreases$ slightly. This suggests that RBE should be much better suited to describe highly excited combination bands. Note that the VBE's FNGR norm values are only slightly larger than those of RBE for all C_s geometries; but since they are worse for symmetric displacements, this again suggests that RBE should perform better.

To really assess which embedding should work best overall, we have carried out a detailed statistical analysis over all 16 000 geometries that are actually used in the rovibrational computations carried out by the GENIUSH code. From this analysis we find the following. First, for around 60% of the points, RBE has smaller FNGR than EE. Second, the highest FNGR(RBE)/FNGR(EE) norm ratio is only around 7 (at the highest asymmetric stretching distortion with the reference θ_e), while its inverse goes up to around 1000 at high bending distortion geometries (excluding the C_{2v} geometries, where the inverse ratio would be infinity). Overall, RBE appears to be significantly better than EE, a numerical result of considerable importance to the spectroscopic community, as experimental investigation of highly excited states is becoming more and more common.

Table 2

Numerical values of the $\mathbf{G}_R$ and $\mathbf{G}_{VR}$ tensor elements of H$_2$^{16}O for the linear and flexible embeddings studied in this paper. Numbers, in cm^{-1}, are provided for the C_{2v} reference geometry, as well as several symmetrically and asymmetrically distorted geometries. The C_{2v} (x, y)/C_s (x, y) notations mean x % distortion in symmetric/asymmetric stretching and y % distortion in bending. FNGR is the Frobenius norm ($\|\mathbf{G}_R - \mathbf{g}_R^{-1}\|_F$) of the $(\mathbf{G}_R - \mathbf{g}_R^{-1})$ tensor.

Embedding	Symmetry	$\mathbf{G}_R$				FNGR	$\mathbf{G}_{VR}$		
		G_{xx}	G_{xy}	G_{yy}	G_{zz}		G_{1z}	G_{2z}	G_{3z}
Eckart	C_{2v} (Ref.)	54.80	0	29.18	19.04	0	0	0	0
Radau flx. Eckart	C_{2v} (Ref.)	54.80	0	29.18	19.04	0	0	0	0
valence bisector	C_{2v} (Ref.)	54.80	0	29.18	19.10	0.06	2.01	−2.01	0
Radau bisector	C_{2v} (Ref.)	54.80	0	29.18	19.04	0	0	0	0
Eckart	C_{2v} (10, 30)	120.19	0	17.56	16.45	1.13	8.22	−8.22	0
Radau flx. Eckart	C_{2v} (10, 30)	120.19	0	17.56	15.32	0	0	0	0
valence bisector	C_{2v} (10, 30)	120.19	0	17.56	15.34	0.03	1.32	−1.32	0
Radau bisector	C_{2v} (10, 30)	120.19	0	17.56	15.32	0	0	0	0
Eckart	C_{2v} (30, 0)	32.43	0	17.27	11.27	0	0	0	0
Radau flx. Eckart	C_{2v} (30, 0)	32.43	0	17.27	11.27	0	0	0	0
valence bisector	C_{2v} (30, 0)	32.43	0	17.27	11.30	0.04	1.55	−1.55	0
Radau bisector	C_{2v} (30, 0)	32.43	0	17.27	11.27	0	0	0	0
(valence) Eckart	C_{2v} (30, 30)	86.05	0	12.57	11.78	0.81	7.32	−7.32	0
(Radau) Eckart	C_{2v} (30, 30)	86.05	0	12.57	11.78	0.81	6.96	−6.96	0
valence flx. Eckart	C_{2v} (30, 30)	86.05	0	12.57	10.97	0	0	0	0
Radau flx. Eckart	C_{2v} (30, 30)	86.05	0	12.57	10.97	0	0	0	0
valence bisector	C_{2v} (30, 30)	86.05	0	12.57	10.99	0.02	1.11	−1.11	0
Radau bisector	C_{2v} (30, 30)	86.05	0	12.57	10.97	0	0	0	0
Eckart	C_s (10, 0)	56.50	−8.03	30.01	19.04	0.18	0.02	−0.02	3.60
valence flx. Eckart	C_s (10, 0)	56.50	−8.03	30.01	19.60	0.74	0.41	0.37	7.52
Radau flx. Eckart	C_s (10, 0)	56.50	−8.02	30.01	19.60	0.74	0	0	7.27
valence bisector	C_s (10, 0)	56.41	−8.17	30.11	19.69	0.83	2.24	−1.83	7.66
Radau bisector	C_s (10, 0)	56.50	−8.02	30.01	19.60	0.74	0	0	7.27
Eckart	C_s (10, 50)	518.14	−41.10	22.20	22.32	4.16	14.04	−16.98	1.02
valence flx. Eckart	C_s (10, 50)	520.81	−18.94	19.53	18.83	0.66	0.16	0.14	2.95
Radau flx. Eckart	C_s (10, 50)	520.81	−18.93	19.53	18.83	0.66	0	0	2.64
valence bisector	C_s (10, 50)	520.73	−20.05	19.62	18.92	0.75	0.91	−0.75	3.12
Radau bisector	C_s (10, 50)	520.81	−18.93	19.53	18.83	0.66	0	0	2.64
Eckart	C_s (30, 0)	72.44	−28.45	37.83	19.04	1.52	0.13	−0.24	11.67
valence flx. Eckart	C_s (30, 0)	72.44	−28.45	37.83	24.85	7.34	1.42	1.03	26.67
Radau flx. Eckart	C_s (30, 0)	72.54	−28.40	37.74	24.82	7.31	0	0	25.57
valence bisector	C_s (30, 0)	71.47	−29.02	38.81	25.21	7.70	2.88	−1.55	27.21
Radau bisector	C_s (30, 0)	72.54	−28.40	37.74	24.82	7.31	0	0	25.57
(valence) Eckart	C_s (30, 50)	631.94	−148.02	53.05	22.01	5.05	12.01	−20.37	3.76
(Radau) Eckart	C_s (30, 50)	631.94	−148.02	53.05	22.01	5.05	10.98	−19.70	3.20
valence flx. Eckart	C_s (30, 50)	660.63	−66.96	24.37	23.50	6.55	0.54	0.39	10.43
Radau flx. Eckart	C_s (30, 50)	660.71	−66.59	24.29	23.43	6.47	0	0	9.11
valence bisector	C_s (30, 50)	659.71	−71.19	25.29	24.36	7.41	1.17	−0.63	11.09
Radau bisector	C_s (30, 50)	660.71	−66.59	24.29	23.43	6.47	0	0	9.11

The claims made above, pertaining to the equivalence of embeddings, and also the vibrational-coordinate-invariance of $\mathbf{G}_R$ but not of $\mathbf{G}_{VR}$, have been confirmed by many explicit calculations, and they are quite evident from the data of Table 2. For example, in rows 13–14 and 34–35 we present explicit tensor elements in the EE, computed using both valence and Radau coordinates, for a "least special" C_{2v} and C_s geometry. The $\mathbf{G}_R$ tensor elements (and hence FNGR) are seen to be identical, but the G_{iz}^{VR} are not. Henceforth, we drop "(valence)" or "(Radau)" from the embedding label, if it is not relevant. Here, Table 2 reveals another interesting feature, i.e., that for generic C_s geometries all three G_{iz}^{VR} values are nonzero in valence coordinates, but for Radau coordinates only G_{3z}^{VR} is non-zero, corresponding to the coupling of the bending vibration and rotation along the z axis. This suggests that Radau coordinates are more natural, helping to explain the equivalence of the flexible Eckart embedding with RBE—which, in any event is also evident from Table 2.

Extending the analysis to new embeddings not studied in our previous paper [45], in Table 3 we list $\mathbf{G}_R$ and $\mathbf{G}_{VR}$ tensor elements for an expanded set of $H_2{}^{16}O$ embeddings studied in this paper, but for a restricted set of geometries—i.e., the reference geometry, plus two selected distorted geometries, one with C_{2v} and one with C_s point-group symmetry. From Table 3 it is very clear that Jacobi and Radau bond embeddings reflect exactly the predictions made in Sections 3.3.2 and 4.2.2. The s- and a-Jacobi and the Radau bond embedding errors are one to two orders of magnitude worse than those of the three linear embeddings, EE, VBE, and RBE. For the C_{2v} geometry, where the FNGR norm of RBE is zero, the value of the FNGR norms for these embeddings fall in the range of 6–43 cm^{-1}. For the C_s geometry, where the FNGR norm of RBE is 0.74 cm^{-1}, the FNGR norm values fall in the range of 10–35 cm^{-1}. Based on the norm values, the sJrE embedding seems to be the best of the lot with FNGR norms of 5.6 and 10.2 cm^{-1} for the distorted C_{2v} and C_s structures, respectively. This makes intuitive sense, given that the coordinates respect the symmetry of the molecule. However, the sJRE embedding seems to be the worst, with FNGR norm values going up to 43.1 and 35.1 cm^{-1} for the distorted C_{2v} and C_s structures, respectively.

The Jacobi bisector embeddings perform much better than all Jacobi and Radau bond embeddings. It is of interest to point out that sJBE seems to be *worse* than aJBE. A moment's reflection reveals the probable reason why—because the a-Jacobi bond angle is similar to the valence bond angle, and even more similar to the Radau bond angle. As a result, this choice performs surprisingly well, with the FNGR norm being around 0.01 cm^{-1} for the reference structure and the other C_{2v} structure. Even more surprisingly, for C_s geometries aJBE seems to be slightly better than RBE, with a FNGR norm of 0.61 cm^{-1}.

In the end, the true indicators of Coriolis coupling are the rovibrational energy levels computed in the Coriolis-free approximation; therefore, it might be insightful to compare how close the computed energy levels are using RBE and aJBE.

Table 3

Numerical values of the $\mathbf{G}_R$ and $\mathbf{G}_{VR}$ tensor elements of $H_2{}^{16}O$ for all of the embeddings studied. For more details, see the caption to Table 2.

Coord.	Embedding	Symmetry	G_{xx}	G_{xy}	G_{yy}	G_{zz}	FNGR	G_{1z}	G_{2z}	G_{3z}
			$\mathbf{G}_R$					**$\mathbf{G}_{VR}$**		
valence	bisector	C_{2v} (Ref.)	54.80	0	29.18	19.10	0.06	2.01	−2.01	0
valence	r_1	C_{2v} (Ref.)	45.20	−12.40	38.78	38.78	19.74	0	4.03	38.10
Radau	Eckart	C_{2v} (Ref.)	54.80	0	29.18	19.04	0	0	0	0
Radau	bisector	C_{2v} (Ref.)	54.80	0	29.18	19.04	0	0	0	0
Radau	r_1	C_{2v} (Ref.)	45.90	−12.20	38.08	38.08	19.04	0	0	36.27
s-Jacobi	bisector	C_{2v} (Ref.)	41.99	12.81	41.99	21.00	1.95	0	0	12.81
s-Jacobi	R	C_{2v} (Ref.)	54.80	0	29.18	54.80	35.76	0	0	−54.80
s-Jacobi	r	C_{2v} (Ref.)	54.80	0	29.18	29.18	10.14	0	0	29.18
a-Jacobi	bisector	C_{2v} (Ref.)	54.78	−0.72	29.20	19.05	0.01	0	0	0.66
a-Jacobi	R	C_{2v} (Ref.)	46.58	−11.96	37.41	37.41	18.36	0	0	35.63
a-Jacobi	r	C_{2v} (Ref.)	45.20	−12.40	38.78	38.78	19.74	0	0	36.94
Val	bisector	C_{2v} (10, 10)	58.72	0	21.21	15.63	0.05	1.71	−1.71	0
valence	r_1	C_{2v} (10, 10)	47.88	−17.01	32.05	32.05	16.47	0	3.43	29.79
Radau	Eckart	C_{2v} (10, 10)	58.72	0	21.21	15.71	0.12	2.73	−2.73	0
Radau	bisector	C_{2v} (10, 10)	58.72	0	21.21	15.58	0	0	0	0
Radau	r_1	C_{2v} (10, 10)	48.77	−16.56	31.16	31.16	15.58	0	0	27.52
s-Jacobi	bisector	C_{2v} (10, 10)	39.96	18.76	39.96	19.98	4.40	0	0	18.76
s-Jacobi	R	C_{2v} (10, 10)	58.72	0	21.21	58.72	43.14	0	0	−58.72
s-Jacobi	r	C_{2v} (10, 10)	58.72	0	21.21	21.21	5.63	0	0	21.21
a-Jacobi	bisector	C_{2v} (10, 10)	58.70	−0.98	21.23	15.59	0.01	0	0	0.77
a-Jacobi	R	C_{2v} (10, 10)	49.61	−16.09	30.32	30.32	14.74	0	0	26.78
a-Jacobi	r	C_{2v} (10, 10)	47.88	−17.01	32.05	32.05	16.47	0	0	28.31
valence	bisector	C_s (10, 0)	56.41	−8.17	30.11	19.69	0.83	2.24	−1.83	7.66
valence	r_1	C_s (10, 0)	54.47	−10.69	32.05	32.05	13.19	0	3.66	31.59
Radau	Eckart	C_s (10, 0)	56.50	−8.03	30.01	19.04	0.18	0.02	−0.02	3.60
Radau	bisector	C_s (10, 0)	56.50	−8.02	30.01	19.60	0.74	0	0	7.27
Radau	r_1	C_s (10, 0)	54.95	−10.15	31.57	31.57	12.71	0	0	30.05
s-Jacobi	bisector	C_s (10, 0)	52.10	12.72	34.42	20.73	1.87	0	0	12.19
s-Jacobi	R	C_s (10, 0)	53.90	11.25	32.62	53.90	35.05	0	0	−52.77
s-Jacobi	r	C_s (10, 0)	57.51	6.05	29.00	29.00	10.15	0	0	28.39
a-Jacobi	bisector	C_s (10, 0)	56.94	7.25	29.58	19.47	0.61	0	0	−6.53
a-Jacobi	R	C_s (10, 0)	40.71	−15.27	45.81	45.81	26.95	0	0	43.46
a-Jacobi	r	C_s (10, 0)	54.47	−10.69	32.05	32.05	13.19	0	0	30.41

5.2.2. Rovibrational energy levels

The rovibrational energies of $H_2{}^{16}O$ computed in the CFA have been studied in detail in our previous paper for three linear embeddings [45]. The $J = 1$ and 10 rovibrational levels were listed in Tables 2 and 3 of that paper, respectively, and the CFA errors of $\Delta(\hat{T}_{VR})$ were plotted in Figs. 3 and 4 of that paper, respectively [45]. Here, we extend our discussion to the Jacobi and Radau bond embeddings and the (symmetric- and asymmetric-) Jacobi bisector embeddings.

The numerical results for $J = 1$ are provided in Table 4. We only list the CFA errors of $\Delta(\hat{T}_{VR})$ for the different embeddings—*i.e.*, in Table 4 the CFA energy levels are compared to the eigenvalues obtained using the full operator for all the embeddings studied in this paper using valence, Radau, and symmetric and asymmetric Jacobi vibrational coordinates. The actual CFA eigenvalues can be found in Tables S4 and S5. Similarly, for $J = 2$ and 3, CFA energy levels are listed in Tables S6–S9 and their errors are provided there, as well. For linear symmetric embeddings, rovibrational energy levels with high J values are also presented in Table S10 and Table 3 of our previous paper [45] for $J = 5$ and 10, respectively. Vibrational (vib, $(v_1\ v_2\ v_3)$) labels are provided for each state, the rovibrational energies are relative to their vibrational parents. The computed eigenvalues closely follow the rigid-rotor model;

Table 4

$J = 1$ rovibrational energy levels of $H_2{}^{16}O$ using the exact Hamiltonian, $\hat{H}_{VR}$, and the differences of the eigenvalues, $\Delta(\hat{T}_{VR})$, obtained with the full and the Coriolis-free Hamiltonian, $\hat{H}_{VR} - \hat{T}_{VR}$. The results are presented in cm^{-1} using different coordinates for all the embeddings studied in this paper. The $\hat{H}_{VR}$ levels are given relative to the vibrational parent state. The vibrational (vib, $(v_1\ v_2\ v_3)$) and the rotational (rot, $J_{K_aK_c}$) quantum numbers are assigned for each state.

	$\hat{H}_{VR}$			$\Delta(\hat{T}_{VR})$											
				valence			Radau				a-Jacobi			s-Jacobi	
#	level	vib	rot	r_1	VBE	VFEE	r_1	RBE	EE	RFEE	r	R	aJBE	r	R	sJBE
1	23.8	(0 0 0)	1_{01}	9.76	0.07	0.03	9.40	0.03	0.01	0.03	9.76	9.06	0.03	4.97	18.57	1.26
2	37.1	(0 0 0)	1_{11}	9.60	0.05	0.03	9.27	0.03	0.01	0.03	9.60	8.96	0.03	5.23	17.83	1.11
3	42.4	(0 0 0)	1_{10}	0.00	0.00	0.00	0.00	0.00	0.00	0.00	0.00	0.00	0.00	0.00	0.00	0.00
4	23.8	(0 1 0)	1_{01}	9.84	0.16	0.12	9.47	0.12	0.22	0.12	9.84	9.11	0.12	5.26	21.95	2.26
5	40.2	(0 1 0)	1_{11}	9.63	0.14	0.12	9.29	0.12	0.21	0.12	9.63	8.97	0.12	5.54	20.99	2.05
6	45.8	(0 1 0)	1_{10}	0.00	0.00	0.00	0.00	0.00	0.00	0.00	0.00	0.00	0.00	0.00	0.00	0.00
7	23.8	(0 2 0)	1_{01}	9.84	0.24	0.20	9.45	0.20	0.43	0.20	9.84	9.08	0.21	5.52	26.48	3.54
8	44.5	(0 2 0)	1_{11}	9.74	0.22	0.21	9.39	0.21	0.41	0.21	9.74	9.06	0.21	5.82	25.15	3.23
9	50.3	(0 2 0)	1_{10}	0.00	0.00	0.00	0.00	0.00	0.00	0.00	0.00	0.00	0.00	0.00	0.00	0.00
10	23.4	(1 0 0)	1_{01}	9.57	0.07	0.03	9.23	0.03	0.01	0.03	9.57	8.90	0.03	4.92	18.03	1.21
11	36.2	(1 0 0)	1_{11}	9.42	0.05	0.03	9.10	0.03	0.01	0.03	9.42	8.80	0.03	5.20	17.28	1.05
12	41.4	(1 0 0)	1_{10}	0.00	0.00	0.00	0.00	0.00	0.00	0.00	0.00	0.00	0.00	0.00	0.00	0.00
13	23.6	(0 0 1)	1_{01}	9.54	0.06	−0.01	9.18	−0.01	−0.16	−0.01	9.54	8.83	−0.01	4.52	17.49	0.98
14	35.8	(0 0 1)	1_{11}	9.35	−0.01	−0.01	9.06	−0.01	−0.16	−0.01	9.35	8.78	−0.01	5.28	15.53	0.59
15	41.1	(0 0 1)	1_{10}	0.00	0.00	0.00	0.00	0.00	0.00	0.00	0.00	0.00	0.00	0.00	0.00	0.00
16	23.8	(0 3 0)	1_{01}	9.79	0.33	0.29	9.37	0.29	0.65	0.29	9.79	8.99	0.30	5.75	32.97	5.32
17	50.7	(0 3 0)	1_{11}	9.92	0.31	0.29	9.54	0.29	0.62	0.29	9.92	9.20	0.30	6.07	30.93	4.82
18	56.8	(0 3 0)	1_{10}	0.00	0.00	0.00	0.00	0.00	0.00	0.00	0.00	0.00	0.00	0.00	0.00	0.00
19	23.4	(1 1 0)	1_{01}	9.65	0.16	0.12	9.29	0.12	0.22	0.12	9.65	8.95	0.13	5.22	21.27	2.17
20	39.2	(1 1 0)	1_{11}	9.44	0.14	0.12	9.12	0.12	0.21	0.12	9.44	8.81	0.12	5.51	20.29	1.96
21	44.7	(1 1 0)	1_{10}	0.00	0.00	0.00	0.00	0.00	0.00	0.00	0.00	0.00	0.00	0.00	0.00	0.00
22	23.6	(0 1 1)	1_{01}	9.59	0.14	0.07	9.22	0.07	0.04	0.07	9.59	8.86	0.08	4.80	20.50	1.89
23	38.5	(0 1 1)	1_{11}	9.39	0.08	0.07	9.09	0.07	0.03	0.07	9.39	8.80	0.07	5.60	18.07	1.37
24	44.1	(0 1 1)	1_{10}	0.00	0.00	0.00	0.00	0.00	0.00	0.00	0.00	0.00	0.00	0.00	0.00	0.00
25	23.7	(0 4 0)	1_{01}	9.73	0.40	0.36	9.29	0.36	0.90	0.36	9.73	8.89	0.37	5.92	43.27	8.10
26	60.8	(0 4 0)	1_{11}	10.10	0.39	0.37	9.71	0.37	0.83	0.37	10.10	9.35	0.38	6.28	39.50	7.10
27	67.1	(0 4 0)	1_{10}	0.00	0.00	0.00	0.00	0.00	0.00	0.00	0.00	0.00	0.00	0.00	0.00	0.00
28	23.4	(1 2 0)	1_{01}	9.65	0.26	0.22	9.28	0.22	0.43	0.22	9.65	8.93	0.22	5.50	25.59	3.41
29	43.2	(1 2 0)	1_{11}	9.56	0.23	0.21	9.22	0.21	0.41	0.21	9.56	8.91	0.22	5.80	24.24	3.09
30	49.0	(1 2 0)	1_{10}	0.00	0.00	0.00	0.00	0.00	0.00	0.00	0.00	0.00	0.00	0.00	0.00	0.00
31	23.6	(0 2 1)	1_{01}	9.56	0.23	0.16	9.17	0.16	0.25	0.16	9.56	8.81	0.17	5.07	24.44	3.03
32	42.2	(0 2 1)	1_{11}	9.52	0.16	0.16	9.20	0.16	0.21	0.16	9.52	8.91	0.16	5.90	21.29	2.31
33	48.1	(0 2 1)	1_{10}	0.00	0.00	0.00	0.00	0.00	0.00	0.00	0.00	0.00	0.00	0.00	0.00	0.00
34	23.0	(2 0 0)	1_{01}	9.38	0.08	0.03	9.04	0.03	−0.02	0.03	9.38	8.72	0.03	4.78	17.40	1.10
35	35.3	(2 0 0)	1_{11}	9.21	0.03	0.02	8.91	0.02	−0.03	0.02	9.21	8.63	0.02	5.18	16.33	0.89
36	40.5	(2 0 0)	1_{10}	0.00	0.00	0.00	0.00	0.00	0.00	0.00	0.00	0.00	0.00	0.00	0.00	0.00
37	23.2	(1 0 1)	1_{01}	9.37	0.07	0.00	9.02	0.00	−0.16	0.00	9.37	8.68	0.00	4.46	17.00	0.93
38	34.9	(1 0 1)	1_{11}	9.17	−0.01	−0.01	8.89	−0.01	−0.16	−0.01	9.17	8.63	−0.01	5.24	14.99	0.53
39	40.2	(1 0 1)	1_{10}	0.00	0.00	0.00	0.00	0.00	0.00	0.00	0.00	0.00	0.00	0.00	0.00	0.00
40	23.3	(0 0 2)	1_{01}	9.31	0.04	−0.05	8.96	−0.05	−0.30	−0.05	9.31	8.61	−0.05	4.17	16.59	0.76
41	34.6	(0 0 2)	1_{11}	9.11	−0.05	−0.05	8.86	−0.05	−0.27	−0.05	9.11	8.60	−0.05	5.30	13.90	0.24
42	39.9	(0 0 2)	1_{10}	0.00	0.00	0.00	0.00	0.00	0.00	0.00	0.00	0.00	0.00	0.00	0.00	0.00
43	23.6	(0 5 0)	1_{01}	9.77	0.46	0.43	9.28	0.43	1.17	0.43	9.77	8.83	0.44	6.00	62.24	13.39
44	80.3	(0 5 0)	1_{11}	10.20	0.46	0.44	9.80	0.44	1.05	0.44	10.20	9.44	0.45	6.43	53.07	10.66
45	86.7	(0 5 0)	1_{10}	0.00	0.00	0.00	0.00	0.00	0.00	0.00	0.00	0.00	0.00	0.00	0.00	0.00
46	23.4	(1 3 0)	1_{01}	9.63	0.35	0.31	9.23	0.31	0.67	0.31	9.63	8.87	0.32	5.75	31.94	5.18
47	49.3	(1 3 0)	1_{11}	9.72	0.32	0.30	9.37	0.30	0.62	0.30	9.72	9.04	0.31	6.07	29.72	4.61
48	55.4	(1 3 0)	1_{10}	0.00	0.00	0.00	0.00	0.00	0.00	0.00	0.00	0.00	0.00	0.00	0.00	0.00
49	23.6	(0 3 1)	1_{01}	9.47	0.31	0.24	9.07	0.24	0.48	0.24	9.47	8.70	0.25	5.30	29.92	4.56
50	47.4	(0 3 1)	1_{11}	9.72	0.24	0.24	9.38	0.24	0.39	0.24	9.72	9.07	0.25	6.18	25.52	3.49
51	53.5	(0 3 1)	1_{10}	0.00	0.00	0.00	0.00	0.00	0.00	0.00	0.00	0.00	0.00	0.00	0.00	0.00

therefore, the well-established [68] and in these cases meaningful rigid-rotor rotational quantum numbers (rot, $J_{K_aK_c}$) are also provided in the tables. For $J = 1$ and 2, the rotational increment is small compared to the gaps between the vibrational states; thus, the eigenenergies of the rovibrational states belonging to different vibrational parent states do not overlap. For $J = 5$ and 10, the rotational and vibrational excitations are already in the same magnitude, which makes the labeling of the rovibrational states more difficult.

As seen in Table 4, numerical calculations on $H_2^{16}O$ bear out all of our predictions, made both here and in our previous paper [45]. Overall, all three linear embeddings in the CFA reproduce the reference numbers obtained with the full $\hat{H}_{VR}$ remarkably well. For the first 50 rovibrational states, the largest errors are around 1 cm^{-1} for $J = 1$, around 2 cm^{-1} for $J = 2$, and still less than 5 cm^{-1} for $J = 3$. For larger J values, all of the rovibrational states based on the fundamental vibrations are reasonably accurate, with the largest errors being 5 and 20 cm^{-1} for $J = 5$ and $J = 10$, respectively. For the ground state, (000), EE is clearly the best embedding. It should also be mentioned that EE does much better for symmetric stretch excitations, (100) and (200), than with other vibrational excitations. The reason for this is the zero subspace along this motion, as discussed above. Interestingly, EE has a single, sizable negative error for the asymmetric stretch state, (001)—around the same magnitude as the error of (010). Therefore, the (011) combination levels are very accurate, due to error cancellation. For all other states in Table 4, RBE yields smaller CFA errors than EE. For the bending excitations, the error in RBE is around half

that of EE, even for higher overtones. Curiously, RBE appears to do best for pure asymmetric stretch excitations—a fact that seems at odds with the behavior of FNGR as described above, which predicts RBE to be better than EE only if bending excitation are also included to some extent. RBE errors are always smaller than VBE errors, but the VBE errors usually follow the trends of RBE errors. When RBE is better than EE, VBE is also better. On a separate note, the reader cannot fail to notice that for $J = 1$—for every single v and for every embedding—the CFA predictions for the 1_{10} rovibrational energy are *exact*. Since this property holds even for the asymmetric embeddings, it cannot depend on permutation symmetry. It does, however, relate to parity, as explained in detail in Appendix B.

As discussed above, RBE and RFEE are equivalent, this is also visible from the CFA energy levels. However, it is interesting to compare the difference of the VFEE and RFEE Coriolis-free energy levels. For $J = 1$, their difference is smaller than 0.001 cm^{-1} for the first 42 energy levels, while for $J = 5$ the differences increase up to 0.01 cm^{-1} for the first 90 energy levels.

For the asymmetric embeddings—i.e., Vr$_1$E (equivalent to aJrE), Rr$_1$E, and aJRE—the $J = 1$ errors of the 1_{01} and 1_{11} states are around 10 cm^{-1} (note that the 1_{10} states are still exact, as discussed in Appendix B). For the symmetric embeddings, we find sJrE errors ranging from about 5–8 cm^{-1} over the relevant v and J range, whereas the sJRE errors range from about 18–50 cm^{-1}. The main reason for this is that in the CFA, sJrE results in prolate energy levels, whereas sJRE yields oblate energy levels; $H_2^{16}O$ is closer to a prolate symmetric top at its equilibrium geometry. For larger J values, the errors are larger (up to several hundred cm^{-1} by $J = 5$)

Table 5
Numerical values of the $\mathbf{G}_R$ and $\mathbf{G}_{VR}$ tensor elements of HD^{16}O for all of the embeddings studied in this paper. For more details on the notation, see caption to Table 2. The symmetry labels provided here are not true point-group-symmetry labels, but the labels used for $H_2^{16}O$ at the same geometries.

Coord.	Embedding	Symmetry	$\mathbf{G}_R$				FNGR	$\mathbf{G}_{VR}$		
			G_{xx}	G_{xy}	G_{yy}	G_{zz}		G_{1z}	G_{2z}	G_{3z}
valence	Eckart	C_{2v} (Ref.)	46.16	−1.81	18.37	13.09	0	0	0	0
valence	flx. Eckart	C_{2v} (Ref.)	35.41	−13.66	29.12	13.10	0.02	−0.06	−0.06	−0.93
valence	bisector	C_{2v} (Ref.)	42.64	−9.42	21.89	14.55	1.46	2.01	−2.01	8.83
valence	w. bisector	C_{2v} (Ref.)	35.41	−13.66	29.12	13.19	0.10	1.34	−2.68	−0.93
Radau	Eckart	C_{2v} (Ref.)	35.39	−13.66	29.14	13.09	0	0	0	0
Radau	flx. Eckart	C_{2v} (Ref.)	35.39	−13.66	29.14	13.11	0.02	0	0	−0.90
Radau	bisector	C_{2v} (Ref.)	42.88	−9.14	21.65	14.38	1.30	0	0	8.15
Radau	w. bisector	C_{2v} (Ref.)	35.39	−13.66	29.14	13.11	0.02	0	0	−0.90
valence	Eckart	C_{2v} (10, 0)	38.15	−1.49	15.18	10.82	0	0	0	0
valence	flx. Eckart	C_{2v} (10, 0)	29.26	−11.29	24.07	10.83	0.01	−0.06	−0.06	−0.77
valence	bisector	C_{2v} (10, 0)	35.24	−7.78	18.09	12.02	1.20	1.83	−1.83	7.29
valence	w. bisector	C_{2v} (10, 0)	29.26	−11.29	24.07	10.90	0.08	1.22	−2.44	−0.77
Radau	Eckart	C_{2v} (10, 0)	29.25	−11.29	24.08	10.82	0	0	0	0
Radau	flx. Eckart	C_{2v} (10, 0)	29.25	−11.29	24.08	10.83	0.01	0	0	−0.74
Radau	bisector	C_{2v} (10, 0)	35.44	−7.56	17.89	11.89	1.07	0	0	6.74
Radau	w. bisector	C_{2v} (10, 0)	29.25	−11.29	24.08	10.83	0.01	0	0	−0.74
valence	Eckart	C_{2v} (10, 10)	47.84	0.75	13.76	10.75	0.08	1.37	−2.54	−0.05
valence	flx. Eckart	C_{2v} (10, 10)	37.34	−15.75	24.26	10.69	0.02	−0.06	−0.06	−0.82
valence	bisector	C_{2v} (10, 10)	45.69	−8.31	15.91	11.86	1.18	1.71	−1.71	6.83
valence	w. bisector	C_{2v} (10, 10)	37.34	−15.75	24.26	10.75	0.07	1.14	−2.29	−0.82
Radau	Eckart	C_{2v} (10, 10)	37.41	−15.72	24.19	10.75	0.08	1.26	−2.43	−0.08
Radau	flx. Eckart	C_{2v} (10, 10)	37.32	−15.76	24.28	10.69	0.02	0	0	−0.76
Radau	bisector	C_{2v} (10, 10)	45.89	−7.95	15.71	11.70	1.03	0	0	6.04
Radau	w. bisector	C_{2v} (10, 10)	37.32	−15.76	24.28	10.69	0.02	0	0	−0.76
valence	Eckart	C_s (10, 0)	53.57	−6.48	16.87	12.33	0.10	0.16	0.16	2.49
valence	flx. Eckart	C_s (10, 0)	35.54	−19.46	34.91	12.51	0.28	0.28	0.26	4.16
valence	bisector	C_s (10, 0)	46.36	−15.96	24.08	15.93	3.69	2.24	−1.83	14.96
valence	w. bisector	C_s (10, 0)	35.26	−19.46	35.18	12.61	0.38	1.49	−2.44	4.31
Radau	Eckart	C_s (10, 0)	35.51	−19.46	34.93	12.33	0.10	0.05	−0.11	2.35
Radau	flx. Eckart	C_s (10, 0)	35.52	−19.46	34.92	12.51	0.28	0	0	3.91
Radau	bisector	C_s (10, 0)	47.04	−15.46	23.41	15.63	3.39	0	0	13.72
Radau	w. bisector	C_s (10, 0)	35.52	−19.46	34.92	12.51	0.28	0	0	3.91

and show more of a range across K_a and K_c—though remarkably, there is still very little variation across v or across embedding. In brief, the $\Delta(\hat{T}_{VR})$ errors of sJrE are always the smallest compared to the other Jacobi and Radau bond embeddings (about half those of the asymmetric embeddings), whereas the sJRE errors are always the largest (about twice those of the asymmetric embeddings), adhering to the predictions based on FNGR norms.

The performance of sJBE is most similar to that of sJrE. Although the $\Delta(\hat{T}_{VR})$ errors for sJBE (Table 4) start smaller than those of sJrE

(around 1.3 cm^{-1} for the zero-point vibration), they increase rapidly upon vibrational excitation. For the (040) bending overtone, they surpass sJrE with $\Delta(\hat{T}_{VR})$ of 8.2 cm^{-1}. However, aJBE performs significantly better than sJBE. For $J = 1$, the CFA energies seem to be very close to their RBE counterparts, with differences smaller than 0.01 cm^{-1} (not visible in Table 4). For higher J, the difference increases slightly. For $J = 5$, the difference between aJBE and RBE is up to 0.4 cm^{-1} for the zero-point vibration. This increases up to 5.0 cm^{-1} for the fundamentals.

Table 6

$J = 1$ rovibrational energy levels of HD^{16}O using the exact Hamiltonian, $\hat{H}_{VR}$, and the differences of the eigenvalues, $\Delta(\hat{T}_{VR})$, obtained with the full and the Coriolis-free Hamiltonian, $\hat{H}_{VR} - \hat{T}_{VR}$. The results are presented in cm^{-1} using valence and Radau coordinates with r_H, r_D, bisector, weighted-bisector, Eckart, and flexible-Eckart embeddings. The $\hat{H}_{VR}$ levels are given relative to the ZPVE (abs) as well as to the vibrational parent state. The vibrational (vib, $(v_1 v_2 v_3)$) and the rotational (rot, $J_{K_a K_c}$) quantum numbers are assigned for each state.

| | $\hat{H}_{VR}$ | | | | $\Delta(\hat{T}_{VR})$ | | | | | | | | | |
| | | | | | valence | | | | | Radau | | | | | |
#	abs	level	vib	rot	r_H	r_D	VBE	VwBE	VFEE	r_H	r_D	RBE	RwBE	EE	RFEE
1	15.5	15.5	(0 0 0)	1_{01}	12.94	3.61	0.79	0.06	0.02	12.24	3.40	0.70	0.02	0.01	0.02
2	29.8	29.8	(0 0 0)	1_{11}	12.16	3.79	0.65	0.07	0.03	11.52	3.59	0.57	0.03	0.01	0.03
3	32.5	32.5	(0 0 0)	1_{10}	0.00	0.00	0.00	0.00	0.00	0.00	0.00	0.00	0.00	0.00	0.00
4	1419.1	15.6	(0 1 0)	1_{01}	13.60	3.46	0.95	0.10	0.05	12.87	3.24	0.86	0.05	0.12	0.05
5	1435.3	31.8	(0 1 0)	1_{11}	11.46	4.04	0.56	0.13	0.10	10.82	3.83	0.50	0.10	0.12	0.10
6	1438.2	34.7	(0 1 0)	1_{10}	0.00	0.00	0.00	0.00	0.00	0.00	0.00	0.00	0.00	0.00	0.00
7	2739.1	15.2	(1 0 0)	1_{01}	13.13	3.44	0.87	0.08	0.02	12.42	3.24	0.77	0.02	0.01	0.02
8	2753.6	29.7	(1 0 0)	1_{11}	12.11	3.66	0.65	0.05	0.02	11.48	3.47	0.59	0.02	−0.02	0.02
9	2756.2	32.3	(1 0 0)	1_{10}	0.00	0.00	0.00	0.00	0.00	0.00	0.00	0.00	0.00	0.00	0.00
10	2797.5	15.6	(0 2 0)	1_{01}	14.17	3.29	1.09	0.11	0.07	13.39	3.08	1.00	0.07	0.19	0.07
11	2816.2	34.2	(0 2 0)	1_{11}	10.87	4.26	0.48	0.18	0.15	10.24	4.04	0.42	0.15	0.22	0.15
12	2819.2	37.3	(0 2 0)	1_{10}	0.00	0.00	0.00	0.00	0.00	0.00	0.00	0.00	0.00	0.00	0.00
13	3723.7	15.4	(0 0 1)	1_{01}	12.30	3.67	0.70	0.07	0.01	11.64	3.46	0.60	0.01	−0.05	0.01
14	3737.0	28.7	(0 0 1)	1_{11}	11.55	3.84	0.55	0.06	0.03	10.96	3.65	0.49	0.03	−0.04	0.03
15	3739.8	31.5	(0 0 1)	1_{10}	0.00	0.00	0.00	0.00	0.00	0.00	0.00	0.00	0.00	0.00	0.00
16	4115.2	15.4	(1 1 0)	1_{01}	14.38	3.28	1.22	0.19	0.15	13.57	3.07	1.11	0.15	0.29	0.15
17	4134.2	34.4	(1 1 0)	1_{11}	10.69	4.18	0.45	0.16	0.13	10.08	3.97	0.40	0.13	0.18	0.13
18	4137.3	37.5	(1 1 0)	1_{10}	0.00	0.00	0.00	0.00	0.00	0.00	0.00	0.00	0.00	0.00	0.00
19	4161.0	15.5	(0 3 0)	1_{01}	14.52	3.16	1.15	0.09	0.04	13.73	2.94	1.05	0.04	0.15	0.04
20	4180.5	35.0	(0 3 0)	1_{11}	10.63	4.24	0.43	0.16	0.14	10.01	4.02	0.37	0.14	0.22	0.14
21	4183.6	38.1	(0 3 0)	1_{10}	0.00	0.00	0.00	0.00	0.00	0.00	0.00	0.00	0.00	0.00	0.00
22	5105.8	15.5	(0 1 1)	1_{01}	12.92	3.52	0.86	0.10	0.04	12.22	3.31	0.76	0.05	0.06	0.05
23	5120.9	30.5	(0 1 1)	1_{11}	10.89	4.10	0.48	0.13	0.10	10.31	3.89	0.42	0.10	0.07	0.10
24	5123.9	33.5	(0 1 1)	1_{10}	0.00	0.00	0.00	0.00	0.00	0.00	0.00	0.00	0.00	0.00	0.00
25	5379.2	14.9	(2 0 0)	1_{01}	13.19	3.28	0.90	0.06	0.01	12.48	3.09	0.80	0.01	−0.04	0.01
26	5393.4	29.1	(2 0 0)	1_{11}	12.22	3.47	0.69	0.02	0.00	11.60	3.30	0.62	0.00	−0.07	0.00
27	5396.0	31.7	(2 0 0)	1_{10}	0.00	0.00	0.00	0.00	0.00	0.00	0.00	0.00	0.00	0.00	0.00
28	5435.0	15.6	(0 4 0)	1_{01}	15.06	3.08	1.44	0.23	0.19	14.19	2.85	1.34	0.19	0.47	0.19
29	5461.0	41.7	(0 4 0)	1_{11}	9.98	4.69	0.34	0.29	0.27	9.35	4.45	0.29	0.27	0.42	0.27
30	5464.5	45.1	(0 4 0)	1_{10}	0.00	0.00	0.00	0.00	0.00	0.00	0.00	0.00	0.00	0.00	0.00
31	5521.7	15.4	(1 2 0)	1_{01}	14.61	3.05	1.19	0.08	0.03	13.81	2.83	1.08	0.03	0.15	0.03
32	5541.6	35.3	(1 2 0)	1_{11}	10.50	4.21	0.41	0.16	0.13	9.89	4.00	0.36	0.13	0.21	0.13
33	5544.7	38.4	(1 2 0)	1_{10}	0.00	0.00	0.00	0.00	0.00	0.00	0.00	0.00	0.00	0.00	0.00
34	6431.6	15.2	(1 0 1)	1_{01}	12.70	3.49	0.83	0.10	0.04	12.01	3.29	0.73	0.04	0.00	0.04
35	6445.5	29.2	(1 0 1)	1_{11}	11.24	3.79	0.52	0.06	0.03	10.67	3.60	0.47	0.03	−0.05	0.03
36	6448.3	31.9	(1 0 1)	1_{10}	0.00	0.00	0.00	0.00	0.00	0.00	0.00	0.00	0.00	0.00	0.00
37	6468.2	15.5	(0 2 1)	1_{01}	13.41	3.36	0.96	0.10	0.04	12.68	3.15	0.86	0.04	0.09	0.04
38	6484.9	32.1	(0 2 1)	1_{11}	10.45	4.23	0.42	0.17	0.14	9.88	4.03	0.37	0.14	0.14	0.14
39	6488.0	35.2	(0 2 1)	1_{10}	0.00	0.00	0.00	0.00	0.00	0.00	0.00	0.00	0.00	0.00	0.00
40	6705.0	15.6	(0 5 0)	1_{01}	15.39	2.95	1.60	0.26	0.22	14.45	2.71	1.49	0.22	0.61	0.22
41	6739.2	49.8	(0 5 0)	1_{11}	9.56	4.92	0.24	0.35	0.32	8.92	4.67	0.20	0.32	0.54	0.32
42	6742.8	53.3	(0 5 0)	1_{10}	0.00	0.00	0.00	0.00	0.00	0.00	0.00	0.00	0.00	0.00	0.00
43	6762.2	15.0	(2 1 0)	1_{01}	14.44	3.14	1.22	0.16	0.10	13.63	2.94	1.10	0.10	0.15	0.10
44	6779.5	32.3	(2 1 0)	1_{11}	11.02	3.84	0.50	0.09	0.07	10.43	3.65	0.45	0.07	0.07	0.07
45	6782.4	35.2	(2 1 0)	1_{10}	0.00	0.00	0.00	0.00	0.00	0.00	0.00	0.00	0.00	0.00	0.00
46	6864.5	15.5	(1 3 0)	1_{01}	14.93	2.89	1.28	0.08	0.02	14.11	2.67	1.17	0.02	0.18	0.02
47	6886.7	37.7	(1 3 0)	1_{11}	10.14	4.34	0.33	0.18	0.16	9.53	4.12	0.29	0.16	0.27	0.16
48	6889.9	40.8	(1 3 0)	1_{10}	0.00	0.00	0.00	0.00	0.00	0.00	0.00	0.00	0.00	0.00	0.00
49	7267.4	15.3	(0 0 2)	1_{01}	11.67	3.74	0.61	0.08	0.01	11.05	3.53	0.51	0.01	−0.11	0.01
50	7279.7	27.6	(0 0 2)	1_{11}	10.95	3.90	0.46	0.06	0.03	10.42	3.71	0.41	0.03	−0.10	0.03
51	7282.5	30.4	(0 0 2)	1_{10}	0.00	0.00	0.00	0.00	0.00	0.00	0.00	0.00	0.00	0.00	0.00

To help ensure that conclusions drawn for $H_2{}^{16}O$ are not merely anecdotal, but in fact reflective of all C_{2v} AB$_2$ systems (with a heavy A atom), we have repeated the above study for the doubly-deuterated isotopologue, $D_2{}^{16}O$. The resultant CFA energy levels show a very similar pattern to $H_2{}^{16}O$ (see Fig. S1), with the main difference being that the $\Delta(\hat{T}_{VR})$ errors are found to be around half of those of $H_2{}^{16}O$, due to the D/H substitution (see Table S11 and Fig. S1).

5.3. HD^{16}O

More interesting than $D_2{}^{16}O$ is the singly deuterated isotopologue of water, HD^{16}O. Here, due to the H/D mass disparity, the system becomes substantially asymmetric—although the PES still reflects the symmetry of $H_2{}^{16}O$, as mass dependence is not introduced into the BT2 PES, for example *via* the diagonal Born–Oppenheimer approximation. In any event, as an asymmetric ABC molecule, HD^{16}O serves as an important generalization of the case of $H_2{}^{16}O$, which will demonstrate which aspects of AB$_2$ theory can be generalized for the ABC context, and also how this can be achieved.

With the increasing number of embeddings due to the asymmetry of the system, we only performed computations using valence and Radau coordinates. As a consequence of the asymmetric deuteration, all the symmetric C_{2v} properties of the KEO are lost for this isotopologue. The G_{xy}^R tensor element is thus non-zero for all embeddings and geometries (see Table 5), and the G_{3z}^{VR} elements are also non-zero in almost all cases.

As to CC, the situation is quite different compared to $H_2{}^{16}O$, due to the loss of two symmetry elements. Most dramatically, the FNGR norm of RBE is now non-zero everywhere, with substantial FNGR norm values even for C_{2v} geometries (see Table 5, but note that the symmetry labels provided there are not true point-group symmetry labels but the ones used for $H_2{}^{16}O$ at the same geometries). For EE, FNGR is still zero at the reference geometry and under symmetric stretch displacements. In general, however, the FNGR norm values of EE are even smaller for HD^{16}O than for $H_2{}^{16}O$, for both C_{2v} and C_s geometries, which probably reflects the heavier mass. They are, in any case, much smaller than for RBE, *i.e.*, something like 0.1 cm^{-1} vs. 3 cm^{-1}. It is also clear that the bond embeddings remain worse than the linear embeddings, with the (valence and Radau) r_H embeddings significantly worse than the r_D embeddings (*i.e.*, FNGR values of around 20 cm^{-1} vs. 5 cm^{-1}).

For HD^{16}O, similar to $H_2{}^{16}O$, we only provide the CFA errors (Table 6), the CFA rovibrational energy levels themselves can be found in Tables S13 and S14 of the supplementary material. Looking at the rovibrational energy level errors for $J = 1$ (see Table 6 and Fig. 5), one can notice that, as predicted, EE performs much better than RBE. For the first 35 states, the EE errors are smaller than 0.3 cm^{-1}, while the RBE errors are increasing up to 1.1 cm^{-1}. VBE follows RBE, with around 0.1 cm^{-1} differences. Of course, given the asymmetric masses of the two side atoms the opportunity arises naturally to question whether the *bisector* of the bond angle is still the appropriate reference to compare EE with. Would not a *mass-weighted* partitioning of the angle, with the narrower wedge closer to the D atom, be a more appropriate generalization of the AB$_2$ "bisector" embeddings for ABC molecules?

Such considerations give rise to two new embeddings, *i.e.*, mass-weighted versions of the valence and Radau bisector embeddings, referred to as "VwBE" and "RwBE", respectively. Indeed, these choices give rise to FNGR norm values for C_{2v} geometries which are quite small for VwBE (about 0.1 cm^{-1}), and *practically zero* for RwBE (about 0.02 cm^{-1}). Moreover, it is clear from Table 5

that RwBE is *identical* to RFEE, lending further credence to the notion that this is the proper generalization of the AB$_2$ RBE for ABC molecules, which perhaps holds even for larger molecular systems. (The equivalence or near-equivalence with VFEE also appears likely, but can no longer be proved using symmetry arguments.) In any event, FNGR norm values of RwBE are generally smaller than their EE counterparts, except for pure asymmetric stretch displacements.

The CFA rovibrational energy levels computed using the mass-weighted bisector embeddings [(V/R)wBE] confirm all of our earlier predictions. First, the CFA errors are much smaller for (V/R) wBE than for the corresponding (V/R)BE calculation (compare Fig. 5 and Fig. 6). Second, the RwBE errors are mostly smaller than those of EE (see Fig. 6 and Table 6); moreover, their correlation is similar to the correlation of the RBE and EE calculations for $H_2{}^{16}O$. Third, VwBE produces $\Delta(\hat{T}_{VR})$ errors slightly larger than RwBE. Finally, we also investigated the FEEs. Here—and similarly to the relation found for $H_2{}^{16}O$—we find that RwBE, RFEE, and VFEE all yield identical CFA rovibrational eigenvalues, further supporting the idea that these are in fact identical embeddings (see Tables 5 and 6).
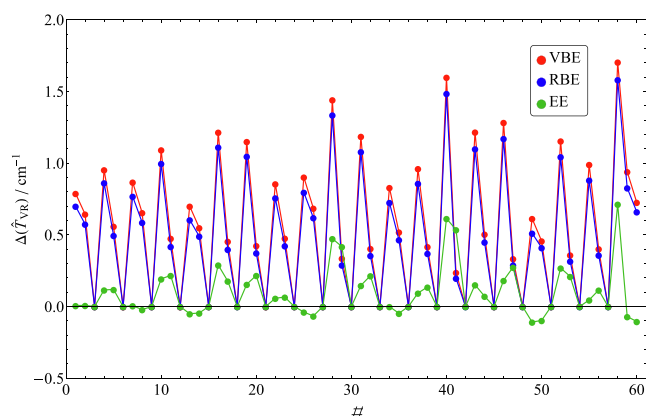
Fig. 5. The differences, $\Delta(\hat{T}_{VR})$, of the $J = 1$ rovibrational energy levels of HD^{16}O using the exact Hamiltonian, $\hat{H}_{VR}$, and the Coriolis-free Hamiltonian, $\hat{H}_{VR} - \hat{T}_{VR}$. The results are presented using valence bisector (VBE), Radau bisector (RBE), and Eckart (EE) embeddings.
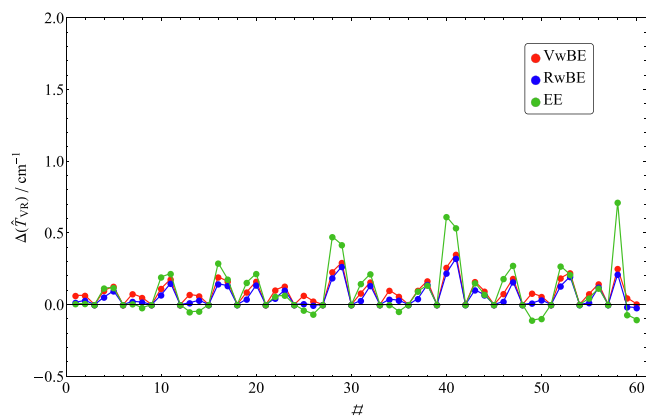
Fig. 6. The differences, $\Delta(\hat{T}_{VR})$, of the $J = 1$ rovibrational energy levels of HD^{16}O using the exact Hamiltonian, $\hat{H}_{VR}$, and the Coriolis-free Hamiltonian, $\hat{H}_{VR} - \hat{T}_{VR}$. The results are presented using valence weighted-bisector (VwBE), Radau weighted-bisector (RwBE), and Eckart (EE) embeddings.

5.4. H_3^+

The next system we investigate is the H_3^+ molecular cation, the smallest triatomic molecular system of considerable spectroscopic and atmospheric interest [65,69]. H_3^+ has higher symmetry than $H_2{}^{16}O$, in its ground electronic state it has an equilibrium structure of D_{3h} point-group symmetry. The lack of a heavy central atom indicates stronger CC, and a greater difference between valence and Radau coordinates (and embeddings) than for $H_2{}^{16}O$.

By examining $\mathbf{G}_R$ and $\mathbf{G}_{VR}$ tensor elements (see Table 7), it becomes clear from the FNGR norm values, $\|\mathbf{G}_R - \mathbf{g}_R^{-1}\|_F$, that the CC in H_3^+ is indeed significantly larger than in $H_2{}^{16}O$. For Jacobi and Radau bond embeddings, these values are around 44 cm^{-1} at the equilibrium geometry, which is more than double the corresponding $H_2{}^{16}O$ values (about 20 cm^{-1}). For VBE, we have 11 cm^{-1}, whereas it is 0.06 cm^{-1} for $H_2{}^{16}O$. Since these kind of numbers (or worse) also characterize the other geometries, none of these is a particularly appealing choice of embedding for the H_3^+ system.

For EE, FNGR norm is naturally zero at the equilibrium geometry of H_3^+, and remains zero for all D_{3h} geometries along v_1, the vibrational band origin (VBO) associated with the "breathing" motion (in exact analogy with symmetric stretching for $H_2{}^{16}O$). Likewise, RBE enjoys zero FNGR values over the entire 2D space of symmetric distortions (i.e., for all D_{3h} and C_{2v} geometries). For EE, the FNGR norm for C_{2v} geometries is tiny (around 0.1 cm^{-1}), which is comparable to the values for $H_2{}^{16}O$. The EE norm values are also quite small for C_s geometries ($\approx$0.6 cm^{-1}), suggesting that EE ought to be a good embedding choice. RBE values for C_s geometries are also quite small ($\approx$2.4 cm^{-1}), although substantially larger than for EE. Note that they are also *much* smaller than for VBE, underscoring how much more different these embeddings are for H_3^+ compared to $H_2{}^{16}O$. In any case, we expect the CFA errors to be considerably worse for H_3^+ than for $H_2{}^{16}O$, no matter which embedding is used.

The computed $J = 1$ Coriolis-free rovibrational energy levels displayed in Table 8 verify our predictions. Since the Jacobi and Radau bond embeddings perform a lot worse than the linear

Table 7

Numerical values of the $\mathbf{G}_R$ and $\mathbf{G}_{VR}$ tensor elements of H_3^+ for all of the embeddings studied in this paper. The numbers are provided in cm^{-1} in the D_{3h} reference geometry and symmetrically and asymmetrically distorted geometries with D_{3h}, C_{2v} and C_s point-group symmetry. For more details on the notation, see the caption to Table 2.

| Coord.	Embedding	Symmetry	$\mathbf{G}_R$				FNGR	$\mathbf{G}_{VR}$		
			G_{xx}	G_{xy}	G_{yy}	G_{zz}		G_{1z}	G_{2z}	G_{3z}
valence	Eckart	D_{3h} (Ref.)	87.77	0	87.77	43.89	0	0	0	0
valence	bisector	D_{3h} (Ref.)	87.77	0	87.77	54.86	10.97	−31.36	31.36	0
valence	r_1	D_{3h} (Ref.)	87.77	0	87.77	87.77	43.89	0	62.72	57.01
Radau	Eckart	D_{3h} (Ref.)	87.77	0	87.77	43.89	0	0	0	0
Radau	bisector	D_{3h} (Ref.)	87.77	0	87.77	43.89	0	0	0	0
Radau	r_1	D_{3h} (Ref.)	87.77	0	87.77	87.77	43.89	0	0	87.77
Jacobi	Eckart	D_{3h} (Ref.)	87.77	0	87.77	43.89	0	0	0	0
Jacobi	bisector	D_{3h} (Ref.)	87.77	0	87.77	43.89	0	0	0	0
Jacobi	R	D_{3h} (Ref.)	87.77	0	87.77	87.77	43.89	0	0	−87.77
Jacobi	r	D_{3h} (Ref.)	87.77	0	87.77	87.77	43.89	0	0	87.77
valence	Eckart	D_{3h} (10, 0)	72.54	0	72.54	36.27	0	0	0	0
valence	bisector	D_{3h} (10, 0)	72.54	0	72.54	45.34	9.07	−28.51	28.51	0
valence	r_1	D_{3h} (10, 0)	72.54	0	72.54	72.54	36.27	0	57.02	47.12
Radau	Eckart	D_{3h} (10, 0)	72.54	0	72.54	36.27	0	0	0	0
Radau	bisector	D_{3h} (10, 0)	72.54	0	72.54	36.27	0	0	0	0
Radau	r_1	D_{3h} (10, 0)	72.54	0	72.54	72.54	36.27	0	0	72.54
Jacobi	Eckart	D_{3h} (10, 0)	72.54	0	72.54	36.27	0	0	0	0
Jacobi	bisector	D_{3h} (10, 0)	72.54	0	72.54	36.27	0	0	0	0
Jacobi	R	D_{3h} (10, 0)	72.54	0	72.54	72.54	36.27	0	0	−72.54
Jacobi	r	D_{3h} (10, 0)	72.54	0	72.54	72.54	36.27	0	0	72.54
valence	Eckart	C_{2v} (10, 10)	77.35	0	61.14	34.26	0.12	−3.35	3.35	0
valence	bisector	C_{2v} (10, 10)	77.35	0	61.14	43.65	9.50	−30.08	30.08	0
valence	r_1	C_{2v} (10, 10)	65.95	−7.41	72.54	72.54	38.39	0	60.15	52.79
Radau	Eckart	C_{2v} (10, 10)	77.35	0	61.14	34.26	0.12	−2.65	2.65	0
Radau	bisector	C_{2v} (10, 10)	77.35	0	61.14	34.15	0	0	0	0
Radau	r_1	C_{2v} (10, 10)	70.19	−8.05	68.29	68.29	34.15	0	0	67.82
Jacobi	Eckart	C_{2v} (10, 10)	77.35	0	61.14	34.26	0.12	−3.35	2.74	1.99
Jacobi	bisector	C_{2v} (10, 10)	76.27	−4.03	62.21	34.26	0.12	0	0	3.99
Jacobi	R	C_{2v} (10, 10)	64.52	−6.59	73.97	64.52	30.37	0	0	−64.18
Jacobi	r	C_{2v} (10, 10)	65.95	−7.41	72.54	72.54	38.39	0	0	72.16
valence	Eckart	C_s (10, 0)	92.24	20.68	89.85	43.74	0.57	−4.17	−4.17	−7.65
valence	bisector	C_s (10, 0)	89.85	20.68	92.24	56.31	13.14	−34.85	28.51	−15.51
valence	r_1	C_s (10, 0)	109.56	−9.31	72.54	72.54	29.37	0	57.02	43.63
Radau	Eckart	C_s (10, 0)	92.24	20.68	89.85	43.74	0.57	−0.30	0.38	−10.20
Radau	bisector	C_s (10, 0)	92.27	20.68	89.82	45.52	2.35	0	0	−20.68
Radau	r_1	C_s (10, 0)	111.74	−0.95	70.35	70.35	27.19	0	0	70.35
Jacobi	Eckart	C_s (10, 0)	92.24	20.68	89.85	43.74	0.57	−4.17	4.38	−8.34
Jacobi	bisector	C_s (10, 0)	102.63	17.17	79.46	44.79	1.62	0	0	−16.90
Jacobi	R	C_s (10, 0)	106.61	−13.68	75.49	106.61	63.44	0	0	−105.74
Jacobi	r	C_s (10, 0)	109.56	−9.31	72.54	72.54	29.37	0	0	71.95

embeddings, we focus our attention on the latter group. According to the $\Delta(\hat{T}_{VR})$ errors (see Fig. 7), the energy levels can be sorted into two different groups. First, some of the levels, all belonging to singly degenerate vibrations, have small $\Delta(\hat{T}_{VR})$ errors. The zero-point vibration, the "breathing" fundamental and its overtone belong to this group. These states have errors less than 0.1 cm^{-1} for EE, and less than 0.5 cm^{-1} for RBE and the Jacobi bisector embedding (JBE). Note that only the two rovibrational states with the $J_G = 1_1$ rotational designation [70] have nonzero errors; the states with

$J_G = 1_0$ remain the same upon neglecting $\hat{T}_{VR}$. The pure bending states with $L_2 = 0$ quantum number [70] also belong to the first group. For EE, the $\Delta(\hat{T}_{VR})$ errors are 0.6 cm^{-1} and 0.7 cm^{-1} for the (020) and (040) states, respectively. They increase up to a couple of cm^{-1} for RBE and JBE. Second, the rest of the vibrational levels including all the doubly degenerate vibrational states have significantly larger errors, up to ±40 cm^{-1}. Note that two of the six $J = 1$ rovibrational levels of the doubly degenerate vibrational states always remain unchanged in the CFA with 0 cm^{-1} error;

Table 8
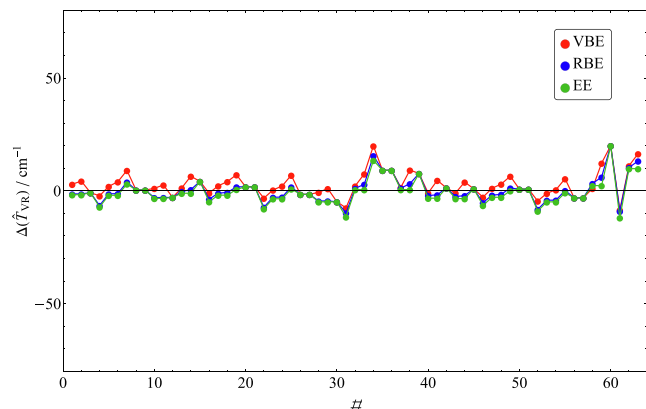
$J = 1$ rovibrational energy levels of H$_3^+$ using the exact Hamiltonian, $\hat{H}_{VR}$, and the differences of the eigenvalues, $\Delta(\hat{T}_{VR})$, obtained with the full and the Coriolis-free Hamiltonian, $\hat{H}_{VR} - \hat{T}_{VR}$. The results are presented in cm^{-1} using valence and Radau coordinates with r_1, bisector, and Eckart embeddings and with Jacobi coordinates with r, R, bisector, and Eckart embeddings. The $\hat{H}_{VR}$ levels are given relative to the ZPVE (abs) as well as to the vibrational parent state. The vibrational (vib, $(v_1 v_2 L_2)$) and the rotational (rot, J_G) quantum numbers are assigned for each state.

		$\hat{H}_{VR}$				valence			Radau			Jacobi		
#	abs	level	vib	rot	r_1	VBE	EE	r_1	RBE	EE	r	R	JBE	EE
1	64.1	64.1	(0 0 0)	1_1	19.83	4.63	0.00	19.88	0.33	0.00	19.83	19.93	0.33	0.00
2	64.1	64.1	(0 0 0)	1_1	22.81	6.05	0.00	22.82	0.36	0.00	22.81	22.82	0.36	0.00
3	87.0	87.0	(0 0 0)	1_0	0.00	0.00	0.00	0.00	0.00	0.00	0.00	0.00	0.00	0.00
4	2548.4	26.8	(0 1 1)	1_2	51.38	36.88	31.94	49.14	32.59	31.94	51.38	47.94	32.59	31.94
5	2548.4	26.8	(0 1 1)	1_2	54.73	41.07	37.12	58.10	37.74	37.12	54.73	60.94	37.55	37.12
6	2609.7	88.1	(0 1 1)	1_1	0.00	0.00	0.00	0.00	0.00	0.00	0.00	0.00	0.00	0.00
7	2609.7	88.1	(0 1 1)	1_1	0.00	0.00	0.00	0.00	0.00	0.00	0.00	0.00	0.00	0.00
8	2616.9	95.3	(0 1 1)	1_0	−5.72	−25.41	−31.40	−6.61	−30.66	−31.40	−5.72	−7.08	−30.47	−31.40
9	2627.5	106.0	(0 1 1)	1_0	−15.73	−31.04	−37.04	−15.19	−36.21	−37.04	−15.73	−15.56	−36.21	−37.04
10	3241.2	62.5	(1 0 0)	1_1	19.18	4.45	0.01	19.26	0.35	0.01	19.18	19.33	0.35	0.01
11	3241.2	62.5	(1 0 0)	1_1	22.36	5.95	0.01	22.36	0.39	0.01	22.36	22.36	0.39	0.01
12	3263.5	84.9	(1 0 0)	1_0	0.00	0.00	0.00	0.00	0.00	0.00	0.00	0.00	0.00	0.00
13	4842.9	64.2	(0 2 0)	1_1	15.01	2.91	0.56	16.20	1.34	0.56	15.01	17.51	1.38	0.56
14	4842.9	64.2	(0 2 0)	1_1	27.42	8.13	0.56	27.58	2.16	0.56	27.42	27.70	2.15	0.56
15	4870.6	92.0	(0 2 0)	1_0	0.00	0.00	0.00	0.00	0.00	0.00	0.00	0.00	0.00	0.00
16	4995.2	−3.2	(0 2 2)	1_3	81.40	68.07	64.25	80.99	65.35	64.25	81.40	80.69	65.36	64.25
17	4999.3	0.8	(0 2 2)	1_3	79.48	67.22	63.09	81.69	63.96	63.09	79.48	84.43	63.87	63.09
18	5088.0	89.6	(0 2 2)	1_2	0.00	0.00	0.00	0.00	0.00	0.00	0.00	0.00	0.00	0.00
19	5088.0	89.6	(0 2 2)	1_2	0.00	0.00	0.00	0.00	0.00	0.00	0.00	0.00	0.00	0.00
20	5125.7	127.3	(0 2 2)	1_1	−37.50	−57.31	−63.32	−37.59	−62.10	−63.32	−37.50	−37.66	−62.04	−63.32
21	5125.7	127.3	(0 2 2)	1_1	−37.28	−54.26	−60.76	−37.18	−59.65	−60.76	−37.28	−37.57	−59.59	−60.76
22	5584.8	30.0	(1 1 1)	1_2	46.84	32.64	27.93	44.42	28.60	27.93	46.84	43.24	28.60	27.93
23	5584.8	30.0	(1 1 1)	1_2	49.09	36.27	32.36	52.71	33.03	32.36	49.09	55.92	32.83	32.36
24	5641.1	86.2	(1 1 1)	1_1	0.00	0.00	0.00	0.00	0.00	0.00	0.00	0.00	0.00	0.00
25	5641.1	86.2	(1 1 1)	1_1	0.00	0.00	0.00	0.00	0.00	0.00	0.00	0.00	0.00	0.00
26	5645.3	90.5	(1 1 1)	1_0	−3.00	−22.50	−28.14	−3.81	−27.40	−28.14	−3.00	−4.22	−27.19	−28.14
27	5655.0	100.1	(1 1 1)	1_0	−12.30	−27.36	−33.46	−11.90	−32.57	−33.46	−12.30	−12.69	−32.58	−33.46
28	6323.8	60.9	(2 0 0)	1_1	18.51	4.26	0.02	18.62	0.38	0.02	18.51	18.74	0.38	0.02
29	6323.8	60.9	(2 0 0)	1_1	21.98	5.89	0.02	21.98	0.45	0.02	21.98	21.98	0.45	0.02
30	6345.8	82.9	(2 0 0)	1_0	0.00	0.00	0.00	0.00	0.00	0.00	0.00	0.00	0.00	0.00
31	7047.4	40.7	(0 3 1)	1_2	30.03	17.63	13.62	27.00	15.38	13.62	30.03	25.51	15.41	13.62
32	7047.4	40.7	(0 3 1)	1_2	37.34	27.31	25.71	45.46	26.26	25.71	37.34	54.71	26.05	25.71
33	7083.6	76.9	(0 3 1)	1_0	19.98	−3.56	−10.53	19.98	−8.16	−10.53	21.99	20.11	−7.76	−10.53
34	7103.6	96.9	(0 3 1)	1_1	0.00	0.00	0.00	0.00	0.00	0.00	0.00	0.00	0.00	0.00
35	7103.6	96.9	(0 3 1)	1_1	2.01	0.00	0.00	0.62	0.00	0.00	0.00	0.00	0.00	0.00
36	7110.7	104.0	(0 3 1)	1_0	−3.75	−18.25	−24.67	−1.98	−22.59	−24.67	−3.75	−2.89	−22.56	−24.67
37	7326.0	39.7	(0 3 3)	1_4	37.85	27.66	26.72	40.61	27.36	26.72	37.85	44.57	27.53	26.72
38	7326.0	39.7	(0 3 3)	1_4	56.01	35.38	26.72	56.11	29.33	26.72	55.80	55.80	29.34	26.72
39	7381.8	95.5	(0 3 3)	1_3	0.00	0.00	0.00	0.00	0.00	0.00	0.20	0.00	0.00	0.00
40	7572.7	79.1	(0 3 3)	1_2	−2.11	−14.19	−16.48	−1.50	−15.32	−16.48	−2.11	−1.04	−15.33	−16.48
41	7572.7	79.1	(0 3 3)	1_2	10.01	−8.56	−16.48	10.00	−15.00	−16.48	10.01	9.99	−15.03	−16.48
42	7582.7	89.1	(0 3 3)	1_3	0.00	0.00	0.00	0.00	0.00	0.00	0.00	0.00	0.00	0.00
43	7840.9	70.8	(1 2 0)	1_1	6.16	−5.88	−8.37	6.59	−7.44	−8.37	6.16	7.07	−7.41	−8.37
44	7840.9	70.8	(1 2 0)	1_1	17.44	−1.02	−8.37	17.65	−7.04	−8.37	17.44	17.87	−7.04	−8.37
45	7858.8	88.7	(1 2 0)	1_0	0.00	0.00	0.00	0.00	0.00	0.00	0.00	0.00	0.00	0.00
46	7873.4	2.3	(1 2 2)	1_3	73.41	60.70	57.05	73.03	58.24	57.05	73.41	72.75	58.26	57.05
47	7878.1	7.0	(1 2 2)	1_3	71.51	59.98	56.00	74.19	56.94	56.00	71.51	77.77	56.82	56.00
48	7959.6	88.5	(1 2 2)	1_2	0.00	0.00	0.00	0.00	0.00	0.00	0.00	0.00	0.00	0.00
49	7959.6	88.5	(1 2 2)	1_2	0.00	0.00	0.00	0.00	0.00	0.00	0.00	0.00	0.00	0.00
50	7990.3	119.2	(1 2 2)	1_1	−30.45	−50.38	−56.22	−30.59	−54.94	−56.22	−30.45	−30.66	−54.86	−56.23
51	7990.3	119.2	(1 2 2)	1_1	−30.13	−46.89	−53.33	−29.94	−52.11	−53.33	−30.13	−30.54	−52.04	−53.33
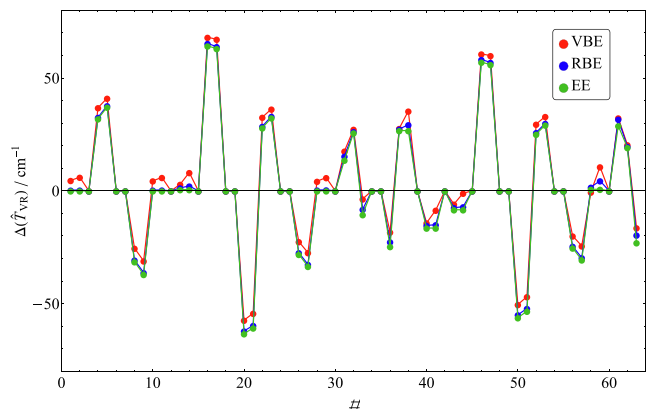
Fig. 7. The differences, $\Delta(\hat{T}_{VR})$, of the $J = 1$ rovibrational energy levels of H_3^+ using the exact Hamiltonian, $\hat{H}_{VR}$, and the Coriolis-free Hamiltonian, $\hat{H}_{VR} - \hat{T}_{VR}$. The results are presented using valence bisector (VBE), Radau bisector (RBE), and Eckart (EE) embeddings.

Fig. 8. The differences, $\Delta(\hat{T}_{VR})_{RR}$, of the $J = 1$ rovibrational energy levels of H_3^+ using the RR Hamiltonian, $\hat{H}_{RR}$, and the Coriolis-free Hamiltonian, $\hat{H}_{RR} - \hat{T}_{VR}$. The results are presented using valence bisector (VBE), Radau bisector (RBE), and Eckart (EE) embeddings.

however, unlike the first group, these are the 1_1 rotational quantum number states.

Taking a closer look at the energy levels of the linear embeddings, we can see that there is a pattern, which most of the CFA levels follow. This pattern is very close to the pattern obtained from the rigid rotor (RR) approximation. In order

to confirm this observation, we created model energy levels using variational vibrational states along with rotational excitations, according to the RR model, and subtracted them from the rovibrational energy levels computed within the CFA resulting in the $\Delta(\hat{T}_{VR})_{RR}$ differences (see Fig. 8). Comparing Fig. 8 to Fig. 7, we can see that the errors on the RR model plot are sig-

Table 9
Numerical values of the $\mathbf{G}_R$ and $\mathbf{G}_{VR}$ tensor elements of $^{16}O_3$ for all of the embeddings studied. For more details on the notation, see caption to Table 2.

Coord.	Embedding	Symmetry	G_{xx}	G_{xy}	G_{yy}	G_{zz}	FNGR	G_{1z}	G_{2z}	G_{3z}
					$\mathbf{G}_R$		FNGR		$\mathbf{G}_{VR}$	
valence	bisector	C_{2v} (Ref.)	7.13	0	0.90	1.01	0.21	1.40	−1.40	0
valence	r_1	C_{2v} (Ref.)	5.42	−2.78	2.61	2.61	1.81	0	2.79	2.85
Radau	Eckart	C_{2v} (Ref.)	7.13	0	0.90	0.80	0	0	0	0
Radau	bisector	C_{2v} (Ref.)	7.13	0	0.90	0.80	0	0	0	0
Radau	r_1	C_{2v} (Ref.)	6.43	−1.96	1.60	1.60	0.80	0	0	1.01
s-Jacobi	bisector	C_{2v} (Ref.)	4.01	3.12	4.01	2.01	1.21	0	0	3.12
s-Jacobi	R	C_{2v} (Ref.)	7.13	0.00	0.90	7.13	6.33	0	0	−7.13
s-Jacobi	r	C_{2v} (Ref.)	7.13	0	0.90	0.90	0.10	0	0	0.90
a-Jacobi	bisector	C_{2v} (Ref.)	6.94	−1.07	1.09	0.94	0.14	0	0	0.50
a-Jacobi	R	C_{2v} (Ref.)	6.88	−1.23	1.15	1.15	0.35	0	0	0.79
a-Jacobi	r	C_{2v} (Ref.)	5.42	−2.78	2.61	2.61	1.81	0	0	1.78
valence	bisector	C_{2v} (10, 10)	8.57	0	0.66	0.74	0.13	1.11	−1.11	0
valence	r_1	C_{2v} (10, 10)	7.08	−3.09	2.15	2.15	1.54	0	2.23	2.21
Radau	Eckart	C_{2v} (10, 10)	8.57	0	0.66	0.62	0.003	−0.11	0.11	0
Radau	bisector	C_{2v} (10, 10)	8.57	0	0.66	0.62	0	0	0	0
Radau	r_1	C_{2v} (10, 10)	8.00	−2.04	1.23	1.23	0.62	0	0	0.64
s-Jacobi	bisector	C_{2v} (10, 10)	4.62	3.95	4.62	2.31	1.69	0	0	3.95
s-Jacobi	R	C_{2v} (10, 10)	8.57	0	0.66	8.57	7.95	0	0	−8.57
s-Jacobi	r	C_{2v} (10, 10)	8.57	0	0.66	0.66	0.05	0	0	0.66
a-Jacobi	bisector	C_{2v} (10, 10)	8.40	−1.13	0.83	0.75	0.14	0	0	0.37
a-Jacobi	R	C_{2v} (10, 10)	8.37	−1.24	0.86	0.86	0.25	0	0	0.49
a-Jacobi	r	C_{2v} (10, 10)	7.08	−3.09	2.15	2.15	1.54	0	0	1.23
valence	bisector	C_s (10, 0)	7.30	−0.60	0.94	1.05	0.25	1.55	−1.27	0.47
valence	r_1	C_s (10, 0)	6.09	−2.57	2.15	2.15	1.36	0	2.54	2.45
Radau	Eckart	C_s (10, 0)	7.33	0.36	0.91	0.80	0.004	−0.004	0.005	−0.07
Radau	bisector	C_s (10, 0)	7.33	−0.36	0.91	0.81	0.02	0	0	0.14
Radau	r_1	C_s (10, 0)	6.85	−1.73	1.39	1.39	0.60	0	0	0.87
s-Jacobi	bisector	C_s (10, 0)	5.03	3.10	3.21	1.96	1.17	0	0	2.95
s-Jacobi	R	C_s (10, 0)	6.94	1.57	1.30	6.94	6.15	0	0	−6.77
s-Jacobi	r	C_s (10, 0)	7.35	0.20	0.89	0.89	0.10	0	0	0.87
a-Jacobi	bisector	C_s (10, 0)	7.28	−0.70	0.97	0.85	0.06	0	0	0.29
a-Jacobi	R	C_s (10, 0)	6.99	−1.49	1.25	1.25	0.46	0	0	0.81
a-Jacobi	r	C_s (10, 0)	6.09	−2.57	2.15	2.15	1.36	0	0	1.39

nificantly smaller, below $10\,\mathrm{cm}^{-1}$ for the first 30 states. The biggest differences between the two plots occur for the second group of energy levels. In fact, the rovibrational energy levels in the first group follow the RR model closely. The rovibrational energy levels in the second group do not follow the RR model; therefore, these states have larger CC. In the CFA, the latter levels also become RR-like, which causes the larger $\Delta(\hat{T}_{VR})$ errors. These findings indicate that the substantial Coriolis-

coupling of H_3^+ is the reason behind the non-rigidity of the system.

All in all, the EE and RBE embeddings are most effective for H_3^+, as predicted. Although similar in performance, EE is consistently better, especially for the first energy level group containing most of the singly degenerate vibrations. Note that insofar as rovibrational energy levels are concerned, we provide no explicit data for the FEE embeddings. This is because the RFEE (following the

Table 10

$J = 1$ rovibrational energy levels of $^{16}O_3$ using the exact Hamiltonian, $\hat{H}_{VR}$, and the differences of the eigenvalues, $\Delta(\hat{T}_{VR})$, obtained with the full and the Coriolis-free Hamiltonian, $\hat{H}_{VR} - \hat{T}_{VR}$. The results are presented in cm^{-1} using valence and Radau coordinates with r_1, bisector, and Eckart embeddings and with symmetric and asymmetric Jacobi coordinates with r, R, and bisector embeddings. The $\hat{H}_{VR}$ levels are given relative to the ZPVE (abs) as well as to the vibrational parent state. The vibrational (vib, $(v_1 v_2 v_3)$) and the rotational (rot, $J_{K_a K_c}$) quantum numbers are assigned for each state.

	$\hat{H}_{VR}$				$\Delta(\hat{T}_{VR})$										
					valence		Radau			s-Jacobi			a-Jacobi		
#	abs	level	vib	rot	r_1	VBE	r_1	RBE	EE	r	R	sJBE	r	R	aJBE
1	0.84	0.84	(0 0 0)	1_{01}	0.90	0.107	0.40	0.000	0.000	0.049	3.17	0.61	0.90	0.174	0.071
2	3.96	3.96	(0 0 0)	1_{11}	0.89	0.104	0.39	0.000	0.000	0.050	3.14	0.60	0.89	0.174	0.070
3	4.01	4.01	(0 0 0)	1_{10}	0.00	0.000	0.00	0.000	0.000	0.000	0.00	0.00	0.00	0.000	0.000
4	695.90	0.84	(0 1 0)	1_{01}	0.90	0.107	0.40	0.001	0.001	0.050	3.23	0.62	0.90	0.176	0.072
5	699.08	4.01	(0 1 0)	1_{11}	0.89	0.104	0.39	0.001	0.001	0.051	3.20	0.62	0.89	0.174	0.070
6	699.13	4.07	(0 1 0)	1_{10}	0.00	0.000	0.00	0.000	0.000	0.000	0.00	0.00	0.00	0.000	0.000
7	1049.49	0.83	(0 0 1)	1_{01}	0.90	0.115	0.40	0.005	0.004	0.052	3.13	0.60	0.90	0.176	0.076
8	1052.56	3.90	(0 0 1)	1_{11}	0.89	0.108	0.39	0.005	0.004	0.055	3.04	0.58	0.89	0.177	0.074
9	1052.62	3.96	(0 0 1)	1_{10}	0.00	0.000	0.00	0.000	0.000	0.000	0.00	0.00	0.00	0.000	0.000
10	1097.64	0.84	(1 0 0)	1_{01}	0.89	0.101	0.39	−0.005	−0.005	0.044	3.17	0.61	0.89	0.169	0.066
11	1100.77	3.97	(1 0 0)	1_{11}	0.88	0.099	0.39	−0.004	−0.005	0.046	3.14	0.60	0.88	0.168	0.065
12	1100.82	4.01	(1 0 0)	1_{10}	0.00	0.000	0.00	0.000	0.000	0.000	0.00	0.00	0.00	0.000	0.000
13	1388.26	0.83	(0 2 0)	1_{01}	0.91	0.107	0.40	0.002	0.002	0.051	3.29	0.64	0.91	0.177	0.073
14	1391.49	4.07	(0 2 0)	1_{11}	0.88	0.104	0.39	0.002	0.002	0.053	3.25	0.63	0.88	0.173	0.071
15	1391.55	4.12	(0 2 0)	1_{10}	0.00	0.000	0.00	0.000	0.000	0.000	0.00	0.00	0.00	0.000	0.000
16	1728.56	0.82	(0 1 1)	1_{01}	0.90	0.115	0.40	0.005	0.004	0.052	3.18	0.62	0.90	0.177	0.076
17	1731.69	3.95	(0 1 1)	1_{11}	0.88	0.107	0.39	0.005	0.004	0.055	3.09	0.59	0.88	0.176	0.073
18	1731.74	4.01	(0 1 1)	1_{10}	0.00	0.000	0.00	0.000	0.000	0.000	0.00	0.00	0.00	0.000	0.000
19	1784.95	0.84	(1 1 0)	1_{01}	0.90	0.102	0.39	−0.003	−0.003	0.046	3.23	0.62	0.90	0.171	0.068
20	1788.14	4.02	(1 1 0)	1_{11}	0.87	0.099	0.38	−0.003	−0.003	0.047	3.20	0.61	0.87	0.168	0.065
21	1788.18	4.07	(1 1 0)	1_{10}	0.00	0.000	0.00	0.000	0.000	0.000	0.00	0.00	0.00	0.000	0.000
22	2069.80	0.82	(0 0 2)	1_{01}	0.90	0.119	0.39	0.006	0.004	0.050	3.09	0.60	0.90	0.174	0.077
23	2072.83	3.85	(0 0 2)	1_{11}	0.88	0.107	0.39	0.006	0.004	0.055	2.95	0.56	0.88	0.176	0.073
24	2072.89	3.91	(0 0 2)	1_{10}	0.00	0.000	0.00	0.000	0.000	0.000	0.00	0.00	0.00	0.000	0.000
25	2077.59	0.83	(0 3 0)	1_{01}	0.91	0.107	0.40	0.003	0.003	0.053	3.35	0.66	0.91	0.178	0.074
26	2080.89	4.12	(0 3 0)	1_{11}	0.87	0.104	0.39	0.003	0.003	0.054	3.31	0.65	0.87	0.173	0.071
27	2080.94	4.18	(0 3 0)	1_{10}	0.00	0.000	0.00	0.000	0.000	0.000	0.00	0.00	0.00	0.000	0.000
28	2112.25	0.82	(1 0 1)	1_{01}	0.90	0.113	0.39	0.003	0.002	0.049	3.13	0.60	0.90	0.173	0.073
29	2115.33	3.90	(1 0 1)	1_{11}	0.88	0.105	0.39	0.003	0.002	0.053	3.04	0.58	0.88	0.174	0.071
30	2115.38	3.95	(1 0 1)	1_{10}	0.00	0.000	0.00	0.000	0.000	0.000	0.00	0.00	0.00	0.000	0.000
31	2188.92	0.84	(2 0 0)	1_{01}	0.89	0.097	0.38	−0.008	−0.009	0.040	3.17	0.60	0.89	0.164	0.062
32	2192.05	3.97	(2 0 0)	1_{11}	0.87	0.094	0.38	−0.008	−0.008	0.042	3.13	0.59	0.87	0.163	0.060
33	2192.09	4.01	(2 0 0)	1_{10}	0.00	0.000	0.00	0.000	0.000	0.000	0.00	0.00	0.00	0.000	0.000
34	2404.53	0.82	(0 2 1)	1_{01}	0.90	0.114	0.40	0.006	0.005	0.053	3.24	0.63	0.90	0.178	0.077
35	2407.71	4.00	(0 2 1)	1_{11}	0.87	0.106	0.39	0.006	0.005	0.056	3.14	0.61	0.87	0.175	0.073
36	2407.77	4.06	(0 2 1)	1_{10}	0.00	0.000	0.00	0.000	0.000	0.000	0.00	0.00	0.00	0.000	0.000
37	2469.41	0.83	(1 2 0)	1_{01}	0.90	0.102	0.39	−0.002	−0.001	0.047	3.29	0.64	0.90	0.173	0.069
38	2472.65	4.07	(1 2 0)	1_{11}	0.87	0.100	0.38	−0.002	−0.001	0.049	3.25	0.63	0.87	0.168	0.066
39	2472.70	4.12	(1 2 0)	1_{10}	0.00	0.000	0.00	0.000	0.000	0.000	0.00	0.00	0.00	0.000	0.000
40	2733.77	0.82	(0 1 2)	1_{01}	0.90	0.119	0.40	0.006	0.004	0.051	3.14	0.61	0.90	0.175	0.077
41	2736.85	3.90	(0 1 2)	1_{11}	0.87	0.106	0.39	0.006	0.004	0.056	2.99	0.57	0.87	0.176	0.073
42	2736.91	3.95	(0 1 2)	1_{10}	0.00	0.000	0.00	0.000	0.000	0.000	0.00	0.00	0.00	0.000	0.000
43	2763.35	0.83	(0 4 0)	1_{01}	0.91	0.107	0.40	0.004	0.005	0.054	3.42	0.68	0.91	0.180	0.075
44	2766.71	4.19	(0 4 0)	1_{11}	0.87	0.104	0.38	0.004	0.005	0.055	3.38	0.66	0.87	0.173	0.072
45	2766.77	4.24	(0 4 0)	1_{10}	0.00	0.000	0.00	0.000	0.000	0.000	0.00	0.00	0.00	0.000	0.000
46	2782.12	0.82	(1 1 1)	1_{01}	0.90	0.112	0.39	0.003	0.002	0.050	3.18	0.62	0.90	0.174	0.074
47	2785.25	3.95	(1 1 1)	1_{11}	0.87	0.104	0.39	0.003	0.002	0.053	3.08	0.59	0.87	0.173	0.071
48	2785.31	4.00	(1 1 1)	1_{10}	0.00	0.000	0.00	0.000	0.000	0.000	0.00	0.00	0.00	0.000	0.000
49	2868.04	0.83	(2 1 0)	1_{01}	0.89	0.098	0.39	−0.007	−0.007	0.042	3.23	0.62	0.89	0.167	0.064
50	2871.22	4.02	(2 1 0)	1_{11}	0.86	0.095	0.38	−0.007	−0.006	0.044	3.19	0.61	0.86	0.163	0.061
51	2871.27	4.06	(2 1 0)	1_{10}	0.00	0.000	0.00	0.000	0.000	0.000	0.00	0.00	0.00	0.000	0.000

Radau angle) is once again equivalent to RBE, while VFEE is very close to it.

5.5. $^{16}O_3$

Despite having three identical atoms, the ozone molecule, $^{16}O_3$, has only C_{2v} point-group symmetry at its equilibrium structure. Consisting of only heavy atoms, CC is expected to be very small for this system. On the other hand, there are three equivalent versions [30] of the C_{2v} equilibrium structure, which complicates matters a bit vis-à-vis the embeddings, and the rovibrational level structure. Since the barriers between adjacent PES wells of $^{16}O_3$ are quite high, it is possible to focus on embeddings and levels that are centered on just a single equilibrium structure. Note, that if only one version is treated in contrast to when all versions are considered, than due to its C_{2v} point-group symmetry at the equilibrium structure, similarly to $H_2^{16}O$ separate symmetric and asymmetric Jacobi embeddings can be defined.

Inspection of the G_R and G_{VR} tensor elements (see Table 9) reveals a similar pattern to the $H_2^{16}O$ molecule when comparing the different embeddings. Of course, all of the FNGR norm values are significantly smaller for $^{16}O_3$, as expected. Similarly to $H_2^{16}O$, the best embeddings here are EE and RBE, with FNGR norm values consistently smaller than 0.1 cm^{-1}. There are also some similarities with H_3^+, owing to the three identical masses, such as the very large difference between RBE and VBE (with the VBE results being significantly worse). Also, aJBE here again seems to mimic RBE very closely. Surprisingly, sJrE has also very small norm values, while it is clear, as well, that the sJRE embedding is by far the worst, with norms of 6–8 cm^{-1}.

Computed CFA rovibrational energy levels are listed in Table 10. In addition to verifying our predictions (as discussed below), we also comment that, unlike for $H_2^{16}O$, the CFA rotational band structure does not show significant vibrational-state dependence—further evidence of the better rotation/vibration separability for this system. For $J = 1$, the RBE and EE errors are smaller than 0.01 cm^{-1} (see Fig. 9), while VBE is indeed an order of magnitude worse, having errors around 0.1 cm^{-1}. Indeed, even aJBE is better than VBE, with errors around 0.07 cm^{-1}. Since the ozone molecule is very close to a prolate symmetric top, aJrE, which yields prolate energy levels in the CFA, performs very well, with errors of only 0.05 cm^{-1}. At the same time, aJRE, which results in oblate energy levels, is by far the worst choice, with errors of 3.2 cm^{-1}. The performance of the rest of the embeddings (e.g., Vr_1E, Rr_1E and sJBE) is average, with errors ranging between 0.4–0.9 cm^{-1}.

Upon taking a closer look at the RBE and EE errors (see Fig. 9), there is still an observable finer structure of the energy levels. The antisymmetric stretch vibrations, (0 0 1) and overtones, seem to have a constant positive error, while the bending fundamental, (0 1 0), and its overtones show an increasing positive error. The symmetric stretch fundamental, (1 0 0), however, shows a negative error which increases upon further excitations. Also, it is observable from Fig. 9 that the RBE and EE errors are very close. Due to the very small errors it is hard to decide which of the two is the better embedding for this system. For $J = 5$, the VBE errors increase up to 0.2–1.6 cm^{-1}, while the RBE and EE errors are still smaller than 0.1 cm^{-1} for the first 80 states (see Fig. 10).

Having discussed the single-PES-well situation for ozone, we now return to a consideration of the three-identical-well version. To address this case, we have computed rovibrational energy levels for all three wells in a single computation (see Table 11). For valence and Radau coordinates, the embeddings best suited to describe one minimum would perform badly for the states centered in the other two wells. In particular, RBE and EE has 0.3 cm^{-1} $\Delta(\hat{T}_{VR})$ error for the other two wells, while VBE performs
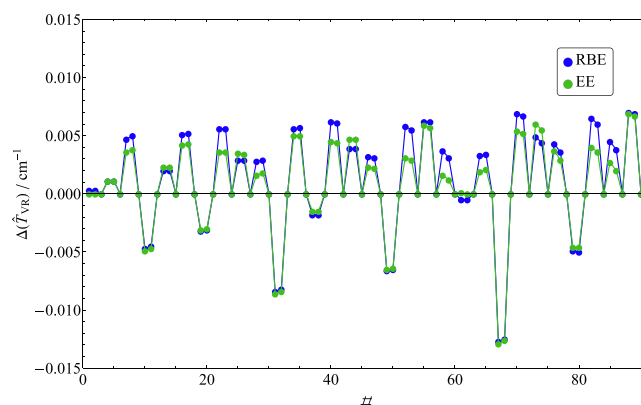

Fig. 9. The differences, $\Delta(\hat{T}_{VR})$, of the $J = 1$ rovibrational energy levels of $^{16}O_3$ using the exact Hamiltonian, $\hat{H}_{VR}$, and the Coriolis-free Hamiltonian, $\hat{H}_{VR} - \hat{T}_{VR}$. The results are presented using Radau bisector (RBE), and Eckart (EE) embeddings.
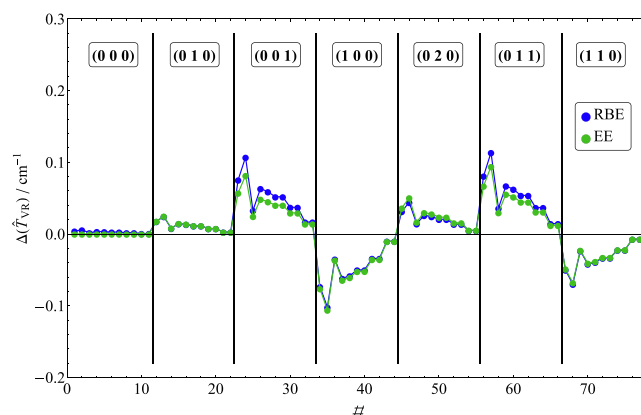

Fig. 10. The differences, $\Delta(\hat{T}_{VR})$, of the $J = 5$ rovibrational energy levels of $^{16}O_3$ using the exact Hamiltonian, $\hat{H}_{VR}$, and the Coriolis-free Hamiltonian, $\hat{H}_{VR} - \hat{T}_{VR}$. The results are presented using Radau bisector (RBE), and Eckart (EE) embeddings.

slightly better, with errors around 0.2 cm^{-1}. The simplest of the three coordinate choices is the case of Jacobi coordinates. Here, the symmetric and asymmetric Jacobi coordinates actually describe different wells, so the CFA errors will be the same in Table 11 as reported for a single well in Table 10, considering both symmetric and asymmetric sets (the latter counted twice). In this case, unlike for the linear embeddings, JBE describes two of the three wells with tiny errors of 0.07 cm^{-1}, while the errors for the third well are around 0.6 cm^{-1}.

In summary, our results show that a single version of $^{16}O_3$ can be described very accurately within the CFA using RBE or EE, but is not possible to describe all version with the same accuracy within a single computation.

5.6. $^{14}NH_3$

The nuclear dynamics of the tetratomic ammonia molecule ($^{14}NH_3$) is characterized by a large-amplitude (inversion) motion, which makes this molecule an important benchmark system both for experimental spectroscopy and nuclear-motion computations [71], and a prime non-triatomic candidate for our study of CFA. Having more than three atoms, none of our earlier derivations regarding the structure of the g and G tensors for planar, triatomic molecules apply for $^{14}NH_3$. Indeed, most of the G_R and G_{VR} tensor elements are nonzero, for a randomly picked geometry. $^{14}NH_3$

Table 11

$J = 1$ rovibrational energy levels of $^{16}O_3$ using the exact Hamiltonian, $\hat{H}_{VR}$, and the differences of the eigenvalues, $\Delta(\hat{T}_{VR})$, obtained with the full and the Coriolis-free Hamiltonian, $\hat{H}_{VR} - \hat{T}_{VR}$. The results are presented in cm^{-1} using valence and Radau coordinates with bisector and Eckart embeddings and Jacobi coordinates with r, R, and bisector embeddings they are given relative to the vibrational parent state. The vibrational (vib, $(v_1 v_2 v_3)$) and the rotational (rot, $J_{K_a K_c}$) quantum numbers are assigned for each state.

| | | $\hat{H}_{VR}$ | | $\Delta(\hat{T}_{VR})$ | | | | | | |
| | | | | valence | | Radau | | Jacobi | | |
#	level	vib	rot	VBE	EE	RBE	EE	r	R	JBE
1	0.840	(0 0 0)	1_{01}	0.201	0.328	0.330	0.328	0.902	0.174	0.071
2	0.840	(0 0 0)	1_{01}	0.201	0.328	0.330	0.328	0.902	0.174	0.071
3	0.840	(0 0 0)	1_{01}	0.107	0.000	0.000	0.000	0.049	3.174	0.609
4	3.963	(0 0 0)	1_{11}	0.200	0.323	0.325	0.323	0.893	0.174	0.070
5	3.963	(0 0 0)	1_{11}	0.200	0.323	0.325	0.323	0.893	0.174	0.070
6	3.963	(0 0 0)	1_{11}	0.104	0.000	0.000	0.000	0.050	3.144	0.601
7	4.014	(0 0 0)	1_{10}	0.000	0.000	0.000	0.000	0.000	0.000	0.000
8	4.014	(0 0 0)	1_{10}	0.000	0.000	0.000	0.000	0.000	0.000	0.000
9	4.014	(0 0 0)	1_{10}	0.000	0.000	0.000	0.000	0.000	0.000	0.000
10	0.837	(0 1 0)	1_{01}	0.203	0.330	0.334	0.330	0.903	0.176	0.072
11	0.837	(0 1 0)	1_{01}	0.203	0.330	0.334	0.330	0.903	0.176	0.072
12	0.836	(0 1 0)	1_{01}	0.107	0.001	0.001	0.001	0.050	3.230	0.624
13	4.015	(0 1 0)	1_{11}	0.199	0.323	0.327	0.323	0.886	0.174	0.070
14	4.015	(0 1 0)	1_{11}	0.199	0.323	0.327	0.323	0.886	0.174	0.070
15	4.015	(0 1 0)	1_{11}	0.104	0.001	0.001	0.001	0.051	3.198	0.616
16	4.066	(0 1 0)	1_{10}	0.000	0.000	0.000	0.000	0.000	0.000	0.000
17	4.066	(0 1 0)	1_{10}	0.000	0.000	0.000	0.000	0.000	0.000	0.000
18	4.066	(0 1 0)	1_{10}	0.000	0.000	0.000	0.000	0.000	0.000	0.000
19	0.828	(0 0 1)	1_{01}	0.115	0.004	0.333	0.331	0.902	0.176	0.076
20	0.828	(0 0 1)	1_{01}	0.204	0.331	0.333	0.331	0.902	0.176	0.076
21	0.828	(0 0 1)	1_{01}	0.204	0.331	0.005	0.004	0.052	3.129	0.604
22	3.901	(0 0 1)	1_{11}	0.108	0.004	0.322	0.319	0.888	0.177	0.074
23	3.902	(0 0 1)	1_{11}	0.202	0.319	0.322	0.319	0.888	0.177	0.074
24	3.902	(0 0 1)	1_{11}	0.202	0.319	0.005	0.004	0.055	3.041	0.579
25	3.956	(0 0 1)	1_{10}	0.000	0.000	0.000	0.000	0.000	0.000	0.000
26	3.956	(0 0 1)	1_{10}	0.000	0.000	0.000	0.000	0.000	0.000	0.000
27	3.956	(0 0 1)	1_{10}	0.000	0.000	0.000	0.000	0.000	0.000	0.000

has two important structures on its PES: the (two equivalent) global minima have C_{3v} point-group symmetry, while the transition state (TS) structure of the inversion motion has D_{3h} point-group symmetry. $^{14}NH_3$, similarly to H_3^+, is an oblate symmetric top.

For $^{14}NH_3$, we choose a "valence" vibrational coordinate set which is very close to the normal coordinates describing the harmonic vibrations (about any of the structures above). The r_1, r_2, and r_3 coordinates describe the N–H stretching motions, β describes the inversion motion, while θ_1 and θ_2 are the two dihedral coordinates of the second and third hydrogen atoms. Implicit in this description of the vibrational coordinates is also the description of a particular embedding, known as the "zxz" (scattering) embedding (zxzE). Specifically, the three H atoms define the horizontal or x–y plane, within which the first H atom defines the direction of the x axis. The EE can be used, as well, with both the C_{3v} and D_{3h} stationary points as natural reference structures. Finally, the FEE is also a very natural choice, particularly if the flexible path is chosen to follow the inversion coordinate, as we did here. The other five coordinates were fixed at their value at the D_{3h} reference geometry.

Table 12 lists FNGR norm values, $\|\mathbf{G}_R - \mathbf{g}_R^{-1}\|_F$, for each embedding at the two reference structures and several distorted geometries (see Table S15). For ammonia, v_2 corresponds to the inversion motion, v_1 to the breathing stretch motion, v_{3s} and v_{3a} represent the symmetric and asymmetric stretching, while v_{4s} and v_{4a} is the symmetric and asymmetric bending. Since we proved earlier that the FNGR norm is a reliable measure for assessing CC, the individual $\mathbf{G}_{VR}$ (and $\mathbf{G}_R$) tensor elements are not shown here. (Note that instead of the three nonzero $\mathbf{G}_{VR}$ elements for triatomic molecules, there are up to 18 nonzero elements for ammonia.) It is obvious from Table 12 that the CC is very substantial for the zxz embedding, across the board. The value of the FNGR norm is 33 cm^{-1} at the C_{3v}

and 25 cm^{-1} at the D_{3h} reference structures. The zxzE norm stays in the 18–47 cm^{-1} range for vibrational excitation, generally being

Table 12

Numerical values of $\|\mathbf{G}_R - \mathbf{g}_R^{-1}\|_F$ (FNGR), the Frobenius norm of the $(\mathbf{G}_R - \mathbf{g}_R^{-1})$ tensor, of $^{14}NH_3$ for all of the embeddings studied in this paper. The numbers are provided in cm^{-1} in the C_{3v} and D_{3h} reference geometries and the distorted geometries along each vibrational band origin (v_n). In case of the degenerate vibrations, the s indicate symmetric, while the a asymmetric distortion. The degree of distortion (dist.) is 10% of the equilibrium value of the excited vibrational coordinates in each case mentioned here. For the actual geometries, see Table S15.

| Geom. | Dist. | zxz | Eckart | | |
			C_{3v}	D_{3h}	flexible
C_{3v} (1)	ref.	33.11	0	5.42	0
C_{3v} (1)	v_2	46.45	0.91	12.97	0
C_{3v} (1)	v_{4s}	36.84	0.36	9.32	0.78
C_{3v} (1)	v_{4a}	33.57	0.15	7.22	0.40
C_{3v} (1)	v_1	27.36	0	4.48	0
C_{3v} (1)	v_{3s}	27.25	0.16	7.39	0.59
C_{3v} (1)	v_{3a}	33.61	0.15	6.71	0.47
D_{3h}	ref.	24.99	6.12	0	0
D_{3h}	v_2	26.45	1.83	0.92	0
D_{3h}	v_{4s}	24.96	8.46	0.31	1.37
D_{3h}	v_{4a}	24.98	7.25	0.19	0.76
D_{3h}	v_1	20.65	5.05	0	0
D_{3h}	v_{3s}	18.01	7.61	0.14	0.62
D_{3h}	v_{3a}	25.06	6.96	0.13	0.51
C_{3v} (2)	ref.	33.11	40.80	5.42	0
C_{3v} (2)	v_2	46.45	107.76	12.97	0
C_{3v} (2)	v_{4s}	36.84	68.53	9.32	0.78
C_{3v} (2)	v_{4a}	33.57	52.79	7.22	0.40
C_{3v} (2)	v_1	27.36	33.72	4.48	0
C_{3v} (2)	v_{3s}	27.25	54.72	7.39	0.59
C_{3v} (2)	v_{3a}	33.61	49.04	6.71	0.47

smaller around the TS structure. In any event, these are all enormous values—no doubt stemming from the fact that one of the three H atoms is unrealistically singled out for purposes of defining the embedding.

In contrast, EE with a C_{3v} reference structure yields much better results in the vicinity of the C_{3v} reference geometry itself, as expected. Just at the C_{3v} global minimum, the FNGR norm is zero, with reasonably large vibrational distortions about this geometry giving rise to norm values generally smaller than 1 cm^{-1}. Of course, this choice is much less well behaved in the vicinity of the D_{3h} TS, where norm values are all on the order of 8 cm^{-1}—except for the v_2 distortion, corresponding to the inversion motion itself. EE with the D_{3h} reference-structure choice naturally shows a reverse behavior, with norms smaller

than 1 cm^{-1} around the its reference structure and norms of 5–13 cm^{-1} around the C_{3v} geometry.

As to the rovibrational levels, due to the "fluxional" nature of $^{14}NH_3$, these are known to be delocalized across both C_{3v} wells—even at low energies. Consequently, given the extremely large FNGR norm values for the C_{3v} EE, as evaluated in the opposite C_{3v} well (see Table 12), we did not use this embedding to compute CFA rovibrational levels. Instead, the D_{3h} EE and FEE embeddings were used, as both of those yield reasonably small norm values everywhere. Of course, the FEE FNGR values are very small at all of these geometries, and at all intermediate values of β along the inversion motion that connects them. Therefore, FEE is expected to perform considerably better in the CFA than the D_{3h} EE, which in turn, should be significantly better than zxzE.

Table 13

$J = 1$ rovibrational energy levels of $^{14}NH_3$ using the exact Hamiltonian, $\hat{H}_{VR}$, and the Coriolis-free Hamiltonian, $\hat{H}_{VR} - \hat{T}_{VR}$, and their difference, $\Delta(\hat{T}_{VR})$. The results are presented in cm^{-1} using valence coordinates with zxz, Eckart, and flexible-Eckart (FEE) embeddings and they are given relative to the ZPVE (abs) as well as relative to the vibrational parent state (rel). The vibrational (vib, v_n) and the rotational (rot, J_K) quantum numbers are assigned for each state.

#	$\hat{H}_{VR}$				$(\hat{H}_{VR} - \hat{T}_{VR})_{abs}$			$(\hat{H}_{VR} - \hat{T}_{VR})_{rel}$			$\Delta(\hat{T}_{VR})$		
	abs	rel	vib	rot	zxzE	EE	FEE	zxzE	EE	FEE	zxzE	EE	FEE
1	16.2	16.2	v_0^+	1_1	32.8	18.9	16.2	32.8	18.9	16.2	16.59	2.69	0.06
2	16.2	16.2	v_0^+	1_1	33.9	18.9	16.2	33.9	18.9	16.2	17.69	2.69	0.06
3	17.0	16.2	v_0^-	1_1	33.6	19.7	17.0	32.8	18.9	16.2	16.60	2.70	0.06
4	17.0	16.2	v_0^-	1_1	34.5	19.7	17.0	33.7	18.9	16.2	17.53	2.70	0.06
5	19.9	19.9	v_0^+	1_0	20.8	25.3	20.0	20.8	25.3	20.0	0.95	5.41	0.10
6	20.7	19.9	v_0^-	1_0	21.5	26.1	20.8	20.7	25.3	20.0	0.79	5.43	0.10
7	948.6	16.2	v_2^+	1_1	964.5	950.9	948.9	32.1	18.4	16.4	15.90	2.28	0.23
8	948.6	16.2	v_2^+	1_1	963.7	950.9	948.9	31.2	18.4	16.4	15.09	2.28	0.23
9	952.6	20.1	v_2^+	1_0	954.4	957.2	953.1	21.9	24.7	20.6	1.81	4.60	0.44
10	984.2	16.0	v_2^-	1_1	1000.5	986.8	984.5	32.4	18.6	16.3	16.36	2.60	0.28
11	984.2	16.0	v_2^-	1_1	1000.4	986.8	984.5	32.3	18.6	16.3	16.23	2.60	0.28
12	987.9	19.8	v_2^-	1_0	990.7	993.1	988.4	22.6	25.0	20.3	2.82	5.24	0.54
13	1613.6	16.1	$2v_2^+$	1_1	1628.8	1615.5	1614.0	31.3	18.0	16.5	15.17	1.85	0.40
14	1613.6	16.1	$2v_2^+$	1_1	1628.4	1615.5	1614.0	30.9	18.0	16.5	14.78	1.85	0.40
15	1617.9	20.4	$2v_2^+$	1_0	1619.7	1621.6	1618.7	22.2	24.1	21.2	1.89	3.76	0.82
16	1639.5	13.3	v_4^+	1_1	1658.9	1645.1	1642.5	32.8	19.0	16.3	19.44	5.64	2.95
17	1639.5	13.3	v_4^+	1_1	1659.4	1645.2	1642.7	33.2	19.0	16.5	19.89	5.72	3.15
18	1640.6	13.3	v_4^-	1_1	1660.0	1646.2	1643.6	32.8	19.0	16.3	19.46	5.66	2.97
19	1640.6	13.3	v_4^-	1_1	1660.5	1646.3	1643.8	33.2	19.0	16.5	19.91	5.75	3.17
20	1645.3	19.1	v_4^+	1_1	1659.9	1645.2	1642.7	33.7	19.0	16.5	14.66	−0.04	−2.61
21	1645.9	19.7	v_4^+	1_1	1660.2	1645.3	1642.9	34.0	19.1	16.7	14.36	−0.55	−3.01
22	1646.4	19.1	v_4^-	1_1	1660.8	1646.3	1643.8	34.6	20.1	17.6	14.40	−0.04	−2.62
25	1647.2	19.9	v_4^-	1_1	1661.1	1646.4	1644.0	33.8	19.1	16.7	13.89	−0.79	−3.26
23	1646.6	20.4	v_4^+	1_0	1647.3	1651.8	1646.6	21.1	25.6	20.4	0.73	5.29	0.07
24	1646.6	20.4	v_4^+	1_0	1647.4	1651.8	1646.6	20.2	24.6	19.3	0.89	5.30	0.07
26	1647.7	20.4	v_4^-	1_0	1648.1	1653.0	1647.7	20.8	25.7	20.4	0.36	5.22	−0.03
27	1647.7	20.4	v_4^-	1_0	1648.3	1653.0	1647.7	21.0	25.7	20.4	0.56	5.22	−0.03
28	1898.0	15.9	$2v_2^-$	1_1	1914.6	1900.8	1898.5	32.4	18.7	16.3	16.58	2.81	0.49
29	1898.0	15.9	$2v_2^-$	1_1	1914.2	1900.8	1898.5	32.1	18.7	16.3	16.21	2.81	0.49
30	1901.5	19.4	$2v_2^-$	1_0	1904.2	1907.2	1902.5	22.1	25.0	20.4	2.75	5.67	0.98
31	2399.8	15.7	$3v_2^+$	1_1	2416.6	2402.8	2400.4	32.5	18.7	16.3	16.84	3.04	0.66
32	2399.8	15.7	$3v_2^+$	1_1	2416.2	2402.8	2400.4	32.1	18.7	16.3	16.46	3.04	0.66
33	2403.1	19.0	$3v_2^+$	1_0	2406.2	2409.2	2404.4	22.1	25.1	20.3	3.09	6.12	1.33
34	2554.1	13.7	$(v_2 + v_4)^+$	1_1	2571.3	2558.9	2556.8	30.9	18.5	16.4	17.13	4.75	2.69
35	2554.1	13.7	$(v_2 + v_4)^+$	1_1	2571.8	2559.0	2557.0	31.4	18.6	16.7	17.66	4.85	2.93
36	2559.1	18.7	$(v_2 + v_4)^+$	1_1	2572.4	2559.0	2557.0	32.0	18.6	16.7	13.34	−0.11	−2.03
37	2559.6	19.2	$(v_2 + v_4)^+$	1_1	2572.9	2559.1	2557.3	32.5	18.7	16.9	13.27	−0.53	−2.30
38	2561.0	20.6	$(v_2 + v_4)^+$	1_0	2562.8	2565.4	2561.5	22.4	25.0	21.1	1.76	4.39	0.50
39	2561.0	20.6	$(v_2 + v_4)^+$	1_0	2562.8	2565.4	2561.5	22.4	25.0	21.1	1.78	4.40	0.50
40	2599.2	13.2	$(v_2 + v_4)^-$	1_1	2617.7	2604.7	2602.3	31.8	18.7	16.3	18.58	5.50	3.10
41	2599.2	13.2	$(v_2 + v_4)^-$	1_1	2618.2	2604.8	2602.5	32.3	18.8	16.6	19.05	5.59	3.33
42	2604.8	18.9	$(v_2 + v_4)^-$	1_1	2618.4	2604.8	2602.5	32.5	18.8	16.6	13.57	−0.06	−2.32
43	2605.4	19.5	$(v_2 + v_4)^-$	1_1	2618.8	2604.8	2602.7	32.9	18.9	16.8	13.44	−0.56	−2.68
44	2606.1	20.2	$(v_2 + v_4)^-$	1_0	2608.8	2611.3	2606.7	22.9	25.4	20.8	2.66	5.16	0.57
45	2606.1	20.2	$(v_2 + v_4)^-$	1_0	2608.8	2611.3	2606.7	22.9	25.4	20.8	2.68	5.16	0.57
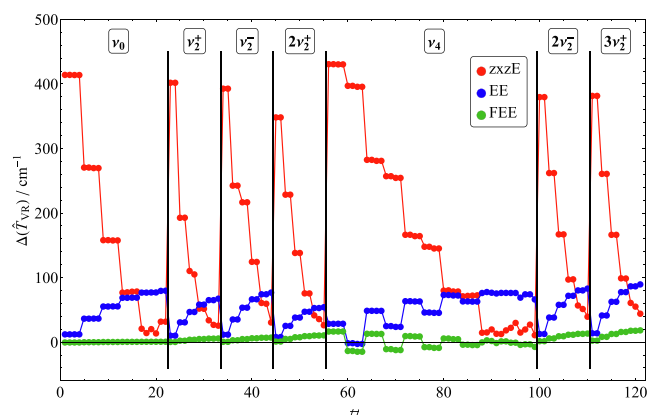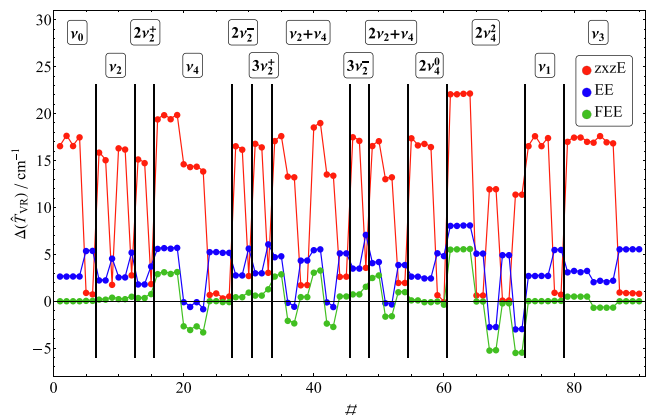
Fig. 11. The differences, $\Delta(\hat{T}_{VR})$, of the $J = 1$ rovibrational energy levels of $^{14}NH_3$ using the exact Hamiltonian, $\hat{H}_{VR}$, and the Coriolis-free Hamiltonian, $\hat{H}_{VR} - \hat{T}_{VR}$. The results are presented using valence zxz (zxzE), Eckart (EE), and flexible-Eckart (FEE) embeddings.

Fig. 12. The differences, $\Delta(\hat{T}_{VR})$, of the $J = 5$ rovibrational energy levels of $^{14}NH_3$ using the exact Hamiltonian, $\hat{H}_{VR}$, and the Coriolis-free Hamiltonian, $\hat{H}_{VR} - \hat{T}_{VR}$. The results are presented using valence zxz (zxzE), Eckart (EE), and flexible-Eckart (FEE) embeddings.

Table 14

$J = 5$ rovibrational energy levels of $^{14}NH_3$ using the exact Hamiltonian, $\hat{H}_{VR}$, and the Coriolis-free Hamiltonian, $\hat{H}_{VR} - \hat{T}_{VR}$, and their difference, $\Delta(\hat{T}_{VR})$. For more details on notations, see caption of Table 13.

	$\hat{H}_{VR}$				$(\hat{H}_{VR} - \hat{T}_{VR})_{abs}$			$(\hat{H}_{VR} - \hat{T}_{VR})_{rel}$			$\Delta(\hat{T}_{VR})$		
#	abs	rel	vib	rot	zxzE	EE	FEE	zxzE	EE	FEE	zxzE	EE	FEE
1	205.3	205.3	v_0^+	5_5	620.2	218.3	205.7	620.2	218.3	205.7	415.0	13.0	0.4
2	205.3	205.3	v_0^+	5_5	620.2	218.3	205.7	620.2	218.3	205.7	415.0	13.0	0.4
3	206.1	205.3	v_0^-	5_5	620.9	219.1	206.5	620.1	218.3	205.7	414.8	13.0	0.4
4	206.1	205.3	v_0^-	5_5	620.9	219.1	206.5	620.1	218.3	205.7	414.8	13.0	0.4
5	238.7	238.7	v_0^+	5_4	510.1	276.0	239.5	510.1	276.0	239.5	271.4	37.3	0.8
6	238.7	238.7	v_0^+	5_4	510.1	276.0	239.5	510.1	276.0	239.5	271.4	37.3	0.8
7	239.4	238.6	v_0^-	5_4	510.0	276.8	240.3	509.2	276.0	239.5	270.6	37.4	0.8
8	239.4	238.6	v_0^-	5_4	510.0	276.8	240.3	509.2	276.0	239.5	270.6	37.4	0.8
9	264.5	264.5	v_0^+	5_3	423.4	320.7	265.6	423.4	320.7	265.6	158.9	56.2	1.1
10	264.5	264.5	v_0^+	5_3	423.5	320.7	265.7	423.5	320.7	265.7	159.0	56.2	1.1
11	265.2	264.4	v_0^-	5_3	423.7	321.6	266.4	422.9	320.8	265.6	158.5	56.3	1.2
12	265.2	264.4	v_0^-	5_3	423.8	321.6	266.4	423.0	320.8	265.6	158.6	56.3	1.2
13	282.9	282.9	v_0^+	5_2	360.6	352.5	284.3	360.6	352.5	284.3	77.7	69.6	1.3
14	282.9	282.9	v_0^+	5_2	361.1	352.5	284.3	361.1	352.5	284.3	78.2	69.6	1.3
15	283.6	282.8	v_0^-	5_2	362.7	353.5	285.0	361.9	352.7	284.2	79.1	69.8	1.4
16	283.6	282.8	v_0^-	5_2	363.0	353.5	285.0	362.2	352.7	284.2	79.4	69.8	1.4
17	294.0	294.0	v_0^+	5_1	315.6	371.6	295.4	315.6	371.6	295.4	21.7	77.7	1.5
18	294.0	294.0	v_0^+	5_1	309.0	371.6	295.4	309.0	371.6	295.4	15.0	77.7	1.5
19	294.6	293.8	v_0^-	5_1	315.7	372.6	296.1	314.9	371.8	295.3	21.1	77.9	1.5
20	294.6	293.8	v_0^-	5_1	309.1	372.6	296.1	308.3	371.8	295.3	14.5	77.9	1.5
21	297.6	297.6	v_0^+	5_0	330.3	378.0	299.2	330.3	378.0	299.2	32.6	80.3	1.5
22	298.3	297.5	v_0^-	5_0	330.9	378.9	299.9	330.1	378.1	299.1	32.6	80.6	1.5
23	1134.8	202.4	v_2^+	5_5	1537.6	1145.8	1136.1	605.1	213.3	203.6	402.8	11.0	1.2
24	1134.8	202.4	v_2^+	5_5	1537.6	1145.8	1136.1	605.1	213.3	203.6	402.8	11.0	1.2
25	1170.6	238.1	v_2^+	5_4	1364.2	1202.2	1173.7	431.7	269.7	241.3	193.6	31.6	3.2
26	1170.6	238.1	v_2^+	5_4	1364.3	1202.2	1173.7	431.8	269.7	241.3	193.7	31.6	3.2
27	1198.2	265.7	v_2^+	5_3	1309.4	1245.8	1202.9	376.9	313.4	270.4	111.2	47.6	4.7
28	1198.2	265.7	v_2^+	5_3	1304.1	1245.8	1202.9	371.6	313.4	270.4	105.9	47.6	4.7
29	1217.8	285.4	v_2^+	5_2	1270.7	1277.0	1223.6	338.2	344.5	291.1	52.9	59.1	5.8
30	1217.8	285.4	v_2^+	5_2	1270.4	1277.0	1223.6	337.9	344.5	291.1	52.6	59.1	5.8
31	1229.6	297.1	v_2^+	5_1	1264.4	1295.6	1236.0	331.9	363.1	303.5	34.8	66.0	6.4
32	1229.6	297.1	v_2^+	5_1	1257.3	1295.6	1236.0	324.8	363.1	303.5	27.7	66.0	6.4
33	1233.5	301.0	v_2^+	5_0	1260.0	1301.8	1240.1	327.5	369.3	307.7	26.5	68.3	6.6
34	1171.4	203.3	v_2^-	5_5	1565.1	1183.9	1172.8	596.9	215.8	204.7	393.7	12.5	1.5
35	1171.4	203.3	v_2^-	5_5	1565.1	1183.9	1172.8	596.9	215.8	204.7	393.7	12.5	1.5
36	1204.9	236.8	v_2^-	5_4	1448.3	1241.0	1208.7	480.2	272.8	240.6	243.4	36.1	3.8
37	1204.9	236.8	v_2^-	5_4	1448.3	1241.0	1208.7	480.2	272.8	240.6	243.4	36.1	3.8
38	1230.9	262.7	v_2^-	5_3	1448.5	1285.2	1236.5	480.4	317.1	268.4	217.6	54.3	5.7
39	1230.9	262.7	v_2^-	5_3	1448.5	1285.2	1236.5	480.4	317.1	268.4	217.6	54.3	5.7
40	1249.4	281.2	v_2^-	5_2	1374.8	1316.7	1256.3	406.6	348.6	288.2	125.4	67.3	7.0
41	1249.4	281.2	v_2^-	5_2	1374.8	1316.7	1256.3	406.6	348.6	288.2	125.2	67.3	7.0
42	1260.5	292.3	v_2^-	5_1	1322.1	1335.6	1268.2	354.0	367.4	300.1	61.7	75.1	7.7
43	1260.5	292.3	v_2^-	5_1	1320.9	1335.6	1268.2	352.7	367.4	300.1	60.4	75.1	7.7
44	1264.1	296.0	v_2^-	5_0	1295.5	1341.9	1272.1	327.4	373.7	304.0	31.4	77.7	8.0

The numerical rovibrational energy levels computed in the CFA bear out these predictions. For $J = 1$ (see Table 13 and Table S16), the $\Delta(\hat{T}_{VR})$ errors for rovibrational energy levels belonging to the first five vibrational states are between 1 and 18 cm^{-1} for the zxzE. They drop to 2–5 cm^{-1} for the EE, and further decrease to 0.1–0.8 cm^{-1} for the FEE. Going higher in energy, negative $\Delta(\hat{T}_{VR})$ errors also appear for rovibrational levels belonging to degenerate vibrations. These negative errors are larger for the FEE; therefore, for certain levels, EE is the better performing of the two. The $\Delta(\hat{T}_{VR})$ errors are plotted in Fig. 11 for all three embeddings. The order of magnitude differences between the three embeddings are clearly visible on these figures, as well as the negative $\Delta(\hat{T}_{VR})$ errors. Note that the trends within a rovibrational band for the *zxz* and EE embeddings are different. For zxzE, the errors for the 1_1 states are always larger than those for the 1_0 states, while for EE, this relation is reversed.

The differences among the embeddings become even more pronounced for $J = 5$ (see Table 14 and Table S17). The errors increase up to 430 cm^{-1} for zxzE, up to 80 cm^{-1} for EE, but only up to 8 cm^{-1} for FEE. The $\Delta(\hat{T}_{VR})$ errors are plotted in Fig. 12 for all three embeddings. The order of magnitude differences between the embeddings are very clear. Furthermore, the $\Delta(\hat{T}_{VR})$ errors do not show significant vibrational dependence, although they are clearly affected by the different rotational states, as discussed.

In conclusion, the energy levels of the tetraatomic $^{14}NH_3$ molecule can be computed fairly accurately using FEE in the CFA. Therefore, the CFA with FEE might be a choice worth pursuing for larger and especially for heavier molecular systems, as well.

6. Summary and conclusions

This paper is devoted to the study of approximations to the exact field-free rovibrational Hamiltonian, $\hat{H}_{VR}$, with the aim to optimally decouple the rotational and vibrational degrees of freedom characterizing the gas-phase dynamics of molecules. The magnitude of Coriolis coupling, usually denoted as the $\hat{T}_{VR}$ kinetic-energy term of $\hat{H}_{VR}$, was investigated across a wide range of embeddings, coordinate systems, and several prototypical molecules, including the triatomic AB$_2$ (H$_2{}^{16}$O and D$_2{}^{16}$O), the triatomic A$_3$ (^{16}O$_3$ and H$_3^+$), the triatomic ABC (HD^{16}O), and the tetratomic AB$_3$ (^{14}NH$_3$) cases. During the search for the optimal separation of the rotational and vibrational degrees of freedom, a sequence of increasingly severe approximations to $\hat{H}_{VR}$ are introduced. They all involve the *Coriolis-free* approximation (CFA), where $\hat{T}_{VR}$ is neglected, and extend to the *diagonal* $\mathbf{G}_R$ approximation (DGRA), where the pure rotational kinetic-energy term, $\hat{T}_R$, is simplified, arriving finally at the *generalized centrifugal sudden* approximation (GCSA), where, due to further simplifications in $\hat{T}_R$, the rovibrational Hamiltonian becomes decoupled in the K rotational quantum number.

The role of vibrational coordinates and body-fixed axis embeddings on the separation of rotations and vibrations was assessed at every rung of this approximation hierarchy. We confirm that the Coriolis-coupling term, $\hat{T}_{VR}$, is indeed independent of the choice of the vibrational coordinates. Then we compare the performance of many different embeddings in the Coriolis-free approximation. Though it is impossible to choose a body-fixed frame that will cause Coriolis coupling to vanish over the whole shape space [34], we show that it is worth seeking the optimal embedding for a given molecule, as different embeddings are characterized by significantly different decouplings. We also show that embeddings exist for which Coriolis coupling vanishes at many configuration-space points—not just at the reference structure, as the Eckart embedding was designed to do.

During our search for the optimal embedding, we utilized different techniques to determine embedding effects. To start with, we performed analytical derivations yielding interesting insight, especially for AB$_2$ molecules. Then, we evaluated the magnitude of Coriolis coupling based on variationally computed rovibrational eigenenergies, employing the exact and the different approximate Hamiltonians. We utilized various embedding choices—some standard, and some less usual—in order to understand the most important characteristics of the approximations. An important question addressed is whether it is indeed the classical [19] Eckart embedding that provides the best separation of rotations and vibrations when a large number of rovibrational eigenstates is considered.

The analytical derivations focused on the $\mathbf{G}_R$ and $\mathbf{G}_{VR}$ tensor elements determining the form of the kinetic-energy operator, both responsible for the coupling of vibrations and rotations. We extensively studied the structure of these tensors for AB$_2$-type molecules, both at C_{2v}- and C_s-symmetry structures. As is well known, for the Eckart embedding Coriolis coupling is zero at the reference geometry—*i.e.*, at a single point, usually chosen as the equilibrium geometry of the molecule. Surprisingly, we discovered that the Radau bisector embedding goes much further than Eckart in decoupling rotations and vibrations, resulting in vanishing Coriolis coupling over not just a single point but an entire two-dimensional subspace. Moreover, we determined that Coriolis coupling is never zero in any of the Jacobi and Radau bond embeddings.

Since the $\mathbf{G}_{VR}$ tensor depends on the vibrational coordinates, its individual tensor elements can not measure appropriately the extent of Coriolis coupling. Instead of this measure [43], we advocate the use of the quantity $\|\mathbf{G}_R - \mathbf{g}_R^{-1}\|_F$ (FNGR) for this purpose, which is the Frobenius norm of the difference between the rotational and inverse moment-of-inertia tensors, providing a coordinate-independent measure for the magnitude of Coriolis coupling. For triatomic molecules, lying in the (x, y) plane, this norm becomes simply $|G_{zz}^R - 1/g_{zz}^R|$. During our tests based on variational nuclear-motion computations, we obtained the $\mathbf{G}$ tensor elements numerically at different distorted geometries and computed $\|\mathbf{G}_R - \mathbf{g}_R^{-1}\|_F$ values, which successfully verify our analytical findings.

Our extensive numerical studies designed to test embeddings involved a number of approximate rovibrational Hamiltonians. First, we computed rovibrational eigenenergies in the Coriolis-free approximation—that is, after neglecting the $\hat{T}_{VR}$ term form the exact $\hat{H}_{VR}$. To determine the performance of the different embeddings, we compared the eigenenergies of the Coriolis-free approximation with the rovibrational eigenenergies computed using the full Hamiltonian. For the special case of triatomic AB$_2$ molecules (namely H$_2{}^{16}$O), we went further, by neglecting the G_{xy}^R term from $\hat{T}_R$, yielding the *diagonal* $\mathbf{G}_R$ approximation. We proved that the *diagonal* $\mathbf{G}_R$ approximation leads to two distinct and almost-perfectly-good parity quantum numbers, one for rotations and one for vibrations. Furthermore, for what we call "linear" embeddings, the *diagonal* $\mathbf{G}_R$ approximation should *always* be used instead of the Coriolis-free approximation, since the extra errors introduced in the eigenenergies at this rung of the approximation hierarchy are minimal, while the savings in computational requirements are substantial.

We also introduced a method to generalize the centrifugal-sudden approximation, resulting in what we call the generalized centrifugal-sudden approximation—whereby upon averaging different diagonal $\mathbf{G}_R$ elements, the different K blocks in the

rovibrational Hamiltonian decouple, resulting in the considerable advantage that K becomes a good quantum number. By comparing different embeddings, we concluded that for all Jacobi and Radau bond embeddings, which have been used historically in the context of the centrifugal-sudden approximation, the diagonal $\mathbf{G}_R$ approximation is actually equivalent to the generalized centrifugal-sudden approximation.

Based on the numerical computations carried out, several additional important molecule-specific conclusions can be drawn. For water ($H_2{}^{16}O$), our prototypical AB_2 molecule, we determined that overall it is the Radau-bisector embedding that is best in minimizing Coriolis coupling. For the Coriolis-free approximation, this choice yields less than 0.5 cm^{-1} $\Delta(\hat{T}_{VR})$ errors for the first 50 $J = 1$ rovibrational states, although the Eckart embedding is only slightly worse (with less than 1.0 cm^{-1} $\Delta(\hat{T}_{VR})$ errors).

This is mostly due to the fact that the Radau-bisector embedding has a two-dimensional C_{2v} subspace for which Coriolis coupling vanishes. Furthermore, based on numerical $\|\mathbf{G}_R - \mathbf{g}_R^{-1}\|_F$ values, we realized that for AB_2 molecules, Coriolis coupling in the Eckart embedding is zero not only at the equilibrium geometry but actually over the entire one-dimensional, pure symmetric stretching distortion space (no distortion of the angle from its reference value is permitted). We have also observed that the Radau-bisector embedding and the flexible-Eckart embedding following the Radau angle are identical, which holds for all triatomic AB_2 molecules. Moreover, we concluded that the Jacobi and Radau bond embeddings always perform worse in the Coriolis-free approximation than the valence/Radau-bisector and the Eckart embeddings (the best one, the symmetric Jacobi r embedding, has $\Delta(\hat{T}_{VR})$ errors only up to 6.0 cm^{-1}), and that the asymmetric Jacobi-bisector embedding is very close to its Radau counterpart.

Regarding the deuterated water isotopologues, we noted that the $D_2{}^{16}O$ results show the exact same patterns as observed for $H_2{}^{16}O$, but with errors half as large. This is due to the mass difference introduced by the H/D substitution. For the ABC prototype $HD{}^{16}O$, we found that the use of the valence/Radau-bisector embeddings becomes less favorable compared to the Eckart embedding. Nevertheless, mass-weighting the bisector angle—an at-present unusual proposition—reverses the order. Using valence/Radau-mass-weighted-bisector embeddings yields similar performance to the valence/Radau-bisector embedding results noted for $H_2{}^{16}O$. The Radau mass-weighted-bisector embedding and the flexible-Eckart embedding following the Radau angle are identical for triatomic ABC molecules.

Studying the two A_3-type molecules resulted in observations rather different from those of the AB_2 and ABC prototypes. In the case of H_3^+, we observed that the system has an inherently large Coriolis coupling. It appears that it is the Coriolis coupling that is mostly responsible for the deviations of the rotational levels from the rigid-rotor model results. None of the embeddings perform nearly as well as they do for $H_2{}^{16}O$; neglecting the $\hat{T}_{VR}$ term results in $\Delta(\hat{T}_{VR})$ errors as large as 65–75 cm^{-1} for the first 50 $J = 1$ rovibrational eigenenergies. The Eckart and the Radau-bisector embeddings appear to be the most effective decoupling options, with the Eckart embedding performing consistently better for the singly-degenerate states, which can be computed fairly accurately within the Coriolis-free approximation. For ozone ($^{16}O_3$), a molecule with three different versions of its equilibrium structure, the situation is just the opposite to that of H_3^+. In this case, as expected, Coriolis coupling is small, the Radau bisector and Eckart embeddings perform equally well when describing only one potential well, with $\Delta(\hat{T}_{VR})$ errors being smaller than 0.01 cm^{-1} for the first 50 states for $J = 1$, which increases only up to 0.1 cm^{-1} for $J = 5$. Describing all three wells in the same

Coriolis-free approximation computation, however, is challenging and it is not straightforward to achieve the same accuracy for all minima.

We extended some of the methodologies we applied to triatomic molecules to ammonia ($^{14}NH_3$), a tetratomic molecule with one characteristic large-amplitude motion. We carried out nuclear-motion computations within the Coriolis-free approximation for the first time for a tetratomic molecule. We observed that the Eckart embedding results in significantly more accurate eigenenergies than a generic embedding, with $\Delta(\hat{T}_{VR})$ errors less than 8 cm^{-1} for the first 100 states of $J = 1$, which increases to 80 cm^{-1} for $J = 5$. Moreover, we determined that the flexible-Eckart embedding following the inversion motion is superior to the simple Eckart embedding, with $\Delta(\hat{T}_{VR})$ errors less than 0.1 cm^{-1} for the $J = 1$ eigenstates on the ground vibrational state, increasing to less than 1.5 cm^{-1} for $J = 5$. We realized that the flexible-Eckart embedding, in general, provides fairly accurate energy levels in the Coriolis-free approximation up to $J = 5$, where we stopped our investigation. The advantage of using the flexible-Eckart embedding is especially notable for higher J values. Our results seem to indicate that the flexible-Eckart embedding in the Coriolis-free approximation might be a choice worth pursuing during computation of approximate rovibrational eigenenergies for larger—and especially for heavier—molecular systems.

Lastly, we would like to point out that although the topic of minimizing Coriolis coupling and comparing embedding performances in variational rovibrational computations has long been of interest to many in the field of high-resolution molecular spectroscopy, without the ability of the GENIUSH protocol [12,15,16,63,64] to switch easily between exact and approximate Hamiltonians and different embeddings, the large amount of computations performed here could not have been carried out. The large amount of numerical results that can be generated with GENIUSH-like variational techniques puts special emphasis on analytical derivations, since without them it is next to impossible to understand the numerical results.

Declaration of Competing Interest

The authors declare that they have no known competing financial interests or personal relationships that could have appeared to influence the work reported in this paper.

Acknowledgments

Appendix A. Explicit tensor element formulas for g and G

Explicit formulas are presented here for the individual tensor elements of the **g** and **G** tensors of Eq. (20) and Eq. (22), respectively. The individual tensor elements in Eq. (20) are obtained from the Jacobian of the coordinate transformation as

$$g_{ij}^V = \sum_{n=1}^{N}\sum_{\alpha} m_n \left(\frac{\partial X_{n\alpha}}{\partial q_i}\right)\left(\frac{\partial X_{n\alpha}}{\partial q_j}\right)$$

$$g_{i\gamma}^{VR} = \sum_{n=1}^{N}\sum_{\alpha} m_n \left(\frac{\partial X_{n\alpha}}{\partial q_i}\right)\left(\frac{\partial X_{n\alpha}}{\partial \theta_\gamma}\right) \qquad (33)$$

$$g_{\beta\gamma}^R = \sum_{n=1}^{N}\sum_{\alpha} m_n \left(\frac{\partial X_{n\alpha}}{\partial \theta_\beta}\right)\left(\frac{\partial X_{n\alpha}}{\partial \theta_\gamma}\right)$$

Note that every tensor element of **g** depends only on the geometry—i.e., on the values of the vibrational coordinates, q_i, and not on those of the rotational coordinates, θ_α.

In Eq. (33) above, the number of particles N is arbitrary; for the AB_2 case, $N = 3$ and $n = \{1, 2, A\}$. Also, i, j, etc. label vibrational coordinates, whereas α, β, etc. label the Cartesian components, $\{x, y, z\}$. Strictly speaking, the $\vec{r}_n = (X_{nx}, X_{ny}, X_{nz}) = (X_n, Y_n, Z_n)$ are *space-fixed* coordinates, although by restricting consideration to the reference orientations, these become equivalent to body-fixed coordinate values, (x_n, y_n, z_n). The distinction only matters with respect to the differential *displacements* $dX_{n\alpha}$ associated with the partial derivatives; these are unconstrained, and thus give rise to differential displacements of the orientation and center of mass, away from the reference orientation and the origin, respectively.

The tensor elements of **G** can be obtained from the *inverse* Jacobian as follows:

$$G_{ij}^V = \sum_{n=1}^{N}\sum_{\alpha} \frac{1}{m_n}\left(\frac{\partial q_i}{\partial X_{n\alpha}}\right)\left(\frac{\partial q_j}{\partial X_{n\alpha}}\right)$$

$$G_{i\gamma}^{VR} = \sum_{n=1}^{N}\sum_{\alpha} \frac{1}{m_n}\left(\frac{\partial q_i}{\partial X_{n\alpha}}\right)\left(\frac{\partial \theta_\gamma}{\partial X_{n\alpha}}\right) \qquad (34)$$

$$G_{\beta\gamma}^R = \sum_{n=1}^{N}\sum_{\alpha} \frac{1}{m_n}\left(\frac{\partial \theta_\beta}{\partial X_{n\alpha}}\right)\left(\frac{\partial \theta_\gamma}{\partial X_{n\alpha}}\right)$$

Generally, we find it more convenient to obtain **G** directly from Eq. (34), rather than by inverting the tensor **g**.

As a technical point, it should be mentioned that the θ_α that appear above, and in Section 3.1, are *not* Euler angle coordinates—and in particular, cannot be used as global rotational coordinates at all, owing to the non-holonomic constraint imposed by the fact that rotations about the $\hat{x}, \hat{y}$, and $\hat{z}$ axes do not commute. However, this does not matter; in practice, we need to consider only *differential* rotations, applied to geometries in the reference orientation, for which the origin of the space-fixed frame corresponds to the center of mass. By the same token, in Section 4.1, where true rotational coordinates are needed and used—i.e., the usual (ϕ, θ, χ) Euler rotation angles—it must be understood that these are not strictly canonically conjugate to $(\hat{J}_x, \hat{J}_y, \hat{J}_z)$, the usual body-fixed components of angular momentum.

Appendix B. Exactness of CFA eigenvalues for $J = 1$

As discussed in Section 5.2, and is evident from the relevant entries of Table 4, when the CFA is being used for $J = 1$—and for every single ν and every embedding—the 1_{01} rovibrational energy is *exact*. The reasons underlying this behavior are explained in this Appendix.

For $J = 1$, $\tilde{H}^J$ has a 3×3 sub-block structure, as discussed. In a parity-adapted basis set (i.e., $\bar{K} = \{1^+, 0^+, 1^-\}$) these form a 2×2 $p = +1$ upper-left diagonal block, a 1×1 $p = -1$ lower-right diagonal block, and two rectangular off-diagonal blocks [see Eq. (35)]. Now, it can be shown that the matrix representations for $\hat{J}_\alpha^2$ (for all α) are block-diagonal, as are those for $\hat{J}_a$ and $\hat{J}_{bc} = (\hat{J}_b\hat{J}_c + \hat{J}_c\hat{J}_b)$.

On the other hand, the matrices for $\hat{J}_b, \hat{J}_c, \hat{J}_{ab}$, and $\hat{J}_{ac}$ have non-zero entries *only* in the off-diagonal blocks.

For the purposes of discussion, then, by choosing $\hat{a} = \hat{z}, \hat{b} = \hat{x}, \hat{c} = \hat{y}$, one obtains a matrix representation of $\hat{T}_R$ that is block-diagonal with respect to parity:

$$\tilde{T}_R^{J=1} = \begin{pmatrix} G_{yy}^R + G_{zz}^R & -iG_{xy}^R & 0 \\ iG_{xy}^R & G_{xx}^R + G_{zz}^R & 0 \\ 0 & 0 & G_{xx}^R + G_{yy}^R \end{pmatrix} \qquad (35)$$

To be sure, the vibrational KEO matrix $\tilde{T}_V^{J=1}$ is block-diagonal with respect to $\bar{K}$, implying that it, too, is block diagonal with respect to $\bar{K}$.

This leaves only the Coriolis contribution, $\tilde{T}_{VR}^{J=1}$. Now, we saw already in Section 3.2.2 that for all embeddings only the G_{iz}^{VR} components of the CC contribution are non-zero. This implies that the only non-vanishing contribution to $\tilde{T}_{VR}^{J=1}$ comes from $\hat{J}_z = \hat{J}_a$. As discussed above, however, $\hat{J}_a$ is also block diagonal. Specifically,

$$\tilde{J}_a^{J=1} = \begin{pmatrix} 0 & 1 & 0 \\ 1 & 0 & 0 \\ 0 & 0 & 0 \end{pmatrix} \qquad (36)$$

This implies that the total Hamiltonian matrix, $\tilde{H}^{J=1}$, adopts the parity-adapted block-diagonal form of Eq. (35), so that each parity block may be diagonalized separately. Moreover, note that the $\tilde{J}_a^{J=1}$ matrix makes no contribution to the 1×1 negative parity block. Consequently, *CC has no impact whatsoever on the $J = 1, p = -1$ eigenstates*; removing $\hat{T}_{VR}$ from the Hamiltonian does not alter the computed energy levels.

Appendix C. Extreme closeness of CFA and DGRA rovibrational energy levels for symmetric embeddings

As discussed in Section 4.3 and in Sec. VI of the supplementary material, the diagonal $\mathbf{G}_R$ approximation provides approximate energy levels that are *remarkably* close to the CFA levels, for symmetric embeddings of AB_2 molecules. Why does this approximation perform so well? How can it be that discarding a contribution from the Hamiltonian, that is on the order of $10\ \text{cm}^{-1}$, gives rise to new energy levels that are no more than $0.01\ \text{cm}^{-1}$ different from the old? This can be explained on permutation symmetry grounds as follows.

Consider a combined rotation-vibration basis set that is permutation-symmetry-adapted with respect to both vibration (ε_{vib}) and rotation (ε_{rot}). For simplicity, we will consider just the $J = 1$ case explicitly. In the fully symmetry-adapted basis representation, the Hamiltonian matrix $\tilde{H}^{J=1}$ becomes rigorously block-diagonal by both parity and permutation symmetry—with each block labeled by the corresponding permutation-inversion irreducible representation (PI irrep). In what follows, we consider the $p = 1, \varepsilon = 1$ PI block, but similar arguments would apply to all such blocks.

The $\tilde{H}^{J=1, p=1, \varepsilon=1}$ block further subdivides by rotation and/or vibration permutation symmetry. For definiteness, we take the upper-left diagonal sub-block to correspond to $\varepsilon_{vib} = \varepsilon_{rot} = 1$, and the lower-right sub-block to $\varepsilon_{vib} = \varepsilon_{rot} = -1$. In the diagonal $\mathbf{G}_R$ approximation, $\tilde{H}^{J=1, p=1, \varepsilon=1}$ is (sub)-block diagonal, so that the off-diagonal blocks are zero. However, since the G_{xy}^R contribution is known to change the character of ε_{vib} and ε_{rot}, this contribution to the CFA must lie within the off-diagonal blocks. Finally, we note that the vibrational contribution respects all forms of permutation symmetry.

Schematically, therefore, we have a Coriolis-free Hamiltonian matrix of the form

$$\tilde{H}^{J=1,p=1,\varepsilon=1} = \begin{pmatrix} \tilde{H}^{V+} + \tilde{G}^{R+}_{\alpha\alpha} & \tilde{G}^{R}_{xy} \\ \tilde{G}^{R}_{xy} & \tilde{H}^{V-} + \tilde{G}^{R-}_{\alpha\alpha} \end{pmatrix} \quad (37)$$

Removing the $\tilde{G}^{R}_{xy}$ off-block-diagonal sub-blocks results in the diagonal $\mathbf{G}_R$ approximation.

Next, consider that the vibrational Hamiltonian matrix elements are much larger than the rotational ones, in general—and in symmetric embeddings, G^{R}_{xy} is often quite small for the most important geometries—so that $|G^{R}_{xy}|/|H^{V\pm}| \approx \lambda \ll 1$. For $H_2{}^{16}O$, we can estimate $|H^{V\pm}| \approx 2500$ cm^{-1}, and $|G^{R}_{xy}| \approx 5$ cm^{-1}, so $\lambda \approx 0.002$. The quantity λ may be useful as a measure of adiabaticity—much like the electron-nucleon mass ratio in the Born–Oppenheimer approximation. Here, we use it in a different manner.

The next step is to transform the Coriolis-free matrix of Eq. (35), into (sub)-block-diagonal form, through the use of successive Jacobi rotation transformations, to zero the $\tilde{G}^{R}_{xy}$ elements in the off-diagonal blocks. Each such Jacobi rotation matrix is of the form

$$\tilde{O}_{i_+ i_-}(\varphi) = \begin{pmatrix} 1 & \cdots & 0 & \cdots & 0 & \cdots & 0 \\ \vdots & \ddots & \vdots & \ddots & \vdots & \ddots & \vdots \\ 0 & \cdots & \cos\varphi & \cdots & \sin\varphi & \cdots & 0 \\ \vdots & \ddots & \vdots & \ddots & \vdots & \ddots & \vdots \\ 0 & \cdots & -\sin\varphi & \cdots & \cos\varphi & \cdots & 0 \\ \vdots & \ddots & \vdots & \ddots & \vdots & \ddots & \vdots \\ 0 & \cdots & 0 & \cdots & 0 & \cdots & 1 \end{pmatrix}, \quad (38)$$

where deviations from the identity matrix occur only on the i_+'th and i_-'th rows and columns.

The angle φ is chosen so as to zero out the element, $G^{R,xy}_{i_+,i_-}$. It can be shown that

$$\tan(2\varphi) = \frac{2G^{R,xy}_{i_+,i_-}}{(H^{V-}_{i_-,i_-} - H^{V+}_{i_+,i_+}) + (G^{R-,xy}_{i_-,i_-} - G^{R+,xy}_{i_+,i_+})} \quad (39)$$

Since the two $\tilde{H}^{V\pm}$ matrix elements are generally different, $\tan(2\varphi)$ is of order λ, so to first order in λ, $\varphi \approx \lambda$, $\sin\varphi \approx \lambda$, and $\cos\varphi \approx 1$. Substituting into Eq. (38), to first order in λ, the remaining matrix elements transform as follows (or remain unchanged, if not listed below):

$$G^{R,xy}_{i_\pm,j_\mp} \rightarrow G^{R,xy}_{i_\pm,j_\mp} - \lambda H^{V\mp}_{i_\mp,j_\mp} + \mathcal{O}(\lambda^2)$$
$$(H^{V\mp}_{i_\mp,j_\mp} + G^{R\mp,\alpha\alpha}_{i_\mp,j_\mp}) \rightarrow (H^{V\mp}_{i_\mp,j_\mp} + G^{R\mp,\alpha\alpha}_{i_\mp,j_\mp}) + \lambda G^{R,xy}_{i_\pm,j_\mp} + \mathcal{O}(\lambda^2) \quad (40)$$
$$(H^{V\pm}_{i_\pm,i_\pm} + G^{R\pm,\alpha\alpha}_{i_\pm,i_\pm}) \rightarrow (H^{V\pm}_{i_\pm,i_\pm} + G^{R\pm,\alpha\alpha}_{i_\pm,i_\pm}) \mp \lambda G^{R,xy}_{i_+,i_-} + \mathcal{O}(\lambda^2)$$

Let us analyze the orders of the corrections above in λ. The off-(sub)-block-diagonal matrix elements, $G^{R,xy}_{i_\pm,j_\mp}$, start out as first-order in λ and remain first-order. However, the corrections to the diagonal-(sub)-block elements above are all *second*-order in λ, since $\tilde{G}^{R}_{xy}$ is itself first order. Consequently, to first order in λ, *the diagonal (sub)-blocks in Eq. (37) are unchanged under the Jacobi rotation.* In practice, a potentially large number of Jacobi rotations must be applied, in order to eventually zero all $\tilde{G}^{R}_{xy}$ matrix elements. None of these has any effect on the diagonal blocks at all, up to first order in λ. Consequently, the block-diagonal matrix that results is simply the diagonal $\mathbf{G}_R$ Hamiltonian matrix. Therefore, *energy*

eigenvalues for the Coriolis-free and diagonal $\mathbf{G}_R$ approximations are identical, apart from corrections of order λ^2. In the case of $H_2{}^{16}O$, this works out to $2500 \times 0.002^2 \approx 0.01$ cm^{-1}.

Although specific results are not presented in this paper, we have also performed calculations for which just the G^{R}_{xy} contribution is removed from the exact Hamiltonian—*i.e.*, CC is retained. Curiously, the energy eigenvalue errors in this case are on the order of 5 cm^{-1}—*i.e.*, $\mathcal{O}(\lambda)$, rather than $\mathcal{O}(\lambda^2)$. This, too, can be explained. The CC contribution also enters into the off-diagonal blocks—at order λ^0, rather than λ. Thus, the first correction that appears in the second two lines of Eq. (40) is in this case of order λ, rather than λ^2.

Appendix D. $\tilde{H}^{JK}$ blocks of the GCSA

An explicit expression for each of the $\tilde{H}^{JK}$ block of the GCSA is provided here, as represented in a Jacobi or Radau bond embedding. Each such $\tilde{H}^{JK}$ block is essentially equal to the $\tilde{H}_V$ vibrational Hamiltonian, plus a J- and K-dependent three-body "centrifugal potential" correction term [54], arising from the $G^{R}_{\alpha\alpha}$ part of the rotational KEO. For definiteness, we consider the symmetric Jacobi R embedding, although this can easily be generalized for any other such embedding via a simple substitution of masses and vector labels. For this choice, $G^{R}_{zz} = G^{R}_{xx}$, so $\hat{c} = \hat{y}$. Thus,

$$\hat{T}^{R} \approx \tfrac{1}{2}\left[G^{R}_{zz}\hat{J}^2 + (G^{R}_{yy} - G^{R}_{zz})\hat{J}^2_c\right]$$
$$V^{JK}_{\text{cent}}(r,R,\gamma) = \tfrac{\hbar^2 J(J+1)}{2}G^{R}_{zz} + \tfrac{\hbar^2 K^2}{2}(G^{R}_{yy} - G^{R}_{zz}) \quad (41)$$

From Eq. (32), we obtain expressions for G^{R}_{yy} and G^{R}_{zz} in terms of the vibrational coordinates, $(\Delta x, \Delta y, \gamma)$. Transforming to (r, R, γ) via

$$r = 2(x_0 + \Delta x)$$
$$R = (1 + 2m/M)(y_0 + \Delta y), \quad (42)$$

we obtain finally

$$V^{JK}_{\text{cent}}(r,R,\gamma) = \frac{\hbar^2 J(J+1)}{2}\frac{(2m+M)}{2mMR^2} + \frac{\hbar^2 K^2}{2}\left[\frac{2\csc^2\gamma}{mr^2} + \frac{(2m+M)}{2mMR^2}(\cot^2\gamma - 1)\right] \quad (43)$$

This matches exactly the symmetric rotor centrifugal potential form as derived in Eq. (7) of Ref. [54].

Appendix E. Supplementary material

Supplementary data associated with this article can be found, in the online version, at https://doi.org/10.1016/j.saa.2020.119164.

References

[1] R. Meyer, H.H. Günthard, J. Chem. Phys. 50 (1969) 353.
[2] H.-D. Meyer, U. Manthe, L.S. Cederbaum, Chem. Phys. Lett. 165 (1990) 73.
[3] M.H. Beck, A. Jäckle, G.A. Worth, H.-D. Meyer, Phys. Rep. 324 (2000) 1.
[4] D. Luckhaus, J. Chem. Phys. 113 (2000) 1329.
[5] D. Lauvergnat, A. Nauts, J. Chem. Phys. 116 (2002) 8560.
[6] D. Luckhaus, J. Chem. Phys. 118 (2003) 8797.
[7] W. Chen, B. Poirier, J. Comput. Phys. 219 (2006) 185.
[8] W. Chen, B. Poirier, J. Comput. Phys. 219 (2006) 198.
[9] D. Lauvergnat, G.D.E. Baloitcha, M. Desouter-Lecomte, Chem. Phys. 326 (2006) 500.
[10] S.N. Yurchenko, W. Thiel, P. Jensen, J. Mol. Spectrosc. 245 (2007) 126.
[11] J.M. Bowman, T. Carrington, H. Meyer, Mol. Phys. 48 (2008) 2145.
[12] E. Mátyus, G. Czakó, A.G. Császár, J. Chem. Phys. 130 (2009) 134112.
[13] W. Chen, B. Poirier, J. Parallel Distrib. Comput. 70 (2010) 779.
[14] W. Chen, B. Poirier, J. Theoret. Comput. Chem. 9 (2010) 825.
[15] C. Fábri, E. Mátyus, A.G. Császár, J. Chem. Phys. 134 (2011) 074105.
[16] A.G. Császár, C. Fábri, T. Szidarovszky, E. Mátyus, T. Furtenbacher, G. Czakó, Phys. Chem. Chem. Phys. 14 (2012) 1085.

[17] C. Petty, B. Poirier, Appl. Math. 5 (2014) 2756.
[18] I.E. Gordon, L.S. Rothman, C. Hill, R.V. Kochanov, Y. Tan, P.F. Bernath, M. Birk, V. Boudon, A. Campargue, K.V. Chance, B.J. Drouin, J.-M. Flaud, R.R. Gamache, J.T. Hodges, D. Jacquemart, V.I. Perevalov, A. Perrin, K.P. Shine, M.-A.H. Smith, J. Tennyson, G.C. Toon, H. Tran, V.G. Tyuterev, A. Barbe, A.G. Császár, V.M. Devi, T. Furtenbacher, J.J. Harrison, J.-M. Hartmann, A. Jolly, T.J. Johnson, T. Karman, I. Kleiner, A.A. Kyuberis, J. Loos, O.M. Lyulin, S.T. Massie, S.N. Mikhailenko, N. Moazzen-Ahmadi, H.S.P. Müller, O.V. Naumenko, A.V. Nikitin, O.L. Polyansky, M. Rey, M. Rotger, S.W. Sharpe, K. Sung, E. Starikova, S.A. Tashkun, J. Vander Auwera, G. Wagner, J. Wilzewski, P. Wcisło, S. Yu, E.J. Zak, J. Quant. Spectrosc. Radiat. Transfer 203 (2017) 3.
[19] C. Eckart, Phys. Rev. 46 (1934) 383.
[20] H.M. Pickett, J. Chem. Phys. 56 (1972) 1715.
[21] X.-G. Wang, T. Carrington Jr., J. Chem. Phys. 129 (2008) 234102.
[22] C. Fábri, J. Sarka, A.G. Császár, J. Chem. Phys. 140 (2014) 051101.
[23] O. Asvany, K.M.T. Yamada, S. Brünken, A. Potapov, S. Schlemmer, D. Marx, Science 347 (2015) 1346.
[24] J. Sarka, C. Fábri, T. Szidarovszky, A.G. Császár, Z. Lin, A.B. McCoy, Mol. Phys. 113 (2015) 1873.
[25] J. Sarka, A.G. Császár, J. Chem. Phys. 144 (2016) 154309.
[26] X.-G. Wang, T. Carrington, J. Chem. Phys. 144 (2016) 204304.
[27] C. Fábri, M. Quack, A.G. Császár, J. Chem. Phys. 147 (2017) 134101.
[28] C. Fábri, A.G. Császár, Phys. Chem. Chem. Phys. 20 (2018) 16913.
[29] A.G. Császár, C. Fábri, J. Sarka, WIREs Comput. Mol. Sci. 10 (2020) e1432.
[30] P.R. Bunker, P. Jensen, Molecular Symmetry and Spectroscopy, second ed., NRC Research Press, Ottawa, 1998.
[31] J.O. Hirschfelder, E. Wigner, Proc. Natl. Acad. Sci. 21 (1935) 113.
[32] C.F. Curtiss, J.O. Hirschfelder, F.T. Adler, J. Chem. Phys. 18 (1950) 1638.
[33] J. Jellinek, D.H. Li, Phys. Rev. Lett. 62 (1989) 241.
[34] R.G. Littlejohn, M. Reinsch, Rev. Mod. Phys. 69 (1997) 213.
[35] D.R. Herschbach, V.W. Laurie, J. Chem. Phys. 37 (1962) 1668.
[36] V.W. Laurie, D.R. Herschbach, J. Chem. Phys. 37 (1962) 1687.
[37] B.T. Sutcliffe, J. Tennyson, Mol. Phys. 58 (1986) 1053.
[38] B.T. Sutcliffe, J. Tennyson, Int. J. Quantum Chem. 39 (1991) 183.
[39] K.L. Mardis, E.L. Sibert, J. Chem. Phys 106 (1997) 6618.
[40] C. Eckart, Phys. Rev. 47 (1935) 552.
[41] J.D. Louck, H.W. Galbraith, Rev. Mod. Phys. 48 (1976) 69.
[42] H. Wei, T. Carrington, J. Chem. Phys. 107 (1997) 2813.
[43] H. Wei, T. Carrington, J. Chem. Phys. 107 (1997) 9493.
[44] H. Wei, T. Carrington, Chem. Phys. Lett. 287 (1998) 289.
[45] J. Sarka, B. Poirier, V. Szalay, A.G. Császár, Sci. Rep. 10 (2020) 4872.
[46] P. McGuire, D. Kouri, J. Chem. Phys. 60 (1974) 2488.
[47] R.T. Pack, J. Chem. Phys. 60 (1974) 633.
[48] J.M. Bowman, J. Phys. Chem. 95 (1991) 4960.
[49] J.M. Bowman, Chem. Phys. Lett. 217 (1994) 36.
[50] J. Qi, J.M. Bowman, J. Chem. Phys. 105 (1996) 9884.
[51] D. Skinner, T. Germann, W. Miller, J. Phys. Chem. A 102 (1998) 3828.
[52] B. Poirier, J. Chem. Phys. 108 (1998) 5216.
[53] H. Zhang, S. Smith, J. Phys. Chem. 3246 (2006).
[54] C. Petty, B. Poirier, Chem. Phys. Lett. 605–606 (2014) 16.
[55] A. Sayvetz, J. Chem. Phys. 7 (1939) 383.
[56] S.V. Shirin, O.L. Polyansky, N.F. Zobov, P. Barletta, J. Tennyson, J. Chem. Phys. 118 (2003) 2124.
[57] J. Klos, M.H. Alexander, P. Kumar, B. Poirier, B. Jiang, H. Guo, J. Chem. Phys. 144 (2016) 174301.
[58] P. Kumar, B. Jiang, H. Guo, J. Klos, M.H. Alexander, B. Poirier, J. Phys. Chem. A 121 (2017) 1012.
[59] R.G. Littlejohn, M. Reinsch, Phys. Rev. A 52 (1995) 2035.
[60] Of course, operator ordering is a bit less trivial for $\mathbf{G}_V$, but can be handled in various standard ways, including the Podolsky "trick", which we need not concern ourselves with further here.
[61] K. Sadri, D. Lauvergnat, F. Gatti, H.-D. Meyer, J. Chem. Phys. 141 (2014) 114101.
[62] C. Petty, W. Chen, B. Poirier, J. Phys. Chem. A 117 (2013) 7280.
[63] C. Fábri, E. Mátyus, A.G. Császár, Spectrochim. Acta A 119 (2014) 84.
[64] E. Mátyus, C. Fábri, T. Szidarovszky, G. Czakó, W.D. Allen, A.G. Császár, J. Chem. Phys. 133 (2010) 034113.
[65] M. Pavanello, L. Adamowicz, A. Alijah, N.F. Zobov, I.I. Mizus, O.L. Polyansky, J. Tennyson, T. Szidarovszky, A.G. Császár, J. Chem. Phys. 136 (2012) 184303.
[66] R. Dawes, P. Lolur, A. Li, B. Jiang, H. Guo, J. Chem. Phys. 139 (2013) 201103.
[67] S.N. Yurchenko, R.J. Barber, J. Tennyson, W. Thiel, P. Jensen, J. Mol. Spectrosc. 268 (2011) 123.
[68] J. Tennyson, P.F. Bernath, L.R. Brown, A. Campargue, M.R. Carleer, A.G. Császár, R.R. Gamache, J.T. Hodges, A. Jenouvrier, O.V. Naumenko, O.L. Polyansky, L.S. Rothman, R.A. Toth, A.C. Vandaele, N.F. Zobov, L. Daumont, A.Z. Fazliev, T. Furtenbacher, I.F. Gordon, S.N. Mikhailenko, S.V. Shirin, J. Quant. Spectrosc. Radiat. Transf. 110 (2009) 573.
[69] J. Tennyson, O.L. Polyansky, N.F. Zobov, A. Alijah, A.G. Császár, J. Phys. B 50 (2017) 232001.
[70] T. Furtenbacher, T. Szidarovszky, E. Mátyus, C. Fábri, A.G. Császár, J. Chem. Theory Comput. 9 (2013) 5471.
[71] T. Furtenbacher, P.A. Coles, J. Tennyson, S.N. Yurchenko, S. Yu, B. Drouin, R. Tóbiás, A.G. Császár, J. Chem. Theory Comput. 251 (2020) 107027.